Proof of concept of a thermal imager with milliKelvin thermal resolution

Bart Festen

April 2, 2012

Exam committee members

Prof. Ir. R.H. Munnig Schmidt
Ir. R. Saathof (daily supervisor)
Ir. J.W. Spronck
Dr. Ir. J.F.L. Goosen

Acknowledgements

This research could not have been performed without the assistance of a number of people. First I would like to thank Rudolf Saathof for his daily support to the project, his continuos motivation to help students to gain new insights on their own and for the friendly atmoshpere. I would like to thank Jo Spronck for providing new ideas for the project and having a critical note on the work that had been performed.
Furthermore I would like to thank the exam committee members Robert Munnig Schmidt and Hans Goosen.
For all the support in making experimental setups I want to thank Harry, Patrick and Rob.
The Mechatronic System Design group of Master and PhD-students have made my stay during my Master's work a very fun time. These people were always there for a good laugh or a serious discussion. In would especially like to thank Jan for the jokes and the motivational words at the end of my project.
Last but not least I am thankful to my family and friends for all their support.

Abstract

In the semiconductor industry the continuous decrease of feature size on integrated circuits (ICs) drives the increasingly tight specifications on optical components of photolithography machines. Moreover, light source wavelength of such systems is brought to the extreme ultaviolet range (EUV) to improve the imaging resolution.

EUV light is absorbed by air and conventional optical components. The new generation lithography machines therefore operate in vacuum and with reflective optical components (mirrors) to decrease loss of light. The limited amount of light that is still lost by absorption of the mirrors causes thermal deformation of the mirrors and as a consequence optical aberrations. To be able to correct for the thermal deformation a thermal image of the mirror surface is needed. Due to vibration isolation of the mirrors a contact measurement is not possible and therefore a thermal imager (thermal camera) should provide the thermal image. Conventional thermal cameras are not suitable because these don't provide sufficient thermal resolution to detect the thermal deformations of interest. A novel concept for a thermal imager is therefore introduced. The novel concept consits of an array of pixels which measures thermal radiation from the back surface of a mirror (the target) falling on the pixels, from which a thermal image of the target's surface can be constructed. A new aspect of this concept is the fact that image resolution is preserved by placing the pixel array very close to the target object ($\sim$1 [mm] distance) instead of placing a lens in front of the pixel array. Furthermore the area of the individual pixels is increased compared to conventional thermal cameras in order to improve the attainable thermal resolution to at least 1 [mK] at a spatial resolution of 10 [mm] and a bandwidth of 1 [Hz]. The concept is modeled to show its theoretical performance and in an experimental setup the effect of increasing pixel area on the pixel's thermal behaviour and its ability to measure target temperature is validated.

The modeled design concept shows a thermal resolution of 0.09 [mK] at a pixel area of 1x1 [mm] and a thermal response time of 1 [s]. The experimental results show that increasing the pixel area at constant pixel thickness decreases the thermal response time of the pixel as was expected. This indicates that the radiation heat exchange of the pixel increases which is paramount to achieving the required thermal resolution. Additional experiments to obtain a quantitative measure of the ratio between the heat transfer coefficients of conduction and radiation to the pixel were not decisive. Finally the measurement of target temperature with a single pixel showed an rms error of 2.9 to 6.0 [mK] depending on the pixel area.

This research shows that an optimal design of the proposed concept leads to a thermal imager which meets the requirements set. Experimental validation further supports the model of the concept in terms of response time and has indicated that increasing pixel area will indeed improve the thermal resolution of the imager. Further research is required to investigate the realisation of spatial resolution and manufacturability of the concept.

Contents

List of Figures

List of Tables

CHAPTER 1

Introduction

1.1 General introduction

Integrated circuits (ICs) continously become faster and contain more functionality on the same size of substrate. These developments push hard on the performance of machines involved in the manufacturing of ICs. In the cyclic process of manufacturing ICs shown in figure 1.1, photolithography machines are responsible for the exposure part. During the exposure a patterned light bundle is incident on a photosensitive layer on the IC substrate. To be able to put smaller features on an IC, the resolution of the imaging inside the lithography machines must be improved. A current development to improve the imaging resolution is the use of a light source with shorter wavelength, extreme ultra violet light (EUV). Because EUV light is absorbed by air, these machines operate in vacuum. There is however still some loss of light because the mirrors which are used to focus the EUV onto the IC substrate absorb some of the light.

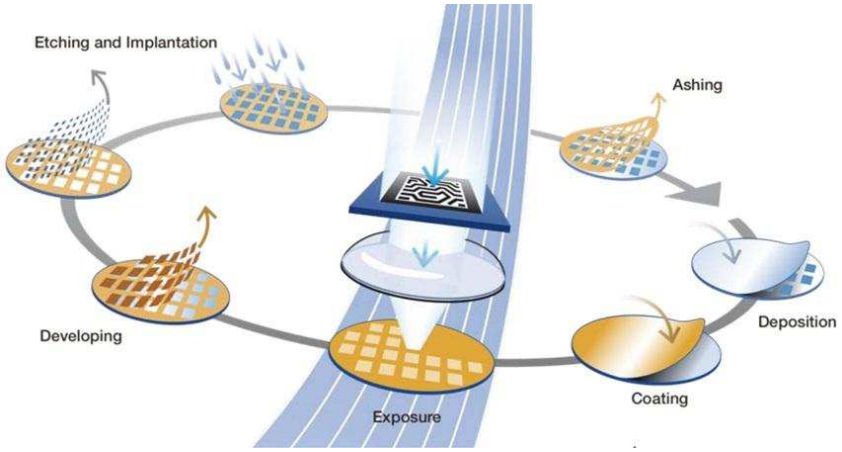

Figure 1.1: Overview of the manufacturing cycle of ICs. For the production of an IC, this cycle is passed through multiple times. The exposure part of the cycle takes place in lithography machines. [Source: ASML]

The light absorption of the mirror causes a heat input onto the mirror which results in thermal deformation of the mirror and consequently optical aberrations, which is shown schematically in figure 1.2. The optical aberrations distort the pattern exposure at the IC substrate and thereby limit the imaging resolution of the machine. The mirrors cannot be cooled easily because they are contactlessly supported and no gas or fluid can flow past them. A new way of controlling the mirror temperature is therefore required and one of the steps in this control is measuring the mirror temperature distribution with a sensor. Because the sensor makes an image of the mirror's thermal distribution it is referred to as a thermal imager.

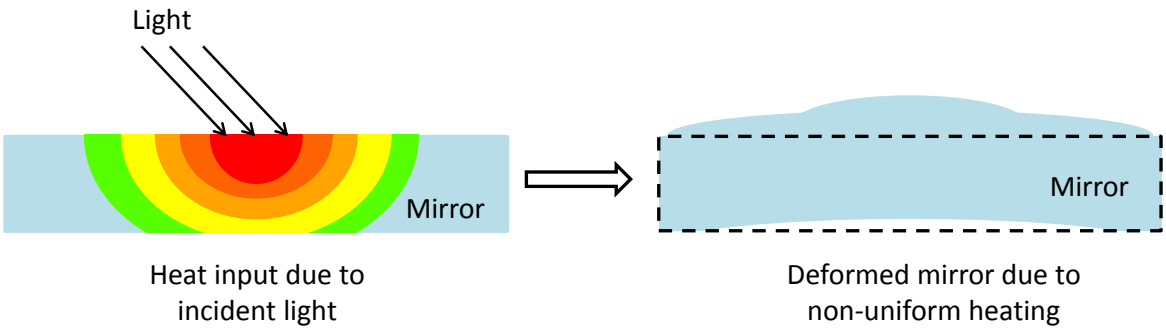

Figure 1.2: Light is incident on a small area of the top surface of a mirror and thereby heat the mirror locally (left). Due to the local heat input, the mirror temperature is non-uniform which causes the mirror to deform (right).

Important conditions for the thermal imager are that it should operate contactlessly and in vacuum. The proof of concept of such a thermal imager is the subject of this report.

1.2 Problem definition

The objective of this research is to provide a proof of concept of a thermal imager which can measure the temperature distribution of a mirror surface, contactless and with milliKelvin thermal resolution. For generality the object to be measured will be called 'target' from now on. The proposed specification for the temperature sensor is given in table 1.1.

Table 1.1: Proposed specifications for the thermal imager

Specification	Unit	Sign	Value	Remarks
Thermal resolution	[mK]		1	
Temperature range	[K]	±	2.5	Around ~ 300 [K]
Image resolution	[mm]		10	
Target area	[mm]		50 x 50	
Response time	[s]		1	

Besides the target specification some environmental conditions must be taken into account in the design of the thermal imager, which are listed here.

Contactless
There must be no mechanical contact between the target and the imager.

Back side of mirror
At the front side of the mirror, the mirror reflects light which is used for imaging in lithography machines. Consequently there is no room for a sensor at the front side of the mirror. The thermal imager will therefore have to be placed at the back side of the mirror.

Vacuum
The imager will be placed in near vacuum.

Heat
The imager should impose as little as possible heat input onto the target.

Space
The design must be compact because very limited space is available for the imager.

Cost
The imager is preferably of low cost compared to conventional thermal imagers.

The requirement on the thermal resolution of the imager stems from the magnitude of thermal deformations of the mirror that need to be detected. The origin of the thermal resolution requirement is discussed in detail in appendix A.1.

The working principle of the thermal imager concept and indicators to check its performance are discussed in 2. From the performance indicators a design path is constructed which guides the design of an optimal performing thermal imager. The design path and the design concept which resulted are shown in chapter 3. In order to validate the working principle and advantages of the proposed design, an experimental validation is carried out. The experimental validation is the subject of chapter 4. Finally the conclusions that are drawn from this research and recommendations for further research are given in chapter 5.

CHAPTER 2

Thermal imager concept

The need for a contactless sensor measuring temperature distribution of a target surface has been introduced in section 1.1. Temperature measurement always involves some heat transfer from a target to a sensor, after which the sensor converts the absorbed heat into an output signal. The output signal of the sensor is then a measure of target temperature. Heat transfer can occur in three ways; conduction, convection and radiation. In the section 2.1 it will become clear that heat between target and sensor can be transferred by radiation only due to the vacuum in which the system operates.
Radiation heat transfer between a target and a sensor object is discussed further in section 2.2. After the heat transfer consideration, conventional thermal imagers and the proposed novel concept are introduced in section 2.3.2. Section 2.4 shows the structure of the pixel of a thermal imager and its thermal behaviour, after which the temperature measurement element of the pixel, the detector, is discussed in section 2.5. Finally section 2.6 treats indicators of the performance of the pixel which have been derived to make an optimal pixel design.

2.1 Heat transfer

Conduction
The physical mechansisms of conduction are complex, encompassing such varied phenomena as molecular collisions in gases, lattice vibrations in crystals, and flow of free electrons in metals. The similarity between these cases is the contact between the particles transporting the heat. To transport heat from a target to a sensor by conduction the objects must be in physical

contact. Heat transfer by conduction is described by Fourier's law as,

$$\mathbf{q} = -k\nabla T$$

where $\mathbf{q}$ is the conduction heat flux vector, k is the conducting material's thermal conductivity and ∇T is the temperature gradient in x, y and z direction. Conduction in one direction can be conveniontly written as a product of a conduction heat transfer coefficient times the temperature difference of a material,

$$\begin{aligned} P_{\text{cond}} &= \frac{kA}{L}\Delta T \\ &= g_{\text{cond}}\Delta T \end{aligned} \tag{2.1}$$

where P_{cond} is the heat flow in [W], A is the cross-sectional area across which heat is transported, L is the distance across which the temperature gradient ΔT is defined. The conduction heat transfer coefficient is thus defined as, $g_{\text{cond}} = \frac{kA}{L}$ in [W/K]. Since the target of interest is suspended contactlessly and should remain contactless from its environment, heat transfer by conduction is dropped as a possible type of heat transfer between target and sensor. Conduction will however be important in analysing the thermal behaviour between contacting components in the sensor.

Convection

Convection or convective heat transfer is heat transfer from a surface to a moving fluid (gas or liquid). This type of heat transfer depends on the fluid flow, geometry of the surface and temperature of fluid and surface. Convection is generally approximated as the product of a surface averaged heat transfer coefficient $\overline{h}$, surface area A and temperature difference ΔT between surface and fluid. The convective heat transfer coefficient g_{conv} is then the product of $\overline{h}$ and A, such that convection heat transfer P_{conv} is given by,

$$P_{\text{conv}} = g_{\text{conv}}\Delta T \tag{2.2}$$

Due to the vacuum in which the system of target and sensor operate convection will be absent.

Radiation

Objects with a temperature above 0 [K], continuously emit electromagnetic radiation. A particle, or quantum, of electromagnetic energy is a photon, and heat transfer by radiation can be viewed either in terms of electromagnetic waves or in terms of photons, which are exchanged between objects. The electromagnetic radiation can also travel through a vacuum which makes it the only possible way for contactless heat transfer for the case at hand. Heat transfer by radiation depends on difference between temperatures to the power four. In section 2.2 it will be shown that by linearization around a temperature T_{lin} radiation heat flow P_{rad} can be written as,

$$P_{\text{rad}} = g_{\text{rad}}\Delta T \tag{2.3}$$

where g_{rad} is the radiation heat transfer coefficient in [W/K] and ΔT is the temperature difference between the objects involved in radiation heat exchange.

From the previous discussion it can be concluded that contactless heat transfer from target to sensor will be by radiation only. Heat transfer by radiation will be discussed further in section 2.2.

2.2 Radiation heat transfer

The heat transfer from a target object to a sensor, needed for measurement of target temperature, is by radiation only as described in section 2.1. Figure 2.1 shows heat radiation from target to a sensor P_{t-s}. The governing mechanisms of this radiation heat transfer is the subject of this section.

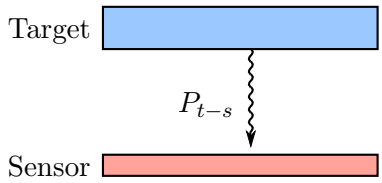

Figure 2.1: Schematic drawing showing heat radiation from target to sensor.

2.2.1 Blackbodies

The basics of radiation heat transfer start with the concept of a blackbody. A blackbody is defined as an object that absorbs all radiation falling on it, reflecting none [1]. As a consequence, all of the radiation leaving a blackbody is emitted by its surface and is given by the Stefan-Boltzmann law as,

$$E_{\text{bb}} = \sigma T^4 \tag{2.4}$$

where E_{bb} is the blackbody emissive power in [W/m^2], T is the blackbody's temperature in [K] and σ is the Stefan-Boltzmann constant[1] [Wm^{-2}K^{-4}]. Now the heat exchange between two blackbodies shown in figure 2.2 is considered. The blackbodies are isothermal plates of equal area A and temperature T_1 and T_2 respectively. The area of the plates is assumed to be very large compared to the distance between them, such that all radiation emitted by plate 1 is incident on plate 2 and vice versa. The radiation emitted by plate 1 and plate 2 is $A\sigma T_1^4$, $A\sigma T_2^4$ respectively. The radiation emitted by one plate is all incident on and absorbed by the other plate, such that the net radiation heat exchange between plate 1 and 2 is,

$$P_{1-2} = A\sigma(T_1^4 - T_2^4) \tag{2.5}$$

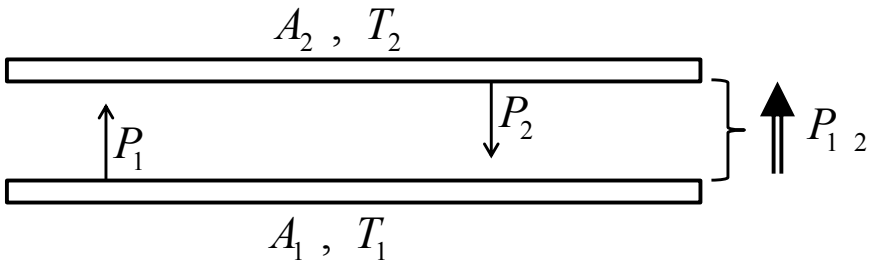

Figure 2.2: Two large black plates exchanging heat by radiation, showing the net radiative heat exchange from surface 1 to surface 2, P_{1-2}.

In practice most objects are not blackbodies. These objects are called graybodies and emit only a fraction of the radiation energy a blackbody emits at the same temperature. Graybodies will be discussed in the next section.

2.2.2 Graybodies

The target and sensor object shown in figure 2.1 are both graybodies. The radiation power emitted per area by such a graybody is given by,

$$E = \varepsilon \sigma T^4 \tag{2.6}$$

where ε is the emissivity of the graybody, which is a number between 0 and 1. Comparing with equation 2.4 the emissivity denotes the fraction of the blackbody emissive power the graybody emits. Also only a fraction of the radiation incident on a graybody is absorbed, the other part is reflected. For a non-transparent graybody the fractions of absorption and reflection are given by,

$$1 = \eta + \rho = \varepsilon + \rho$$

where η is the absorptivity and ρ the reflectivity of the graybody. This equation assumes that the variation of these coefficient with radiation wavelength is negligable. To obtain the net heat exchange between two graybodies, consider again the system of two large plates facing each other, shown in figure 2.2. In this case the plates are graybodies and therefore emit a radiation power of $A\sigma\varepsilon T^4$. Still assuming that all radiaton emitted by plate 1 is incident on plate 2 and vice versa, the net radiation heat exchange becomes,

$$P_{1-2} = \frac{A\sigma(T_1^4 - T_2^4)}{{}^1\!/_{\varepsilon_1} + {}^1\!/_{\varepsilon_2} - 1} \tag{2.7}$$

[1] $\sigma = 5.6697 \cdot 10^{-8}$ [$\mathrm{Wm^{-2}K^{-4}}$]

2.2.3 View factor

In the previous sections all radiation emitted from one object was assumed to be incident on the other. From figure 2.3a it is clear that this is not the case for radiation from a target to a sensor. In that case a measure is needed of radiation emitted by the source object that is actually incident on the receiving object. A view factor F_{1-2} is defined as the fraction of the radiation P_1 leaving surface 1 that is intercepted by surface 2, P_{1-2}.

$$F_{1-2} = \frac{P_{1-2}}{P_1} \tag{2.8}$$

The view factor depends on the area and orientation of the surfaces and on the distance between them. As such the view factor can be calculated when the geometry and orientation of the objects are known. The calculation of view factors is discussed further in appendix B.
Returning to the problem of heat exchange between two graybodies of section 2.2.2, the view factor can be added to equation 2.7 to account for the effect of the geometry of the objects. The radiation emitted by surface 1 that reaches surface 2 is given by $\sigma\varepsilon_1 T_1^4 A_1 F_{1-2}$ and radiation emitted by surface 2 that reaches surface 1 is $\sigma\varepsilon_1 T_1^4 A_1 F_{1-2}$. The net radiation heat exchange is now found to be,

$$P_{1-2} = \frac{\sigma(T_1^4 - T_2^4)}{\frac{1-\varepsilon_1}{\varepsilon_1 A_1} + \frac{1}{A_1 F_{1-2}} + \frac{1-\varepsilon_2}{\varepsilon_2 A_2}} \tag{2.9}$$

In this equation the reciprocal rule of view factors has been used which is given by $A_1 F_{1-2} = A_2 F_{2-1}$. For a square target and sensor of equal width w and with a distance d between them, the view factor is shown in figure 2.3b. Since the area of the target and the sensor are equal the reciprocal rule says that the view factor from target to sensor is equal to the view factor from sensor to target. The plot shows that decreasing the distance between the objects increases the view factor, which means that more radiation from one object reaches the other.

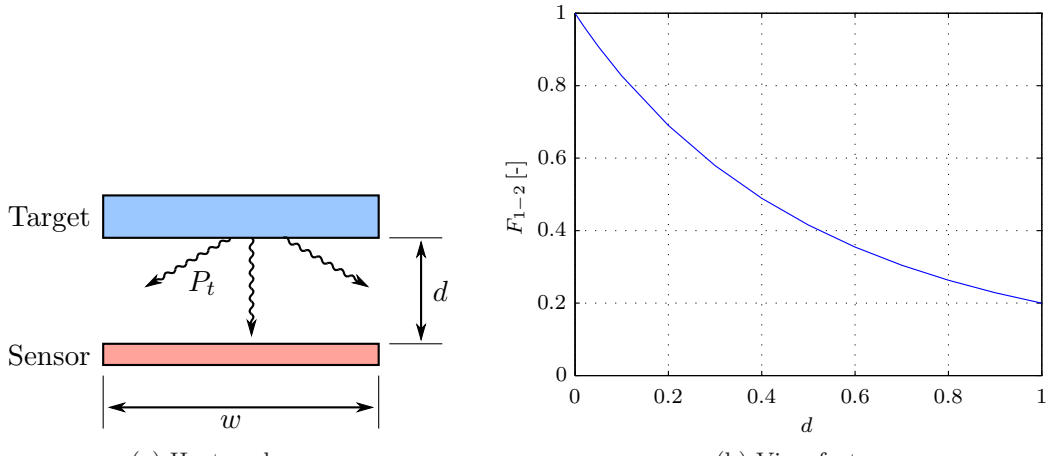

(a) Heat exchange

(b) View factor

Figure 2.3: Only a fraction of the radiation from the target reaches the sensor. This fraction is given by the view factor which decreases with increasing target-sensor distance.

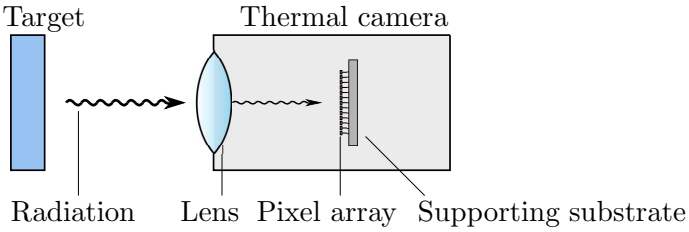

Figure 2.4: Schematic drawing of a conventional thermal camera receiving heat radiation from a target. Radiation is focussed by a lens onto the pixel array which is supported by a substrate.

2.2.4 Linearization of radiation

For small temperature differences between the objects involved in radiation equation 2.9 can be linearized. The heat exchange is linearized around a temperature T_{lin} such that it becomes linearly dependent on the temperature difference between the objects. The linearized heat exchange is given by,

$$\begin{aligned} P_{1-2} &= \frac{4\sigma T_{\text{lin}}^3}{\frac{1-\varepsilon_1}{\varepsilon_1 A_1} + \frac{1}{A_1 F_{1-2}} + \frac{1-\varepsilon_2}{\varepsilon_2 A_2}}(T_1 - T_2) \\ &= g_{\text{rad}}(T_1 - T_2) \end{aligned} \tag{2.10}$$

where g_{rad} is the radiation heat transfer coefficient. Throughout this report often a simpler form of g_{rad} is used, for example when the heat radiation leaving an object in all directions is considered. In that case the heat transfer coefficient is given by,

$$g_{\text{rad}} = 4\sigma\varepsilon T^3 A \tag{2.11}$$

2.3 System concept

2.3.1 Conventional thermal imagers

Section 2.1 showed that contactless temperature distribution measurement can only take place through measuring radiation heat from a target object. Such measurement devices exist and are called thermal cameras. In general a thermal camera consists of an array of radiation sensitive pixels supported on a substrate and a lens which focusses radiation coming from a target object onto the pixel array, as shown schematically in figure 2.4. The space between lens and pixel array is vacuum sealed to make sure no convective heat transfer can take place. In general the spatial resolution and measuring frequency are high relative to the spatial resolution and response time required for the current application. Pixel width of these cameras is in the order of 50 micrometers. Each pixel contains an element across its area which is responsible for the conversion of radiation into an electrical output signal. This element is called the detector and is the component which determines the type of thermal camera. There are generally two types of detectors; quantum detectors and thermal detectors.

Quantum detectors rely on the interaction of individual photons with the crystalline lattice of semiconductor materials [2]. They require cryogenic cooling of the support substrate to produce high sensitivity, which is very energy consuming and causes a large, unwanted heat sink in the system. Thermal sensitivity down to 10 [mK] is reported for quantum detectors [3]. For the application at hand the thermal influence of the temperature sensor must be minimal. The cryogenic cooling of the quantum detectors will cause a significant heat sink, which makes them unsuitable for this application. Quantum detectors will therefore not be discussed further.

Thermal detectors measure the bulk temperature increase of a pixel due to the overall heat exchange with a target and its environment. Types of thermal detectors are the resistive bolometer (thermistors, RTDs), ferroelectric bolometer (also called bias-enhanced pyroelectric detectors), pyroelectric detector, thermoelectric detector (thermocouples, thermopiles) and transistor detector. Also there are detection mechanisms based on mechanical movement due to gas expansion (Golay cell) or due to bimaterial thermal expansion. Resistive bolometers have proven to provide the best performance for thermal cameras and is therefore the only detector considered here [4]. Thermal resolution reported of thermal cameras with resistive bolometers range from 30 to 50 [mK] [5], [3]. The theoretical best performance of conventional thermal detectors, in the absence of electrical noise, is about 1 to 2 [mK].
Summarizing, both the conventional thermal and quantum detectors are not suitable due to their insufficient thermal resolution, which is at best 10 [mK] for quantum detectors. Moreover, quantum detectors require cryogenic cooling which causes a large unwanted thermal disturbance in the system. A new concept for a thermal imager is therefore needed for the application at hand.

2.3.2 General system concept

In this section the general principle of the concept is explained. A temperature from a target object is measured by detection of the radiation from the target falling on a sensor. This is shown schematically in the left of figure 2.5. The radiation from the target falling on the sensor $P_{\text{t-s}}$ causes the sensor to heat up and the resulting temperature increase is measured. From the temperature change of the sensor the target temperature should than be resolved. The sensor will however not only receive heat from the target above it, but also from its sides and bottom as shown in the middle of figure 2.5. A reference object is therefore placed underneath the sensor and its temperature is measured, such that the heat input from the bottom is known. Furthermore by placing the target, sensor and reference very close to each other the possible heat input from the sides becomes very small, which is shown in the right of figure 2.5.
Consider this system in the ideal case that no radiation heat enters the system through the sides and the target temperature is uniform and higher than the uniform temperature of the reference. Radiation between two objects was shown to be governed by equation 2.10. The

radiation heat transfer coefficient between target and sensor is now denoted as g_t and between reference and sensor by g_r. When the sensor is in steady state its heat balance is then,

$$P_{in} = P_{out}$$
$$g_t(T_t - T_s) = g_r(T_s - T_r)$$

Knowing the heat balance of the sensor enables the prediction of an unknown target temperature from the sensor and reference temperature as,

$$T_t = T_s + \frac{g_r}{g_t}(T_s - T_r) \tag{2.12}$$

In the case that $g_t = g_r$, the sensor temperature will exactly be in between the target and reference temperature. When for example $T_t = 300$ [K] and $T_r = 296$ [K], the sensor temperature will be 298 [K].
The general thermal imager system thus contains a reference and a sensor object which are placed close to the target object. The small distance between target and sensor should make the use of lenses as used in conventional thermal imagers, unnecessary. Up to now only the overall uniform temperature of a target has been considered, while in the current application the target has a temperature distribution across its surface. This requires the sensor to measure at different points on its surface and thereby creating spatial resolution. Establishing this spatial resolution is discussed in section 2.4.

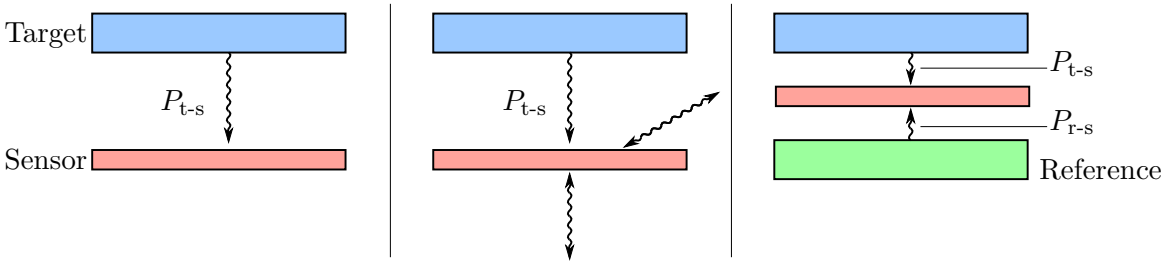

Figure 2.5: Schematic drawings showing at the *left* radiation ideally comes only from the target to the sensor, but the *middle* shows that the sensor can also receive heat from its side and bottom. The *right* shows that in order to know all heat influences on the sensor, a reference object is placed underneath the sensor and all objects are placed very close to each other to minimize radiation from the side.

2.4 General pixel model

The sensor object of figure 2.5 consists of a two-dimensional array of pixels. These temperature sensitive pixels exchange heat with the target and reference which determines their temperature. The temperature of each pixel ideally indicates the temperature of a point on the target which is directly opposed to that pixel. In that way spatial resolution is created in the sensor and a temperature distribution image of the target can be made. This section looks into the structure and thermal behaviour of the pixel.

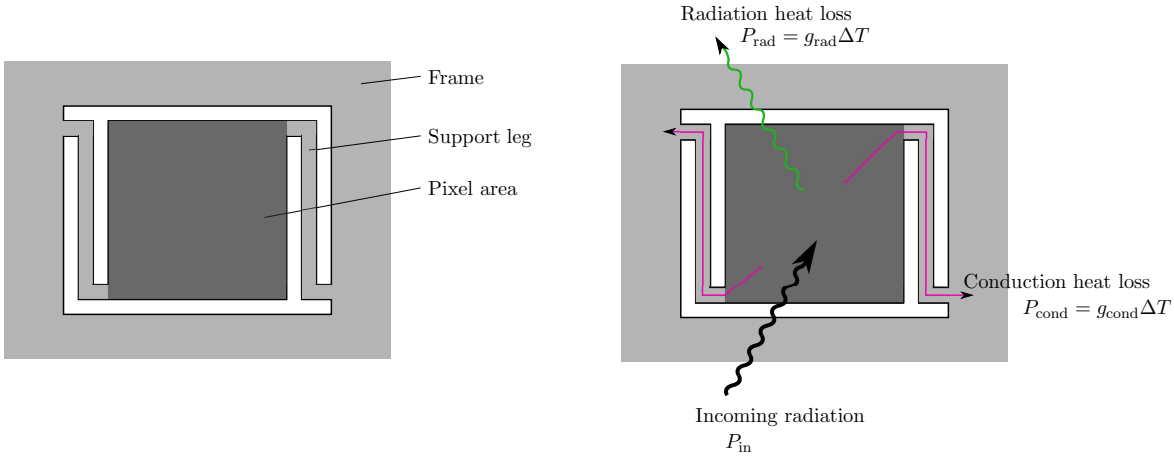

(a) Pixel structure

(b) Pixel heat exchange

Figure 2.6: Schematic drawings of a pixel showing its components and the heat flow to and from the pixel.

2.4.1 Pixel structure

Each pixel consists of a radiation absorbing pixel area connected to a supporting substrate or frame, as shown in figure 2.6a. Radiation falling on a pixel is absorbed, causing an increase in temperature. From the pixel, the absorbed heat can flow to the surroundings of the pixel. There are two potential types of heat loss from the pixel; conduction and radiation.

Conduction can take place in two ways:

1. Heat can flow from the pixel via its support legs to the frame.

2. Heat may be able to flow directly from one pixel to a neighboring pixel if the pixels are directly adjacent to each other. This is to be avoided because it reduces the spatial resolution.

Radiation occurs as heat exchange between the pixel and its surroundings. If the principle heat loss mechanism is by radiation, the pixel is said to be at the 'background limit', the limit fundamental to its performance. In the ideal case this is the only limit on its thermal performance.
So in order to obtain high performance, the pixels should not be directly adjacent to each other but thermally isolated and the principle heat loss mechanism should be by radiation. This means that conduction heat transfer should be as small as possible.

2.4.2 Pixel heat balance

The performance of a pixel is mainly determined by its heat balance. Determining the heat balance of a pixel is the subject of this section.

General pixel heat balance

Let the pixel have a heat capacity of C. Let the total heat transfer coefficient of the pixel be G. This heat transfer coefficient accounts for radiation and conduction heat loss from the pixel. Let a time varying heat radiation of power amplitude P_0 fall on the pixel. Let the fraction of incident radiation that is absorbed be η. Let the frequecy of the time varying heat radiation be ω. Let the temperature increase of the pixel above the temperature of its environment be ΔT_{p}. The heat balance of the pixel then becomes,

$$C\frac{\mathrm{d}(\Delta T_{\mathrm{p}})}{\mathrm{d}t} + G(\Delta T_{\mathrm{p}}) = \eta P_{\mathrm{in}} = \eta P_0 \mathrm{e}^{j\omega t} \tag{2.13}$$

where P_{in} is the radiation incident on the pixel, $j = \sqrt{-1}$ and t is time [6]. This equation assumes that power dissipation due to applied electrical bias through the pixel's detector can be neglected. The solution of the temperature increase of the pixel above its surroundings from equation 2.13 is,

$$\Delta T_{\mathrm{p}} = \frac{\eta P_0 \mathrm{e}^{j\omega t}}{G + j\omega C} = \frac{\eta P_0}{G(1+\omega^2\tau^2)^{1/2}} \tag{2.14}$$

where τ is the thermal response time of the pixel, which is defined as

$$\tau = \frac{C}{G} \tag{2.15}$$

Equation 2.14 shows that the temperature increase of the pixel increases and decreases as the input radiant power rises and falls in an oscillatory manner. At low frequencies for which $\omega\tau \ll 1$ the temperature increase is,

$$\Delta T_{\mathrm{p}} = \frac{\eta P_0}{G}$$

At high frequencies for which $\omega\tau \gg 1$ the temperature increase is,

$$\Delta T_{\mathrm{p}} = \frac{\eta P_0}{\omega C}$$

So for low frequencies the temperature increase is dependent on the total heat transfer coefficient G, at high frequencies it is dependent on the frequency ω and heat capacity C and in the transition region between low and high frequencies it is characterized by the thermal repsonse time τ.

Detailed pixel heat balance

Figure 2.6b denotes that heat loss from the pixel can occur in two ways; as conduction down the pixel's support legs to the frame or as radiation to its surroundings. The surroundings of the pixel consist mainly of a target object and a reference object as shown in figure 2.5. It is assumed that radiation from the open sides between target, sensor and reference is negligable. This assumption is discussed further in appendix B. Heat exchange by radiation is thus determined by the target, pixel and reference. Recalling that heat exchange between objects can be written as a heat transfer coefficient times a temperature difference between the objects, the pixel heat balance can be written as,

$$C\frac{\mathrm{d}T_\mathrm{p}}{\mathrm{d}t} = g_\mathrm{t}(T_\mathrm{t} - T_\mathrm{p}) + g_\mathrm{r}(T_\mathrm{r} - T_\mathrm{p}) + g_\mathrm{f}(T_\mathrm{f} - T_\mathrm{p}) \tag{2.16}$$

where g_t, g_r, g_f are the heat transfer coefficients from target, reference and frame to the pixel, respectively. Note also that conduction is thus governed by $g_\mathrm{cond} = g_\mathrm{f}$, radiation is governed by $g_\mathrm{rad} = g_\mathrm{t} + g_\mathrm{r}$ and that the total heat exchange of the pixel depends on,

$$G = g_\mathrm{t} + g_\mathrm{r} + g_\mathrm{f} \tag{2.17}$$

To get better insight into the influence of the target, reference and frame on the pixel temperature the heat balance is divided by the total heat transfer coefficient of the pixel G.

$$\tau\frac{\mathrm{d}T_\mathrm{p}}{\mathrm{d}t} = r_\mathrm{t}(T_\mathrm{t} - T_\mathrm{p}) + r_\mathrm{r}(T_\mathrm{r} - T_\mathrm{p}) + r_\mathrm{f}(T_\mathrm{f} - T_\mathrm{p}) \tag{2.18}$$

where r_t, r_r, r_f are the ratios of the target, reference and frame heat transfer coefficient to the total heat transfer coefficient, respectively. If for example the target coefficient ratio is large compared to the ratios of reference and frame, the pixel temperature mainly depends on the target temperature. This is of course the desired situation because the goal is to measure target temperature. To make the effect of these coefficient ratios more clear the target temperature is resolved from equation 2.18 in the case of steady state ($\frac{\mathrm{d}T_\mathrm{p}}{\mathrm{d}t} = 0$) as,

$$T_\mathrm{t} = T_\mathrm{p} + \frac{1}{r_\mathrm{t}}\{r_\mathrm{r}(T_\mathrm{p} - T_\mathrm{r}) + r_\mathrm{f}(T_\mathrm{f} - T_\mathrm{r})\} \tag{2.19}$$

Again this shows that when the target heat transfer coefficient g_t is large compared to the other heat transfer coefficients its ratio r_t to the total heat transfer coefficient G is large and consequently target temperature is mainly indicated by the pixel temperature.
Now that the influences on the pixel temperature are known the question is how the pixel temperature is measured. Generally the pixel temperature is measured across the pixel area by a detector. This detector is discussed in section 2.5.

2.5 Detector

The detector is the element contained in a pixel which measures the temperature of the pixel. The properties of this detector are discussed in this section.

2.5.1 Detector material

In section 2.3.1 some types of detectors have been discussed and it was stated that according to literature the detector providing the best thermal performance is a resistive bolometer. A resistive bolometer consists of a material which has an electrical resistance which is strongly dependent on temperature. This property is used to convert temperature into an electrical output. Types of resistive bolometers are resistance temperature detectors (RTD) and thermistors, which differ in material type. RTDs are made of a metal, while thermistors are made of a semiconductor material. The material type determines the sensitivity of the element's resistance to temperature. For small temperature increments the resistance change ΔR is linear with temperature change ΔT, that is,

$$\Delta R = \alpha R \Delta T \tag{2.20}$$

where R is the detector's nominal resistance and α is the temperature coefficient of resistance (TCR) in [K^{-1}]. For metals at room temperature the TCR is positive, for semiconductors at room temperature it is usually negative. The TCR of semiconductors at room temperature is approximately ten times higher than the TCR of metals. Therefore thermistors are the most suitable detector when small temperature resolution is required. For a thermistor the TCR is approximately 0.02 to 0.06 [K^{-1}]. The semiconductor material used in thermal cameras is vanadium oxide (VO_2 or V_2O_5) or amorphous silicon (a-Si).

2.5.2 Detector resistance-temperature relationship

R-T relationship

Equation 2.20 shows an approximate description of the resistance-temperature (R-T) relationship of the detector (thermistor). A more accurate description of the R-T relationship of a thermistor is given by the Steinhart-Hart equation [7],

$$T^{-1} = A + B\ln(R) + C(\ln(R))^3 \tag{2.21}$$

where T is the thermistor temperature in [K], R the thermistor resistance in [Ω] and A, B, C are constants. The constants A, B and C can be obtained through calibration and equation 2.21. Using three calibration points the calibration values of equation 4.3.1 can be calculated. Provided a sufficiently accurate reference, a calibration with three calibration points will result in an absolute temperature error of 1 [mK] or less within the calibrated temperature range [8].

Detector output signal

By applying a constant bias current I_b through the thermistor a voltage establishes across the resistance of the thermistor. This voltage is the output signal of the thermistor and is

proportional to the magnitude of the thermistor resistance. Consequently the voltage output signal indicates the temperature of the thermistor. Using the simplified R-T relationship of equation 2.20 the voltage output signal for a temperature change of the thermistor is given by,

$$V_s = I_b \alpha R \Delta T \tag{2.22}$$

The constants in this equation $I_b \alpha R$ are sometimes referred to as the detector sensitivity.

Detector self-heating

The bias current across the detector causes Joule heating in the resistance of the detector ($P_{self} = I_b^2 R$). This causes the detector to affect its own temperature by introducing an additional heat input. Due to the fact that the bias current is constant and known and the voltage across the detector is measured, the influence of self-heating can be accounted for. It is however important to keep the self-heating of the detector as low as possible.

2.5.3 Detector distribution across the pixel

Ideally the voltage output signal of equation 2.22 indicates the temperature of the entire pixel. This means that either the temperature of the pixel should be uniform or the resistance and current flow should be distributed uniformly across the pixel. Temperature uniformity of the pixel is discussed in section 2.6.6, in this section the resistance and current distribution is considered.
The thermistor material is spread across the area of the pixel. As a consequence the electrical resistance of this material is also spread across the pixel area. The bias current is provided to the detector via the support legs of the pixel, shown in figure 2.6a. Ideally the current will then be distributed uniformly across the resistance of the detector material, but this may not be the case. The flow of the current across the pixel area is therefore an important issue for further research. In general however it is favourable to make sure that the temperature of the pixel can be assumed uniform.

2.6 Performance indicators

From the heat balance of the pixel which is shown in section 2.4.2 some indicators for the performance of a pixel can be extracted. The performance indicators are discussed in this section. The outcome of the performance indicators for the proposed concept is the subject of chapter 3. Additional dimensions and material properties used in this section ar given in appendix A.2.1.

2.6.1 Response time

The response time τ of the pixel determines the speed of response of the pixel temperature to a changing heat input. As such the maximum frequency in time to which a changing heat input can be measured is determined by the response time. In the case at hand a response time of 1 [s] is required. The response time is determined by the heat capacity C and total heat transfer coefficient G of the pixel and is given by,

$$\tau = \frac{C}{G} \tag{2.23}$$

Furthermore the heat capacity depends on the volume V, density ρ and specific heat capacity c_p of the pixel as,

$$C = \rho A t c_p$$

where the pixel volume is written as area times thickness, $V = At$. Density and specific heat capacity are material properties and are therefore determined by the choice of detector. At a certain pixel area, the pixel thickness can increase or decrease the heat capacity and consequently the response time. Finally, the heat transfer coefficient G depends on the conduction and radiation heat transfer coefficients of the pixel as,

$$G = g_{\text{cond}} + g_{\text{rad}}$$

Increasing G decreases response time, which happens when the pixel area is increased. The heat transfer coefficient is discussed in more detail in section 2.6.2. Figure 2.7a shows the response time versus pixel thickness for a pixel area of 3x3 [mm], which is a suitable pixel size in terms of thermal resolution as will be shown in section 2.6.5. For this pixel area the thickness should be less than 7 [μm] to meet the required response time. Figure 2.7b shows that for a pixel of 6 [μm] thick the response time stays within the required range up to about 10 [mm] pixel width.

2.6.2 Heat transfer coefficient

The total heat transfer coefficient G determines how well the pixel exchanges heat with its environment and depends on conduction and radiation. The influence of pixel geometry and material properties on G is given as,

$$\begin{aligned} G &= g_{\text{cond}} + g_{\text{rad}} \\ &= 2\frac{kA_{\text{leg}}}{L_{\text{leg}}} + 4\sigma\varepsilon T^3(2A_{\text{p}}) \end{aligned} \tag{2.24}$$

where k is the thermal conductivity of the two support legs, A_{leg}, L_{leg} are the cross-sectional area and length of the support legs and A_{p} is the pixel area. For an optimal pixel performance the conduction must be minimized and therefore A_{leg} should be small and L_{leg} should be large. In literature a minimum support leg thickness and width of 0.01 times the pixel width and a

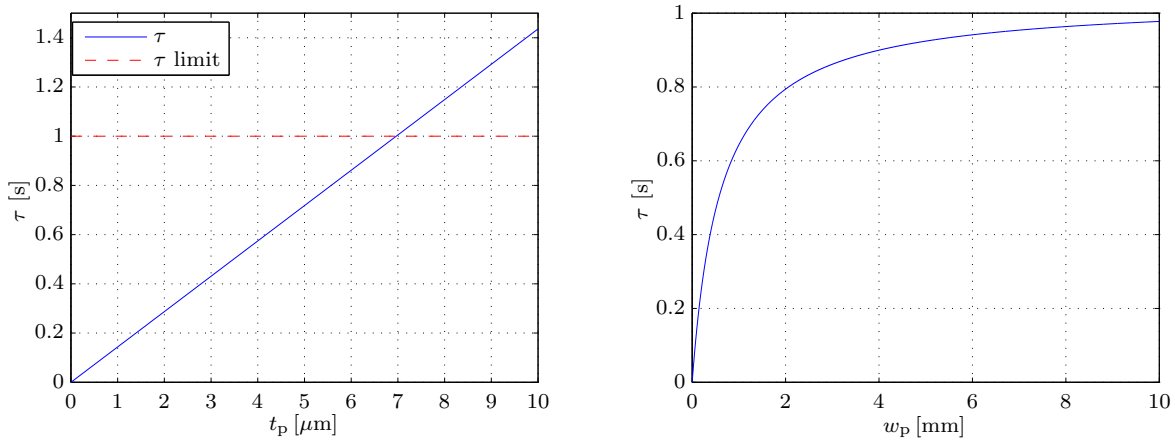

(a) Response time vs pixel thickness ($w_p = 3$ mm)

(b) Response time vs pixel width ($t_p = 6$ μm)

Figure 2.7: Response time versus pixel thickness for a pixel area of 3x3 [mm], showing that the response time requirement limits the thickness to 7 [μm]. Also showing response time versus pixel width for a pixel thickness of 6 [μm].

leg length equal to pixel width is given [6]. This results in a rewritten equation for G which is mainly dependent on pixel width w_p and is given by,

$$2k(0.01)^2 w_p + 4\sigma\varepsilon T^3 2(w_p)^2$$

This equation and figure 2.8a show that for very small pixel width conduction is dominant but by increasing the width radiation becomes dominant. The ratio of the radiation and conduction heat transfer coefficients in figure 2.8b shows that at a pixel width of 6 [mm], g_{rad} is 10 times larger than g_{cond} and conduction is then negligable compared to radiation.

2.6.3 Responsivity

The responsivity shows the change in the pixel's electrical output signal for a change in heat radiation falling on the pixel. A high responsivity thus indicates that the pixel is very sensitive to incoming radiation. The temperature change of a pixel to a changing radiation heat input was derived in section 2.4.2 into equation 2.14 as,

$$\Delta T_p = \frac{\eta P_0}{G(1+\omega^2\tau^2)^{1/2}}$$

The voltage output signal of the detector for the temperature change of the pixel is given by equation 2.22 as,

$$V_s = I_b \alpha R \Delta T_p$$

Recalling that the responsivity $\Re$ is the output signal for a change in radiation input, it is given by,

$$\Re = \frac{I_b \alpha R \eta}{G(1+\omega^2\tau^2)^{1/2}} \tag{2.25}$$

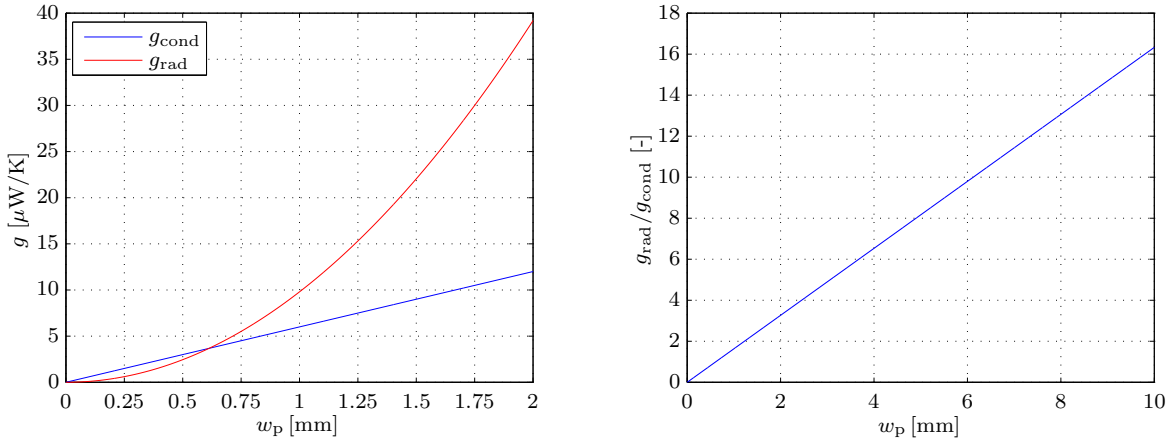

(a) Heat transfer coefficients

(b) Coefficient ratio

Figure 2.8: Plots showing the conduction and radiation heat transfer coefficients of a pixel and their ratio as a function of pixel width. At a pixel width of 0.6 [mm] the coefficients are equal and for increasing pixel width g_{rad} becomes significantly larger than g_{conv}.

The responsivity is plotted for a steady state situation ($\omega = 0$) against pixel width in figure 2.9a which shows that the responsivity strongly decreases with pixel width due to the increase of the heat transfer coefficient. An increase of the frequency ω of the heat input causes the responsivity to decrease as shown in figure 2.9b for a pixel width of 3 [mm].

2.6.4 Noise

Noise in the output signal of the detector limits the resolution of the detector's temperature measurement. When a certain temperature change causes a signal output voltage V_{s} smaller than the noise voltage V_{n} the temperature change is not detected. It is said that the signal-to-noise ratio is than lower than 1. Noise sources influencing radiation detector performance are temperature fluctuation noise, Johnson noise and 1/f noise [4]. The equations governing these noise sources and their magnitude for the concept design are discussed in appendix A.2.2. For a radiation detector a typical rms value for the noise voltage is 1 [μV] [6].

2.6.5 Thermal resolution

For thermal imagers the thermal resolution is often described in terms of the noise equivalent temperature difference *NETD*. The thermal resolution of the imager is determined by the resolution of its pixels. *NETD* is defined as the change in temperature of a large blackbody in the field of view of a pixel that will cause the signal-to-noise ratio at the output of the pixel to change by unity.
Considering the application of the thermal imager, the area of interest on a target for one

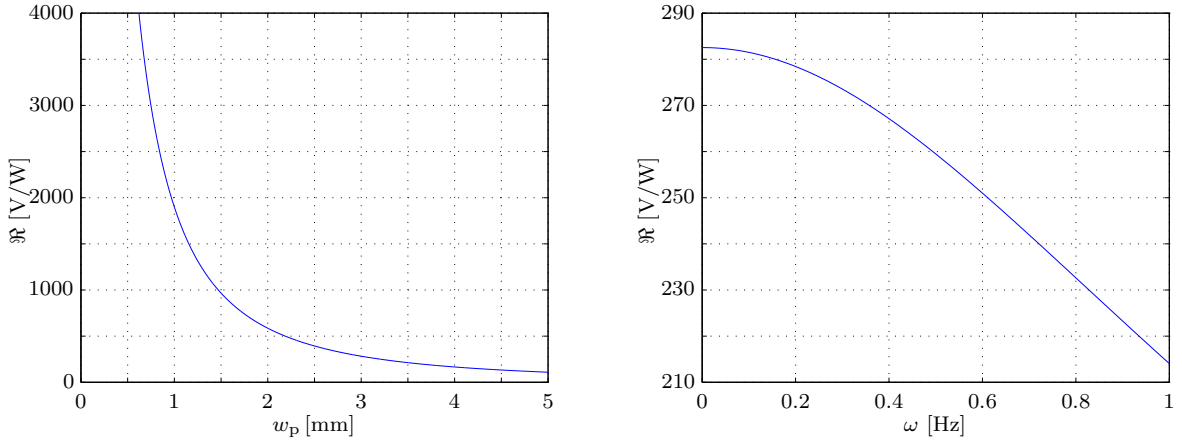

(a) Responsivity versus pixel width ($\omega = 0$)

(b) Responsivity versus frequency ($w_p = 3$ mm)

Figure 2.9: Plots showing the decrease of responsivity of a pixel with increasing pixel width in steady state and with increasing frequency of the radiation input at a pixel width of 3 [mm].

pixel is determined by the required spatial resolution of 10 [mm] and the Nyquist criterion. Defining the inverse of the required spatial resolution as the maximum spatial frequency of interest $f_{i,max}$ and the Nyquist frequency as half the measurement frequency ($f_N = \frac{f_m}{2}$). The required measurement frequency is then given by [9],

$$f_{i,max} < f_N = \frac{f_m}{2} \Leftrightarrow f_m > 2f_{i,max} \tag{2.26}$$

The width of the measurement area of interest on a target is thus the inverse of this measurement frequency. As a consequence the area of interest on a target for one pixel is smaller or equal to 5x5 [mm]. In the definition of the *NETD* the target is a blackbody for which the emitted radiation per area is given by equation 2.4. The change in emitted radiation per area to a change in temperature of the blackbody is $\frac{dE_{bb}}{dT_{bb}} = 4\sigma T^3$. In section 2.2.3 it was shown that of two objects facing each other not all radiation leaving one object reaches the other object. The fraction of radiation leaving object 1 that reaches object 2 can be described by a view factor F_{1-2}. The change in radiation from the target's area of interest A_{bb} due to a temperature change that reaches the pixel is thus given by,

$$\frac{dP_{bb\text{-}p}}{dT_{bb}} = 4\sigma T^3 A_{bb} F_{bb\text{-}p} \tag{2.27}$$

Note that due to the reciprocal rule of view factors $A_{bb}F_{bb\text{-}p} = A_p F_{p\text{-}bb}$. The *NETD* is the temperature change of the area of interest on the blackbody that causes the pixel to produce an output voltage equal to the noise voltage. Combining equations 2.22, 2.14, 2.25, 2.27 and the reciprocal rule, the *NETD* can be found as,

$$NETD = \frac{V_n}{\Re\, A_p\, F_{p\text{-}bb}\, \frac{dE_{bb}}{dT_{bb}}} \tag{2.28}$$

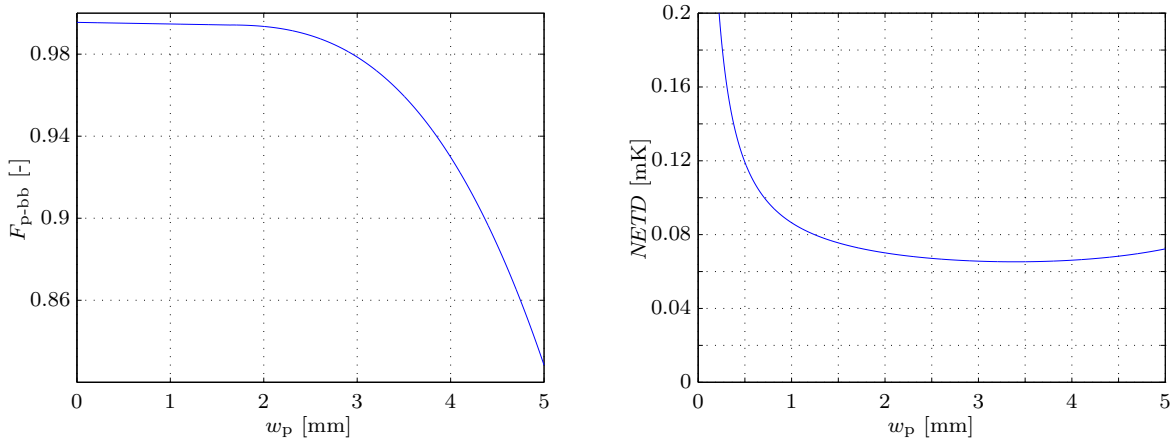

(a) View factor $F_{\text{p-bb}}$ (b) *NETD*

Figure 2.10: Plots of the view factor from pixel to the blackbody area of interest and *NETD* versus pixel width. At a pixel width of 3.5 [mm] the *NETD* is at a minimum of approximately 0.06 [mK].

The view factor of the pixel to the area of interest on the blackbody A_{bb} is plotted against pixel width in figure 2.10a. The distance between pixel and target is taken as 0.5 [mm]. It shows that the view factor decreases with increasing pixel width. The *NETD* is plotted against pixel width in figure 2.10b. Up to a pixel width of 1 [mm] the *NETD* strongly decreases due to the increase of pixel area. Above a pixel width of 1 [mm] the radiation heat transfer coefficient g_{rad} becomes significantly larger than the conduction heat transfer coefficient g_{cond}. The *NETD* can in that case be approximated by,

$$NETD \approx \frac{V_{\text{n}}}{I_{\text{b}} \alpha R F_{\text{p-bb}}} \qquad \text{when } g_{\text{rad}} \ll g_{\text{cond}}$$

The terms V_{n}, I_{b}, α and R are constant and therefore in this case the view factor determines the course of the *NETD*. The view factor decreases for increasing pixel width and consequently the *NETD* increases. This causes the thermal resolution of the pixel to have a minimum of about 0.06 [mK] at a pixel width of 3.5 [mm].

2.6.6 Pixel temperature uniformity

In section 2.5.2 the measurement of pixel temperature by an output voltage across the resistance of the detector has been explained. Section 2.5.3 explained that the uniformity of the current flow across the pixel is uncertain. Therefore it is important that the pixel temperature is uniform to make sure that the measured pixel temperature is indeed the temperature of the total pixel. An indication of the temperature uniformity of an object is given by the Biot number which is the ratio between the internal heat flow resistance and the external heat flow resistance of an object. When the external resistance is much higher than the internal resistance the object can

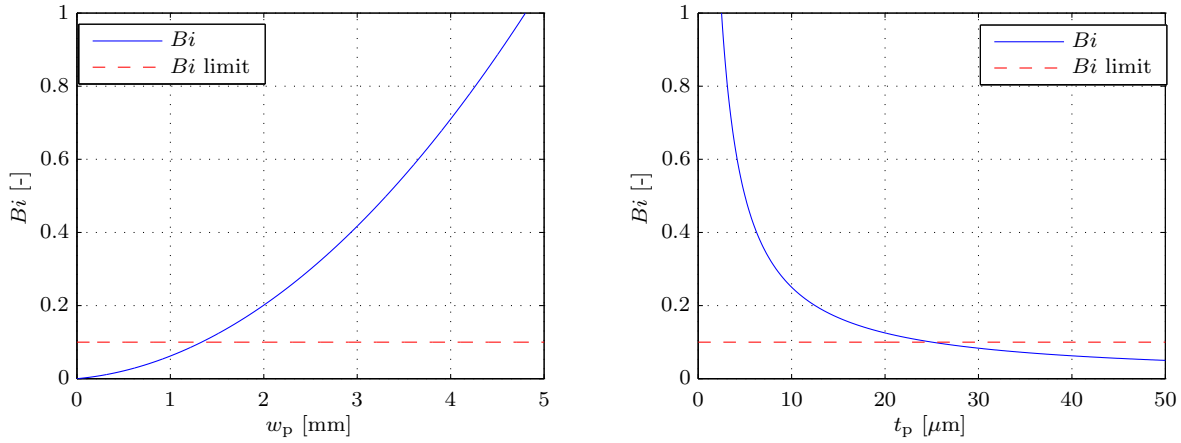

(a) Bi versus w_p ($t_p = 6$ μm) (b) Bi versus t_p ($w_p = 3$ mm)

Figure 2.11: Plots showing the Biot number number versus pixel width and pixel thickness. A Biot number below 0.1 indicates that the pixel can be assumed to have a uniform temperature.

be assumed uniform in temperature. The Biot number is given by,

$$Bi = \frac{R_{\text{in}}}{R_{\text{out}}} = \frac{\frac{L_c}{kA_c}}{\frac{1}{G}} \tag{2.29}$$

where L_c and A_c are a charachteristic length and cross-sectional area of the object through which heat flows internally and G is the total heat transfer coefficient with the environment of the object. For a pixel, G is already known and as a characteristic length half of the pixel's diagonal is chosen. The characteristic area is taken as the pixel width times its thickness t_p. As a rule of thumb it is said that the temperature of an object can be assumed uniform if the Biot number is below 0.1, therefore the requirement for the pixel becomes,

$$Bi = \frac{\sqrt{\frac{1}{2}}G}{kt_p} < 0.1$$

Figure 2.11a shows the Biot number increases with pixel width which is caused by the increase of the heat transfer coefficient G. Above a pixel width of 1.3 [mm] pixel temperature can no longer be assumed uniform. Figure 2.11b shows that the Biot number decreases with increasing pixel width because this lowers the internal heat flow resistance. For a pixel width of 3 [mm] the pixel thickness should be larger than 25 [μm] to meet the Biot number requirement for a uniform temperature.

CHAPTER 3

Optimal design

An optimal design of a thermal imager with respect to the proposed specification shown in section 1.2 is required. This means that the thermal imager should have a thermal resolution of at least 1 [mK] at a spatial resolution of 10 [mm] and a response time of 1 [s]. Section 2.6 provides indicators on which the performance of a design of the concept can be evaluated. Also from these indicators a design path or design steps can be deduced. These design steps are given and discussed in section 3.1. Subsequently the performance of the design derived from the design steps is shown in section 3.2 and further discussed in section 3.3.

3.1 Design steps

The following design considerations need to be considered:

Spatial resolution

The spatial resolution together with the Nyquist criterion determines the area of interest on a target for one pixel as dicussed in section 2.6.5. Thereby it also puts a maximum on the pixel area A_{p} of 5x5 [mm].

Heat transfer coefficient

The pixel area and consequently its width, mainly determines the total heat transfer coefficient G of the pixel as shown in section 2.6.2. Furthermore increasing the pixel width increases the radiation heat transfer coefficient more than the conduction heat transfer coefficient. Figure 2.10b shows that this improves the thermal resolution until a pixel width of 3.5 [mm].

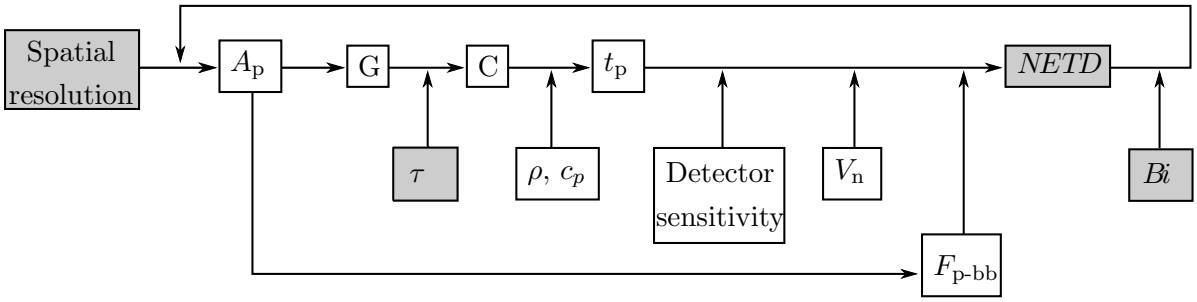

Figure 3.1: Block diagram showing the design path of the pixel with requirements in a gray box. The path starts with the spatial resolution and after one iteration towards the *NETD* subsequent iterations may be needed, amongst others due to the requirement of temperature uniformity (*Bi*).

Heat capacity - Response time

The heat capacity of the pixel depends on the volume, density and specific heat capacity of the pixel. The last two are determined by the choice of detector, the volume is partially determined by the pixel area. The pixel thickness is therefore the free variable to change the heat capacity. Moreover, because the reponse time of the pixel is determined by heat capacity and heat transfer coefficient, the pixel thickness must be chosen such that the response time requirement is met.

Detector

The detector determines the sensitivity of the output signal to temperature change of the pixel as shown in section 2.5.2. This detector sensitivity directly influences the achievable thermal resolution. The other factor directly influencing thermal resolution is the noise voltage. Generally the largest part of the noise voltage is determined by the pixel and its read-out electronics.

View factor

The view factor determines how much of the radiation that leaves the area of interest on a target actually reaches the pixel, as stated in section 2.6.5. Ideally the view factor of the pixel to the area of interest is 1, which means that all radiation leaving that area reaches the pixel. Figure 2.10a shows that increasing pixel width, decreases this view factor. The view factor thereby limits the advantage of increasing pixel width.

Temperature uniformity

Section 2.5.3 discussed that the pixel temperature should ideally be uniform. Figure 2.11 shows that assuming a uniform pixel width is only valid below certain pixel width and above a certain pixel thickness. This criterium therefore puts a limit on the pixel width and thickness.

These considerations can be combined into a useful design path, which is shown in figure 3.1.

3.2 Concept performance

By following the path of figure 3.1 the design described in table 3.1 is chosen for the thermal imager concept.

Properties					
Pixel width	w_{p}		[mm]	1	
Pixel thickness	t_{p}		[μm]	9	
Heat capacity	C		[μJ/K]	15.2	
Conduction heat transfer coefficient		g_{cond}	[μW/K]		6
Radiation heat transfer coefficient		g_{rad}	[μW/K]		9.8
Total heat transfer coefficient	G		[μW/K]	15.8	
View factor	$F_{\mathrm{p\text{-}bb}}$		[-]	0.99	
Performance					
Spatial resolution	Spatial res.		[mm]	5	
Response time	τ		[s]	0.97	
Thermal resolution	*NETD*		[mK]	0.09	
Temperature uniformity	*Bi*		[-]	0.04	

Table 3.1: Properties and performance of the design concept.

3.3 Discussion and conclusion

There are some points of discussion for the design which is shown in section 3.2.

- The thermal resolution (*NETD*) could be lower if the temperature uniformity of the pixel would not be an issue. Currently the pixel width is chosen smaller than would be ideal for the thermal resolution, to satisfy the required Biot number. The thermal resolution is however still well within the required value.
- The response time is just within the requirement. Response time can be brought down by making the pixel thinner up to about 4 [μm] after which the Biot number becomes too large. The current thickness is chosen larger than 4 [μm] in view of the manufacturability of the pixel. The pixel thickness is now about 100 times smaller than the width, which is the same thickness-width ratio as pixels of conventional thermal cameras have.
- The estimation of the noise voltage used in the performance calculation is uncertain because the mechanisms behind 1/f noise are not generally understood yet. The 1/f noise

is potentially the main noise source for this design. A larger noise voltage would directly decrease the thermal resolution.

Summarizing, all the three requirements set for the thermal imager are met by the current concept design. There even appears some to be some room to improve one of the performance numbers if it would turn out to be threatened. The manufacturability of this concept seems achievable but needs further research.

CHAPTER 4

Experimental validation

In section 2.3.1 the performance of conventional thermal imagers was discussed, which showed that their thermal resolution is a factor 10 above the requirement of the application at hand. The proposed concept showed to have a theoretical performance well within the proposed specification. The main reason for the improvement of thermal resolution with respect to conventional imagers is the increase of the pixel area. This causes two favourable effects. First, the area for absorbing radiation from a target is larger, so more radiation is absorbed by the pixel for a certain temperature change of the target. Secondly, the area increase makes the pixel more sensitive to the target temperature compared to temperature of other objects in the pixel's surroundings.
The goal of validation by experiments is two fold:

1. Prove that the principle of the proposed concept works and that temperature changes of a target object in the order of milliKelvins can be measured.

2. Validate that the increase of pixel area makes the pixel more sensitive to the temperature of the target than temperature of other objects in its surroundings.

This section discusses the experimental validation. In section 4.1 the proposed validation is treated, after which the setups that have been used are explained and shown in section 4.2. The calibration and determination of temperature resolution of the used thermistors is discussed in section 4.3. With these thermistors experiments are performed to see the influence of pixel size on thermal performance. The thermal response time of the pixel is treated in section 4.4 and the thermal resolution is discussed in section 4.5. Extensive dimensions and properties of the components used in the experiments are listed in appendix C.1.

4.1 Proposed validation

Making a prototype according to the design proposed in section 3.2 would require extensive research on the manufacturability which is beyond the scope of this research. Therefore the concept is scaled up to a thickness for which detectors (thermistors) are readily available. With these thermistors the following experiments have been carried out.

Thermistor performance

To be able to do measurements with the thermistors, their behaviour must be characterised first. Two experiments are therefore done with the thermistors only.

- Calibration of the thermistors with respect to a reference thermometer. The calibration must enable the thermistors to detect temperature differences in the milliKelvin range.
- Determination of the temperature resolution of the thermistors. The temperature resolution of the thermistor determines the smallest temperature difference they can measure.

Pixel performance

After characterisation of the thermistors, one thermistor is attached to a foil which is varied in area. The thermistor and foil together form a single pixel. The total setup consists of a single pixel varied in area, and a target, frame and reference object.

- The response time of the various pixels is determined by exposing them to a step heat input. The change of the response time with pixel area size indicates the change of the pixel's heat transfer coefficient.
- The sensitivity of the pixel to the temperature of a target is determined by putting it in between a target and a reference object. The target object is heated in steps and the accompanying temperature change of all the objects in the setup are measured. The goal is to determine the change of the ratios of the heat transfer coefficients of the pixel.

4.2 General setup

This section introduces the components and setups used in the experimental validation.

4.2.1 Calibration and resolution setup

A photo of the thermistors used in the experiments is shown in figure 4.1a. The actual size of one thermistor bead is 0.8x1.4 [mm].

The calibration setup contains the following components:

- Thermistors as shown in figure 4.1a.
- A mercury-in-glass thermometer used as a reference sensor for the calibration, shown in figure 4.2.
- An aluminium block, which contains nine holes up to its center, each for one thermistor. Another hole in the block is intended for the reference thermometer. The block with thermistors and thermometer is shown in figure 4.2.
- A Peltier element used to heat and cool the aluminium block. The Peltier element is shown in figure 4.1b. The Peltier element is removed after heating or cooling, so is not attached to the block during the actual calibration.
- Foam placed around the aluminium block to minimize heat exchange with the environment during calibration.

In the resolution experiment a temperature gradient is established along the width of the aluminium block. The setup consists of the following components:

- Thermistors as shown in figure 4.1a.
- The same aluminium block as used in the calibration experiment. In this case with 3 thermistors in the center of the block and one thermistor at each outer side of the block. The inner thermistor are spaced at a small distance in the width direction. The outer thermistors are used to control the temperature at either side of the block.
- Two Peltier elements to continuously control the temperature at either side of the block.
- Foam placed around the aluminium block to minimize heat exchange with the environment during the experiment.

(a) Thermistor (b) Peltier element

Figure 4.1: Photo of a thermistor and a Peltier element. The actual size of the thermistor is 0.8x1.4 [mm] and of the Peltier element 40x40 [mm].

4.2.2 Response time and thermal resolution setup

For the experiments performed to see the influence of varying pixel area, a thermistor is attached to an aluminium foil. This aluminium foil is varied in size and as such the pixel area is

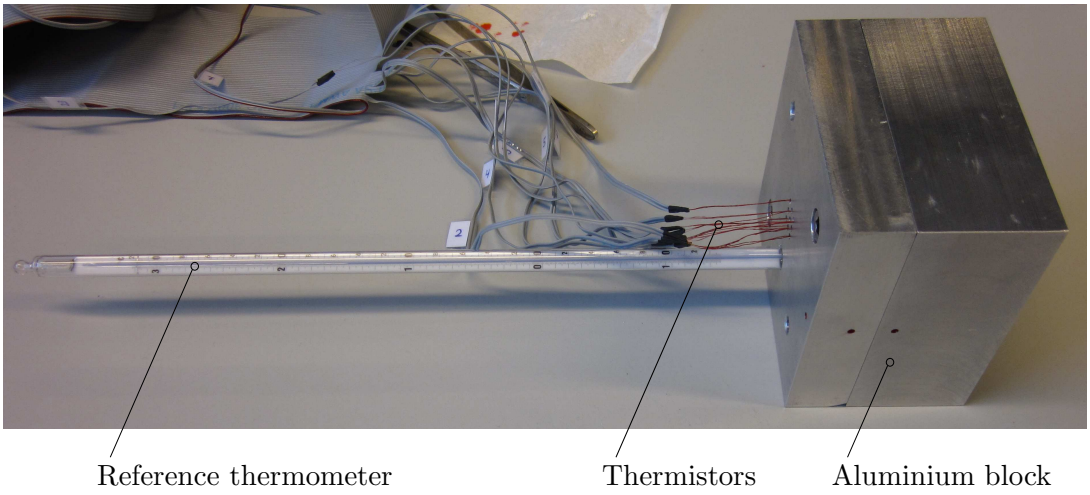

Figure 4.2: Photo showing the main components of the calibration and the resolution setup.

varied. The thermistor is put in a plastic container which is supported by slender legs that are attached to a frame. The aluminium foil is attached to the thermistor and container with some thermal paste. The pixel frame is kept at a approximately 2 [mm] distance from a target and reference object by a plastic holder. The holder with the reference and pixel frame containing a thermistor, is shown in figure 4.3.

The response time setup is shown in figure 4.4a and consists of the following components:

- A pixel consisting of a thermistor, a thermistor container and an aluminium foil sprayed black on both sides. The components are attached to each other with thermal paste.
- A reference object made of a 6 [mm] thick plate of aluminium. The side facing the pixel is sprayed black and at the other sides holes are drilled to just below the side facing the pixel. These holes contain thermistors to measure the surface temperature of the reference.
- A holder, keeping pixel and reference at 2 [mm] distance.
- A vacuum box in which the whole setup is put.
- A beamer outside the vacuum box, used to create a step heat input on the pixel as shown in figure 4.4a.

The thermal resolution setup is shown in figure 4.4b and consists of the following components:

- A pixel which can be varied in area.
- A reference object which is also used in the response time experiment.

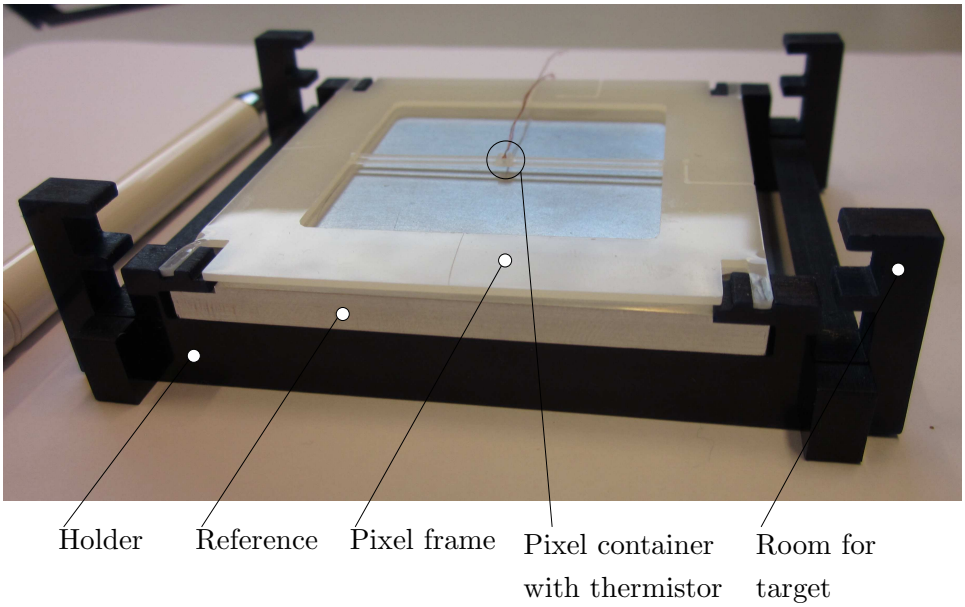

Figure 4.3: Holder with the reference object and the pixel frame. The pixel frame carries a container with a thermistor on long slender legs. The size of the reference object is 70x70x6 [mm].

- A target object made of a 6 [mm] thick aluminium plate, sprayed black at its front and back side. At the front side (facing the beamer) holes are drilled to just below the back surface to measure the target's surface temperature.
- A holder, keeping pixel, reference and target each at 2 [mm] distance.
- A vacuum box in which the whole setup is put.
- A beamer outside the vacuum box, used to heat the target across its full front area.

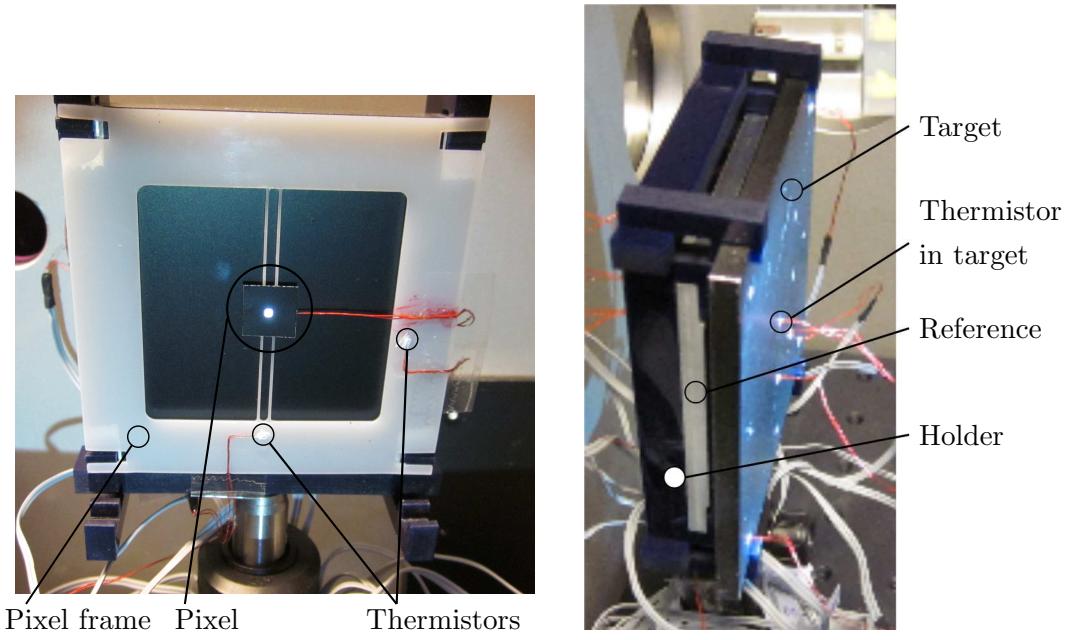

(a) Response time setup (b) Thermal resolution setup

Figure 4.4: *Left:* Front view of the response time setup with a 10x10 [mm] pixel which is exposed to a small light dot at its center. *Right:* Side view of the thermal resolution setup showing the target with thermistors in it and being exposed to light across its full area.

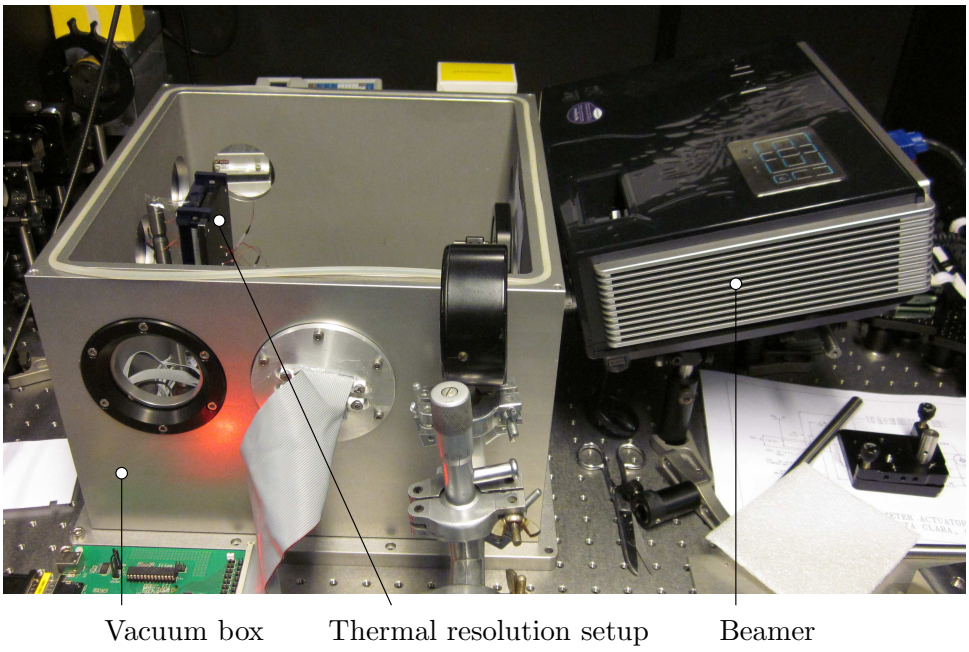

Figure 4.5: Photo of the thermal resolution setup in the vacuum box. In front of a window in the vacuum box the beamer is placed.

4.3 Component performance

This section discusses the calibration of the thermistors in section 4.3.1 and the determination of the resolution of the thermistors in section 4.3.2.

4.3.1 Thermistor calibration

Introduction

The detector is the temperature measurement element in each pixel of the thermal imager and thereby determines to a large extent the achievable thermal resolution. The detector should have a high temperature sensitivity $S_{\mathrm{T,d}}$, in other words the change in the output signal ΔO_{d} must be as large as possible for a given temperature change ΔT_{d} of the detector.

$$S_{\mathrm{T,d}} = \frac{\Delta O_{\mathrm{d}}}{\Delta T_{\mathrm{d}}} \tag{4.1}$$

The smallest change in a temperature being measured that causes a perceptible change in the corresponding indication or output signal is the temperature resolution [10]. For the application at hand the temperature resolution must be better than the thermal resolution required for the thermal imager. Amongst others the temperature resolution is influenced by the temperature sensitivity of the detector, noise in the detector output signal and resolution of the A/D conversion of the detector output signal. Besides the temperature resolution, the closeness of the measured value to the true value is of importance. The difference between the true and measured value of a measurand is called the measurement error E, as shown in equation 4.2. Since the true value of a measurand cannot be known, measurement error is often calculated with respect to a certain reference or standard [10].

$$E = x_{\mathrm{meas}} - x_{\mathrm{true}} \tag{4.2}$$

Where x_{meas} is the measured value and x_{true} is the true value of the measurand. The measurement error made in a measured temperature with respect to the true absolute temperature T_{abs} will be referred to as the absolute temperature error. To make sure that the absolute temperature error of a sensor is minimal, the sensor is calibrated. This calibration is performed by comparing the indication of the sensor to a reference sensor at a number of distinct temperatures, the calibration points. After calibration the indication of the sensor shows a temperature T_{cal} which should be closer to the actual absolute temperature T_{abs}. The calibration procedure is discussed for a sensor having an output which is linearly dependent on temperature and which is calibrated at two calibration points with respect to a reference sensor. Ideally the reference doesn't have any absolute temperature error. In that case the calibrated temperature T_{cal} at each calibration point is equal to the actual absolute temperature T_{abs}. This case results in the ideal calibration curve as shown in figure 4.6a, where the red crosses denoting the indication of

the reference coincide with the actual absolute temperatures. In reality however, the reference will have an absolute temperature error E_{ref} which results in calibration temperatures that deviate from the actual absolute temperature. This yields a deviated calibration curve, shown in black, together with the ideal calibration curve in green, in figure 4.6b. The curve of figure 4.6b shows that the maximum absolute temperature error introduced by calibration, within the calibration range, is the absolute temperature error of the reference E_{ref}.

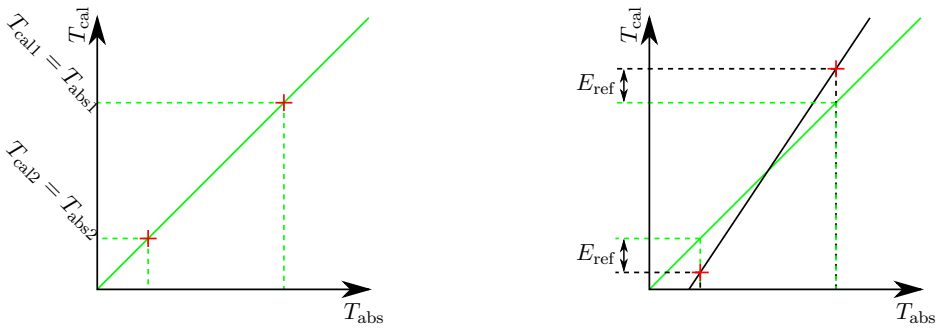

(a) Ideal

(b) Non-ideal

Figure 4.6: Calibration curves in the ideal case where calibrated temperature matches actual temperature and in the non-ideal case where an error is introduced by the absolute temperature error of the reference.

Absolute temperature is however not of specific interest. The thermal imager should only be able to detect temperature *differences* accurately. Therefore the focus should not be on absolute temperature error, but on the error made in measuring temperature differences. This temperature difference error will be termed relative temperature error and is defined as,

$$e = \Delta T_{\text{cal}} - \Delta T_{\text{abs}} \tag{4.3}$$

where e is the relative temperature error, ΔT_{cal} is the measured temperature difference after calibration and ΔT_{abs} is the actual temperature difference. The magnitude of the relative temperature error introduced in calibration is indicated by the derivative of the calibration curve. In the ideal case the calibration temperature is equal to the absolute temperature and the derivative is then given by:

$$\frac{\mathrm{d}T_{\text{cal}}}{\mathrm{d}T_{\text{abs}}} = 1$$

The absolute temperature error of the reference will however introduce an absolute temperature error in the calibration temperature. This causes an absolute temperature error in the calibration temperature equal to the absolute temperature error of the reference as shown in figure 4.6b. The relative temperature error however is dependent on the deviation of the derivative of the calibration curve from the ideal value of 1. Figure 4.7 shows the ideal calibration curve, where $\frac{\mathrm{d}T_{\text{cal}}}{\mathrm{d}T_{\text{abs}}} = 1$, in green and a non-ideal curve with a different derivative in black. The

derivative of the non-ideal curve is given by:

$$\frac{\mathrm{d}T_{\mathrm{cal}}}{\mathrm{d}T_{\mathrm{abs}}} = 1 + \varphi \tag{4.4}$$

where φ is the deviation of the derivative from the ideal value of 1. When a certain absolute temperature difference ΔT_{abs} is measured, the ideal calibration curve translates this into a measured temperature difference ΔT_{cal} which is exactly equal to ΔT_{abs}, since:

$$\Delta T_{\mathrm{cal}} = \Delta T_{\mathrm{abs}} \frac{\mathrm{d}T_{\mathrm{cal}}}{\mathrm{d}T_{\mathrm{abs}}} = \Delta T_{\mathrm{abs}}$$

The non-ideal calibration curve of which the derivative is given in equation 4.4, translates the absolute temperature difference into a measured temperature difference containing an error.

$$\Delta T_{\mathrm{cal}} = \Delta T_{\mathrm{abs}} \frac{\mathrm{d}T_{\mathrm{cal}}}{\mathrm{d}T_{\mathrm{abs}}} = \Delta T_{\mathrm{abs}}(1 + \varphi)$$

The relative temperature error is therefore dependent on the actual temperature difference T_{abs} times the derivative error φ.

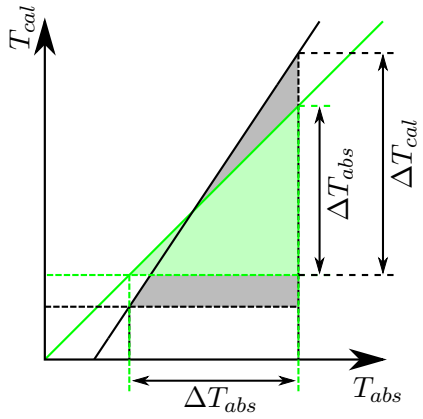

Figure 4.7: Relative error introduced in calibration, depicted in the calibration curve as the difference between ΔT_cal and ΔT_abs.

Modeling calibration errors

The detector used in this experiments are thermistors.

The supplier provides the thermistors with a data sheet containing the thermistor's rated resistance R_{r} at the rated temperature T_{r} and a material specific constant M. Also an approximate resistance-temperature relationship is given by,

$$R(T) = R_{\mathrm{r}} e^{M(1/T - 1/T_{\mathrm{r}})} \tag{4.5}$$

where $R(T)$ is the thermistor resistance depending on its temperature T and the previously stated constants. The rated resistance R_{r} and the thermistor's material constant M are subject

to manufacturing tolerances. Because of this equation 4.5 doesn't give a sufficient desciption of the thermistor's behaviour, as will be further shown in section 4.3.1. A more accurate description of the resistance-temperature relationship was given by equation 2.21 as,

$$T^{-1} = A + B\ln(R) + C(\ln(R))^3$$

The constants A, B and C which can be obtained through calibration and equation 2.21, determine the resistance-temperature relationship of a thermistor and will be further referred to as the calibration values. In this section the relative temperature error introduced in calibration is investigated. The thermistors will be calibrated against a reference which has a maximum absolute temperature error E_{ref} of ± 0.1 [K]. In section 2.5.2 it was stated that for thermistors, 3 calibration points are sufficient to obtain an accurate calibration curve. Because the temperature measurement range of the thermistors is 288 to 303 [K], 289, 295 and 302 [K] are chosen as calibration points. These points will be denoted as the maximum, middle and minimum calibration point, respectively. In the worst case scenario the absolute temperature error made in calibration is for example +0.1 [K] at the maximum and minimum calibration point and -0.1 [K] at the middle calibration point. For this scenario the resulting absolute and relative temperature error in the measured thermistor temperature, have been calculated. The absolute and relative temperature error is shown in figure 4.8a and figure 4.8b respectively. The absolute temperature error of +0.1 [K] at 289 and 302 [K] and of -0.1 [K] at 295 [K] introduced directly by the reference error, show up as expected in figure 4.8a. The relative temperature error is given as an error dependent on the temperature difference measured. Figure 4.8b shows that when a temperature difference of 1 [K] is measured around 301 [K], the relative error in that measurement will be 0.05 [K]. The maximum relative error introduced by this calibration is therefore $\pm 7\%$ of the measured temperature difference.

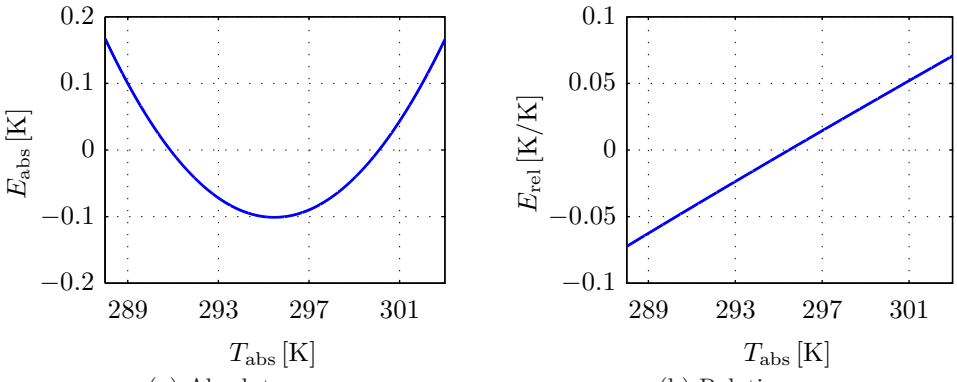

(a) Absolute error

(b) Relative error

Figure 4.8: Estimated absolute and relative temperature error introduced in calibration of thermistors. Showing a maximum absolute temperature error of ± 0.1 [K] and a maximum relative error of 0.07 times the measured temperature difference.

Setup and experiment

As stated in section 4.3.1 a liquid-in-glass thermometer is used as a reference for the temperature calibration of the thermistors. The maximum absolute temperature error of this reference is ±0.1 [K]. When performing the calibration the thermistors must be at the same temperature as the reference. Therefore the reference and thermistors are placed in an aluminium block, referred to as the calibration block. The calibration block contains one hole for the reference and 9 holes for thermistors. The high thermal conductvitity of the calibration block will ensure temperature uniformity of the thermistors and reference. A box of foam around the calibration block furthermore reduces heat exchange with the environment. Reference and thermistors are brought to the different calibration points by heating and cooling the block with a Peltier element. After heating or cooling, the Peltier element is released from the block and the block is placed in the isolating box. At the calibration points the temperature of the reference and the resistances of the thermistors are recorded. With this information the calibration values, constants A,B and C of equation 2.21, are determined. The calibration block, containing the reference and thermistors is shown in figure 4.9. The dimensions of the setup's components are given in table 4.1

Table 4.1: Dimensions of the components of the calibration setup.

Component			Units	Remarks
Block	l x w x h	90 x 60 x 60	[mm]	Aluminium
Thermistors	l x d	1.4 x 0.8	[mm]	Size of sensor without wires
Isolation	t	40	[mm]	Thickness of isolation foam

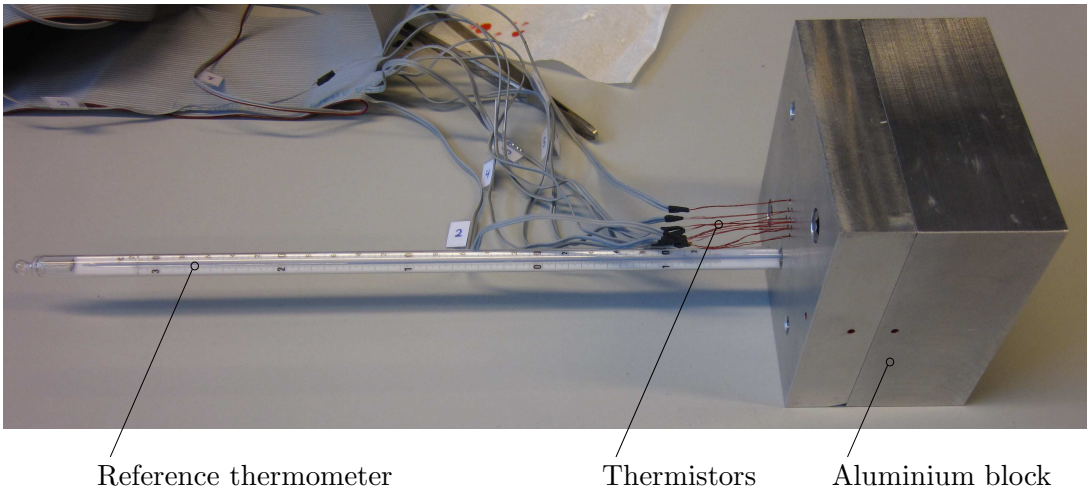

Figure 4.9: Photo showing the main components of the calibration setup.

The resulting calibration procedure is as follows:

Heat/cool Heat or cool the aluminium block with the Peltier element to the desired calibration point.

Settling Remove the Peltier from the block and place the block in the isolation box. Afterwards the setup is left to settle for 15 [min].

Calibration point After the settling time, the reference temperature and electrical resistances of the thermistors are recorded.

Calculation From three calibration points, the calibration values for each thermistor are calculated.

Check The temperature uniformity of the block is checked by repeating the calibration sequence with a shuffled configuration of the thermistors, i.e. the same thermistors are distributed differently amongst the holes in the block.

Additional series For the next series of thermistors, one thermistor of the first series is used as a reference.

Calibration results

A first series of thermistors, thermistors 2 to 10, have been calibrated against the reference thermometer. The thermistor temperatures measured during the middle calibration point are calculated with equation 4.5 and shown in figure 4.10a. During calibration the thermistors are assumed to be at the same temperature within 1 [mK], but figure 4.10a shows differences of about 1 [K]. This shows that the supplier data is not sufficient to describe the thermistor behaviour properly. Figure 4.10b shows thermistor temperatures of the same measurement, but calculated using equation 2.21 and the calibration values. Clearly this result is in better agreement with what is expected, because the temperatures of all thermistors are now approximately the same during calibration. Figure 4.11a shows the thermistor temperatures at the maximum calibration point. Looking at figure 4.11a, it is clear that the temperature of the thermistors, and thus of the calibration block, is decreasing during calibration. This is expected because the ambient temperature is lower, so the block will lose heat to its environment. The heat loss of the block to ambient can cause temperature differences between the thermistors. Figure 4.11b shows the thermistor temperatures minus the temperature of one of the thermistors, in other words the temperature difference with respect to this one thermistor. For the plot of figure 4.11b the temperature data is averaged with a moving average of 150 data points. The original data was obtained at a sampling frequency of 144 [Hz]. Despite the heat loss, the temperature differences are within ± 2 [mK]. Furthermore it can be seen in figure 4.11b that the calibration data is taken from the measurement between 200 and 300 [s], because there the temperature difference goes to zero. The remaining fluctuations are mainly caused by electrical noise of which interference of the mains voltage is the most significant influence.

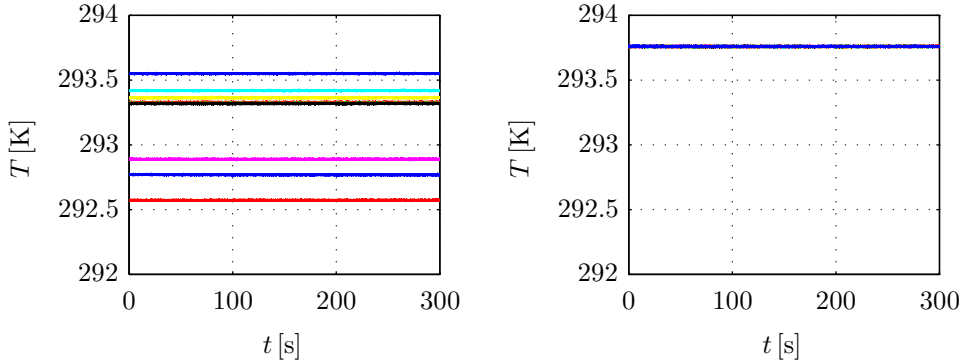

(a) Calculated with supplier data. (b) Calculated with calibration values.

Figure 4.10: Thermistor temperatures during measurement of the middle calibration point (∼295 [K]), calculated with the supplier data and calculated using the calibration values. This shows that the calibration values give a better description of the thermistor temperature.

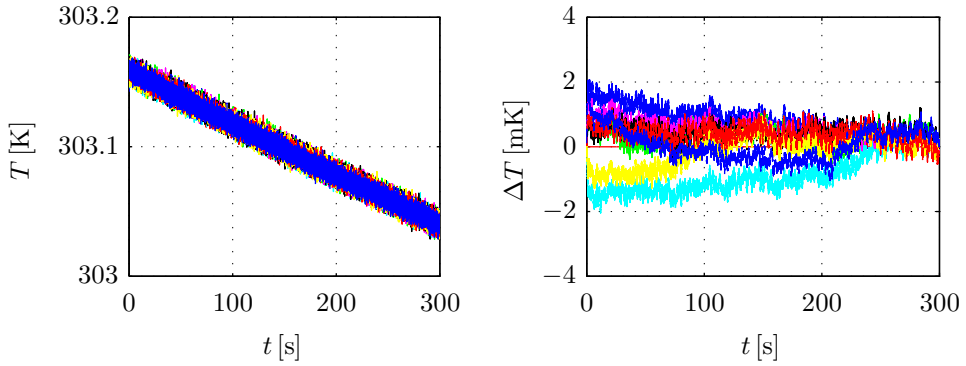

(a) Absolute temperature (b) Temperature difference (averaged 150x)

Figure 4.11: Absolute temperature and temperature difference of the thermistors with respect to thermistor 3, at the maximum calibration point (∼303 [K]).

During the calibration experiments the temperatures of the thermistors and the reference are assumed to be uniform. To check this assumption the calibration experiment is repeated with the same thermistors, but in a different configuration. This means that the placement of the thermistors in the different holes in the block is interchanged. The placement of the thermistors is shown in more detail in appendix C.2.2. The temperature differences of the thermistors with respect to thermistor 3, during the initial calibration and during the calibration with the shuffled configuration are shown in figures 4.12a and 4.12b respectively. Both temperature results have been calculated with the calibration values obtained with the initial calibration. It is clear that the temperature difference during calibration is within ±4 [mK].

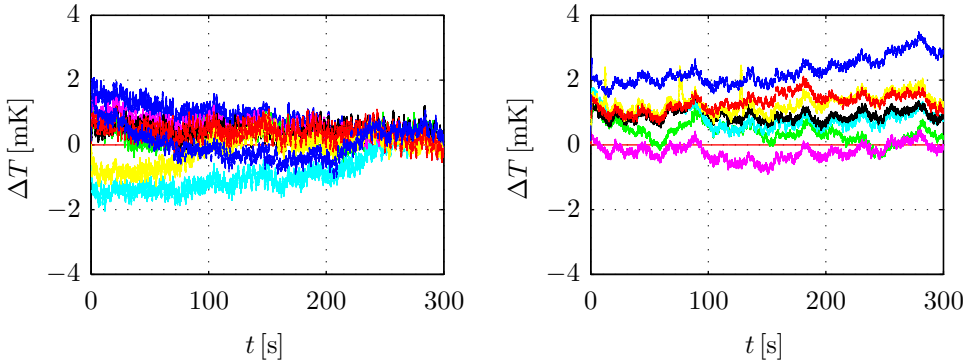

(a) Initial configuration (averaged 150x) (b) Shuffled configuration (averaged 150x)

Figure 4.12: Temperature differences with respect to thermistor 3 at the maximum calibration point, in the initial and in a shuffled configuration. This shuffled configuration shows that the temperature non-uniformity is within ±4 [mK].

Results of the other calibration points for the initial configuration are shown in appendix C.2.1 and the temperature uniformity check at the different calibration points is shown in appendix C.2.2. Additional series of thermistors have been calibrated using a calibrated thermistor of the first series as reference. Results of that calibration are given in appendix C.2.3

Conclusions

In section 4.3.1 it was explained that not absolute temperatures, but temperature differences are of interest for the thermal imager. On that account the calibration procedure has been focussed on the accuracy of measured temperature differences. The error made in a measured temperature difference was further referred to as relative temperature error.

Two factor were identified to influence the relative temperature error of the thermistors.

- A relative temperature error of ±7% of the measured temperature difference, caused by the absolute temperature error of the reference.
- Non-uniform temperature of the thermistors. Checking this uniformity showed that the temperature difference during calibration did not exceed ±4 [mK].

In conclusion it is said that after calibration, the relative temperature error of the thermistors is ±4 [mK] plus ±7% of the measured temperature difference. So for example, when the measured temperature difference between two thermistors is 10 [mK], the maximum relative temperature error is,

Non-uniformity error	±3	=	±4
Reference error	$(10 \pm 4)(\pm 0.07)$	=	±1
Total relative error		=	±5

The actual temperature difference is therefore 10±5 [mK].

4.3.2 Thermistor resolution

Introduction

The temperature resolution of a thermistor determines the smallest temperature difference that can be measured. The goal of this experiment is to determine this temperature resolution. Three factors influencing the temperature resolution are identified:

Thermistor sensitivity The thermistor or detector sensitivity was shown to be determined by the temperature coefficient of resistance (TCR), nominal resistance of the thermistor and the bias current through the thermistor. A higher sensitivity leads to a larger output signal change at a certain temperature change.

Noise Noise also causes signal changes in the output of the thermistor. If a certain temperature change yields an output signal equal to the noise signal, that temperature change cannot be resolved. The noise therefore limits the resolution.

A/D convertor The output signal from the thermistor is conditioned by a Wheatstone bridge and then amplified and fed to an A/D convertor. The A/D convertor translates the analog signal that it receives from the amplifier into a discrete number that is send to the PC. The A/D convertor at hand has a 16 bits resolution, denoting that it can convert the analog input signal into $2^{16} - 1 = 65535$ discrete values. This means that the A/D convertor limits the attainable temperature resolution to 0.23 [mK] at the current temperature input range of 15 [K].

Setup & experiment

In order to measure the temperature resolution of the thermistors a known temperature difference must be established between two thermistors. Because the thermistors will also be used to verify the applied temperature difference some leverage is needed. This leverage is created by attaching two thermistors to the outer sides of an aluminium block with length L, as shown in figure 4.13. The temperature of these outer thermistors is controlled by a Peltier element at each side, such that there is a temperature difference ΔT_L between the outer thermistors. In this way a temperature gradient is created across the length of the block. Two thermistors which are placed in the middle of the block, at a smaller distance l, also experience a temperature difference ΔT_l, which is smaller. In this way the needed leverage is created. The total length of the block L is 90 [mm] and the distance between the inner thermistor l is 4 [mm].

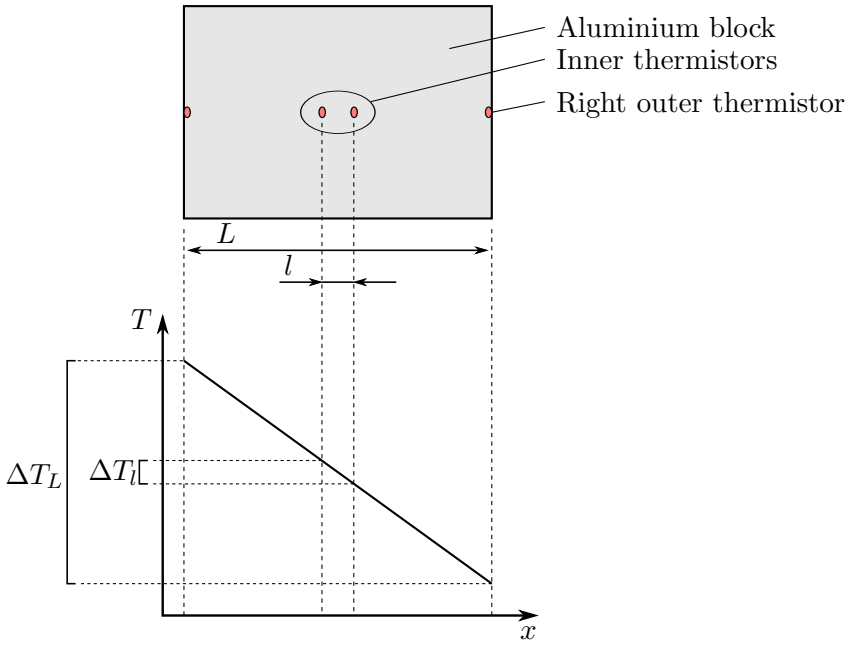

Figure 4.13: Schematic drawing of the resolution setup and an impression of the ideal temperature gradient across the block's length. The aluminium block contains two thermistors at the outside were temperature is controlled and two at the inside between which temperature difference is measured. Ideally the temperature gradient is linear such that measured inner temperature difference ΔT_l can be predicted by the larger outer temperature difference ΔT_L.

The temperature gradient across the block would ideally be linear, such that the temperature difference between the inner thermistors is,

$$\Delta T_l = \Delta T_L \frac{l}{L} = \Delta T_L r \tag{4.6}$$

Here r is a ratio between the outer and inner temperature difference. A linear gradient will however only occur if there is only heat flow along one direction, in this case along the block's length. The Peltier elements don't cover the full sides of the block, therefore the temperatures at the controlled sides will not be uniform. Moreover, since the block is not totally at ambient temperature, there will be some heat exchange with the enviroment. To reduce this heat exchange the setup is isolated with a foam box. Due to these two effects the temperature gradient will not be entirely linear. The ideal, linear, and the non-ideal gradient are shown in figure 4.14. Ideally the inner temperature difference ΔT_l would obey equation 4.6 and the constant of proprtionality r, is then $\frac{l}{L} \approx 0.044$ [K/K]. Due to the multi-directional heat flow however, the temperature gradient will be less steep in the middle of the block, causing a lower ratio. This lower ratio will be determined in the experiment.

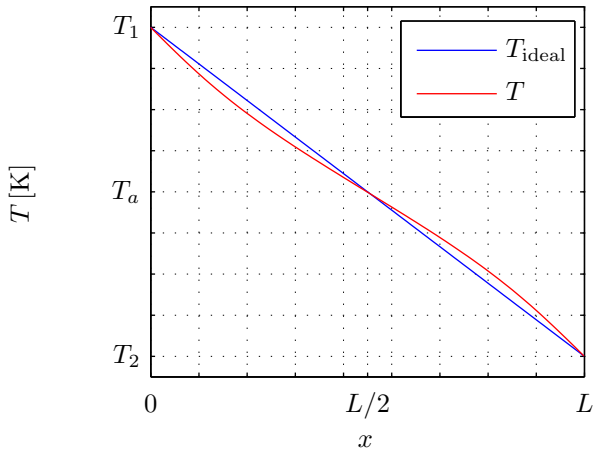

Figure 4.14: Temperature along the length of the resolution block in the ideal case with only heat flow across the length resulting in a linear gradient, and in the non-ideal case with multi-directional heat flow resulting in a non-linear gradient.

Results

The temperature difference across the outside of the calibration block ΔT_L has been varied from +2 to -2 [K]. As an example, in figure 4.15a the measured temperature difference across the block versus time is shown for a setpoint of $\Delta T_L = 1$ [K]. The measurement signal is averaged 128 times on the data acquisition board. In the first 50 [s] the temperature difference oscillates around the setpoint, but after 400 [s] the measured temperature difference is settled to 1±0.004 [K]. The fluctuation on measured ΔT_L is relatively high frequent and symmetric around 1 [K], so it is assumed the fluctuations are caused by electrical noise in the measurement system. A plot of the fluctuations of ΔT_L is shown in figure C.12 of appendix C.2.4. The accompanying temperature difference between the thermistors inside the block, ΔT_l is shown in figure 4.15b. This temperature difference settles to 33±2 [mK], where the fluctuation is also assumed to be due to electrical noise. The fluctuations of ΔT_L are shown in figure C.13.

Measurements as shown in figure 4.15 have been performed for multiple positive and negative outer temperature differences ΔT_L. The measured inner temperature difference ΔT_l is plotted against the corresponding outside temperature difference ΔT_L in figure 4.16a. It appears that ΔT_l is indeed linearly dependent on ΔT_L, as desired. To verify this a ratio r is calculated as,

$$r = \frac{\Delta T_l(\Delta T_L = 0.8) - \Delta T_l(\Delta T_L = -0.8)}{0.8 - (-0.8)} \approx 0.037$$

As expected the ratio r is somewhat lower than the ratio of the outer and inner distance (which is 0.044), due to the multi-directional heat flow, as mentioned in section 4.3.2. The linear curve, or 'fit' that results from mulitplying r with ΔT_L is shown in figure 4.16a. It appears that the ratio fits the data well, but that there is some offset between the measured data and fit. In

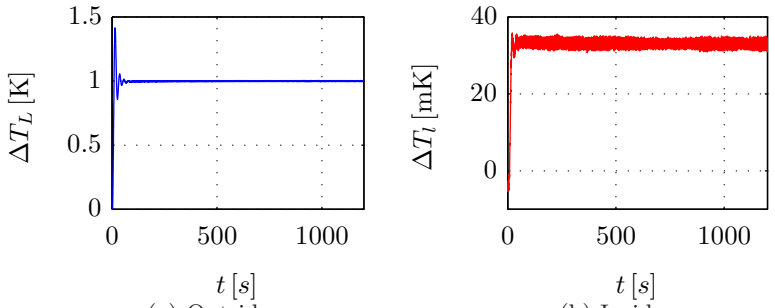

(a) Outside (b) Inside

Figure 4.15: Measured temperature differences between the outer and inner thermistors of the resolution block, in the case of setpoint on the outer temperature difference of 1 [K] (data 128x averaged). This shows that the temperatures settle to a constant value throughout the rest of the measurement.

figure 4.16b the error between fit and measured data shows this constant offset of approximately 3.5 [mK]. Because the offset appears in every measurement it is assumed that it is introduced by calibration. The offset is subtracted from the measured data to come to corrected data, which is shown together with the fitted curve in figure 4.17a. Figure 4.17b shows that the error between the fit and the corrected data is less than ± 1 [mK].

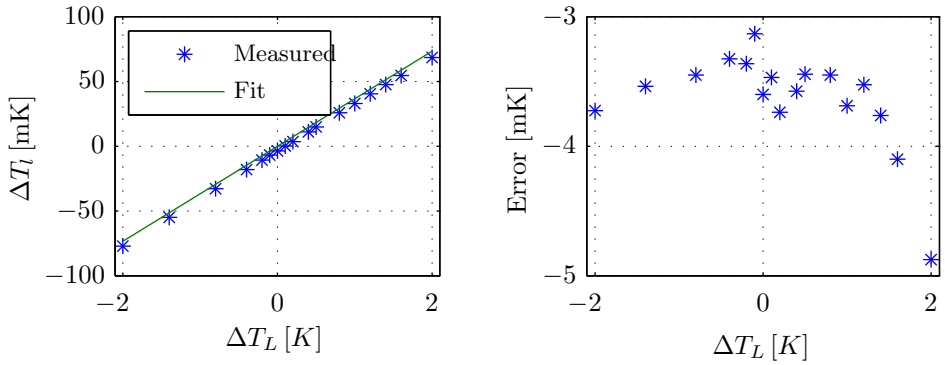

(a) Measurement and fit (b) Error

Figure 4.16: Measured temperature difference inside ΔT_l versus measured temperature difference outside ΔT_L and a fit to the gradient $\frac{\Delta T_l}{\Delta T_L}$. Also showing the error between the measured data and the fit.

With the corrected measurement data, the limit of measurable temperature difference is investigated. At an outside temperature difference ΔT_L of 0.1 [K], the two temperatures measured inside the block, at distance l, are shown in figure 4.18. Due to the noise on the measurement signal the measured temperatures almost overlap. When the signals start to overlap, the difference between them cannot be resolved anymore. According to the ratio the measured inner temperature difference at an outer temperature difference of 0.1 [K] should be,

$$\Delta T_l = r\Delta T_L \approx 0.037 \cdot 0.1 = 3.7\,[\text{mK}]$$

At a temperature difference of 3.7 [mK] the measurement signals are at the limit of overlapping

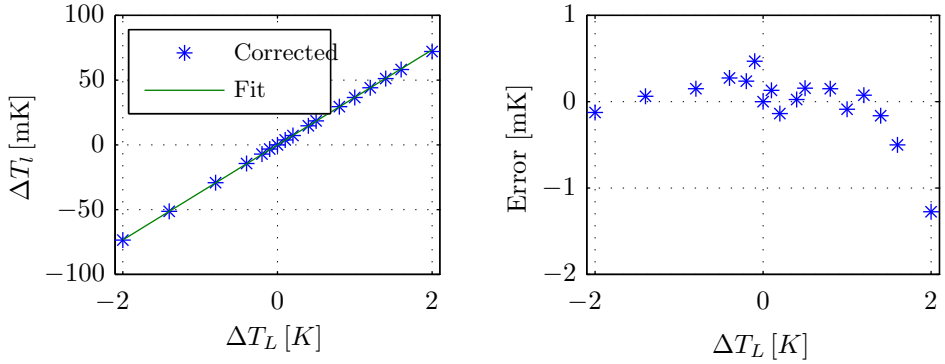

(a) Corrected measurement data and fit

(b) Error

Figure 4.17: Measured temperature difference inside ΔT_l, corrected with an offset value, versus measured temperature difference outside ΔT_L and a fit to the gradient $\frac{\Delta T_l}{\Delta T_L}$. Also showing the error between the corrected data and the fit.

and a smaller temperature difference can thus not be measured accurately.

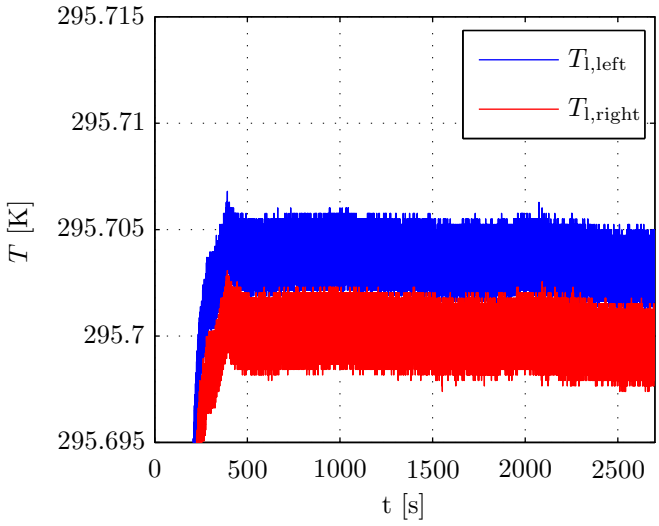

Figure 4.18: Measured temperatures, left and right, at the inside of the resolution block. The actual temperature difference is approximately equal to the peak-to-peak noise of the thermistors, therefore the measured temperature almost overlap.

Conclusions

The temperature difference between two thermistors has been varied by putting them at a small distance l at the inside of an aluminium block. The temperature difference ΔT_l between them has been varied by controlling the temperature at the outer sides of the block which has a length L. With this setup the resolution of the thermistors is determined. From the experiment the following conclusions are drawn:

- By doing measurements with a series of different outside tempeature difference a constant ratio r is found which relates the measured outside temperature difference to the inside temperature difference. This ratio is used to predict the inside temperature difference.
- At an outside temperature difference of $\Delta T_L = 0.1$ [K] the measurment signals of the inner thermistors were at the limit of overlapping, as shown in figure 4.18. According to the ratio r, the actual inside temperature difference ΔT_l was 3.7 [mK] for this ΔT_L. It is therefore concluded that in this case the resolution of the thermistors is approximately 4 [mK]. The measurement signal of the thermistors was averaged 128 times.
- The resolution is limited by noise in the thermistor's output signal. Reducing the noise or doing more averaging on the measurement signal can thus improve the temperature resolution. The A/D convertor limits the attainable temperature resolution to 0.23 [mK].

4.4 Pixel response time

4.4.1 Introduction

The thermal response time determines the speed of response of the pixel to a changing heat input. In the proposed experimental setup, the influence of pixel area size on response time is investigated. Three different pixel sizes will be used, which each differ approximately a factor 10 in area. In order to determine the response time of the different pixels, the response of the pixel temperature to a changing heat input is measured. An office beamer is used to create this changing heat input by exposing the pixel to a step input of light on the pixel. Due to the step input the pixel will heat up and, over time, settle to a steady state temperature. From the pixel's temperature over time, its thermal response time can be obtained. How the response time is found from this experiment can be explained by looking at the pixel's heat balance. The beamer creates a spot of light on the pixel which causes a heat input P_{beam}. Besides the beamer the pixel also exchanges heat with the rest of its environment. The heat exchange with the environment is governed by the total heat transfer coefficient of the pixel G and the temperature difference with the environment $\Delta T = T_{\text{p}} - T_{\text{e}}$, where T_{p} is the pixel temperature and T_{e} is the temperature of the environment. The heat capacity C of the pixel determines how much the pixel temperature increases above the environment temperature for a certain net heat input. This leads to the heat balance of the pixel,

$$C\frac{\mathrm{d}(\Delta T)}{\mathrm{d}t} = P_{\text{beam}} - G(\Delta T) \tag{4.7}$$

From this heat balance the temperature change of the pixel ΔT above the environment, is obtained as,

$$\Delta T(t) = \frac{P_{\text{beam}}}{G}\left\{1 - e^{-t/\tau}\right\} \tag{4.8}$$

The response time τ determines the time is takes for the pixel temperature to settle to a steady state value, and is determined by the pixel's heat capacity C and its total heat transfer coefficient G as,

$$\tau = \frac{C}{G} \tag{4.9}$$

The experiments are performed both in vacuum and air. The total heat transfer coefficient G therefore consists of the heat transfer coefficients for conduction g_{cond}, convection g_{conv} and radiation g_{rad} of the pixel or only of conduction and radiation. In the experiment three pixel sizes are used which differ in area by a factor 10. It is expected that increasing the area causes the heat capacity C and heat transfer coefficients g_{conv} and g_{rad} to increase, while g_{cond} remains constant. Whether this leads to a change in response time depends on the ratio between C and G. The setup and experiment steps used are discussed in section 4.4.2. In section 4.4.3 an estimation of heat capacity, heat transfer coefficient and response time for the different pixel areas is given, and in section 4.4.4 the results of the experiment are shown. Finally the conclusions of the experiment are given in section 4.4.5.

4.4.2 Setup and experiment

A schematic drawing of the experimental setup is shown in figure 4.19 and a photo of the setup is shown in figure 4.4a. Also the components of the setup are discussed in section 4.2.2. Three different pixel sizes of, 3x3, 10x10 and 30x30 [mm], will be used in the experiments.

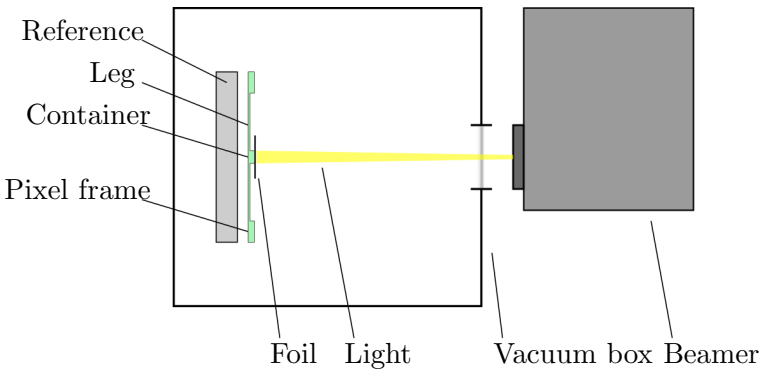

Figure 4.19: Schematic drawing of the experimental setup, showing the reference object, pixel and its support structure, vacuum box and beamer. The beamer creates a step, heat input, by exposing the pixel to a dot of light on the pixel's foil.

The experiment sequence is as follows,

- One of the pixel foils, 3x3, 10x10 or 30x30 [mm] is attached to the container.
- The vacuum box is closed, after which it can be brought to vacuum, depending on whether an air or vacuum measurement is being performed.

- The setup is left to settle for 30 [min] to let al the components come to a uniform temperature.
- The beamer projects a dot of light on the pixel during 120 [s]. The area of the dot is approximately equal to the area of the smallest pixel.
- The beamer projects nothing during 120 [s].
- The beamer sequence of the previous two steps is repeated 6 to 20 times.

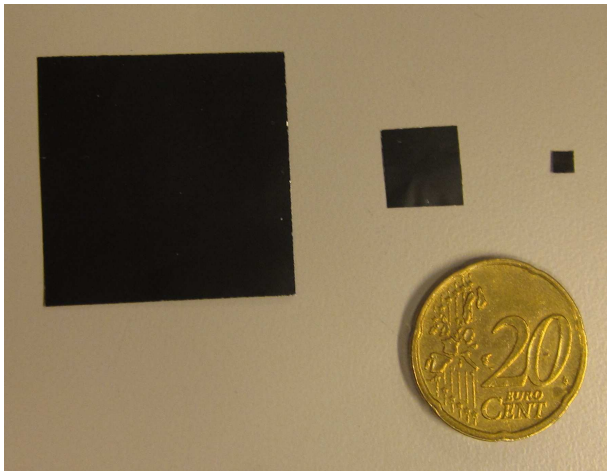

Figure 4.20: Photo showing the three pixel foils used in the experiment of 3x3, 10x10 and 30x30 [mm]. The pixels are pieces of aluminium foil, made black on each side with spray paint.

4.4.3 Estimation

In this section an estimation of the response time for the different pixel sizes in air an vacuum are shown. The response time is determined by the heat capacity C and heat transfer coefficient G of the pixel. The calculation of C and G are given in detail in appendix C.3.1.

Heat capacity

The heat capacity of the pixel is determined by the heat capacities of its components. The pixel consists of a foil, thermistor, container and thermal paste. An estimate of their heat capacities is shown in figure 4.2. Only the heat capacity of the foil is dependent on pixel area. The heat capacity of the total pixel therefore increases with increasing pixel area. The estimated heat capacity of the pixel versus pixel area is shown in figure 4.22a.

Table 4.2: Heat capacities of the different parts of the pixel.

Part	Value [mJ/K]	Remarks
Foil	0.6 . . . 60	Estimate; depends on area
Thermistor	1.3	From thermistor data sheet
Holder	3	Estimate
Thermal paste	2	Estimate
Total	6.9 . . . 66.3	

Heat transfer coefficient

Heat can be transferred from and to the pixel by conduction, convection and radiation. The heat transfer coefficient in air is therefore given by,

$$G_{\text{air}} = g_{\text{cond}} + g_{\text{conv}} + g_{\text{rad}}$$

Due to the absence of a fluid facilitating convection, in vacuum convection is not present and the total heat transfer coefficient is then given by,

$$G_{\text{vac}} = g_{\text{cond}} + g_{\text{rad}}$$

The calculation of the heat transfer coefficient is shown in detail in appendix C.3.1. Here the main aspects of conduction, convection and radiation, and their dependence on pixel area are discussed.

Conduction Conduction takes place between the pixel and its frame, through the thermistor wires and through the support legs. The conduction heat transfer coefficient g_{cond} depends on thermal conductivity k, cross sectional area A_{cond} and length of the material through which the heat flows.

$$g_{cond} = \frac{kA_{\text{cond}}}{L} \tag{4.10}$$

The conduction heat transfer coefficient of the thermistor wires is approximately a factor 60 higher than that of the legs and is thus the most significant. This coefficient is independent of pixel area, since the thermistor wires are the same each time.

Convection Convection requires the transport of heat by a fluid. In the experiment there will only by natural fluid flow driven by buoyancy forces on the air caused by density differences of the air. The convective heat transfer coeffcient is generaly given as an average heat transfer coefficient per unit area $\overline{h}$.

$$g_{conv} = \overline{h}A \tag{4.11}$$

Convection can take place at the front and back surface of the pixel. The convective heat transfer is therefore proportional to two times the pixel area A_{p}.

Radiation The radiation heat transfer coefficient was determined as,

$$g_{\text{rad}} = 4\sigma\varepsilon T_{\text{lin}}^3 A \tag{4.12}$$

Like the g_{conv} the radiation heat transfer coefficient depends linearly on two times the pixel area A_{p}.

In figure 4.21a the conduction, convection and radiation heat transfer coefficients are plotted versus pixel area. Due to the fact that g_{cond} is the only coeffcient to be independent of pixel area, it is most significant for very small pixel areas. As pixel area increases radiation and convection coefficient become larger than the conduction coefficient. The total heat transfer coefficients versus pixel area, in air and vacuum, are plotted in figure 4.21b. Both total coefficients start at the conduction coefficient for very small pixel area and increase with pixel area according to the increase of the convection and radiation coefficients. The total coefficient in air is always larger than in vacuum due to the absence of convection in vacuum. Figure 4.22b shows the estimated response time versus pixel area in vacuum and air. Heat capacity and total heat transfer coefficient both increase linearly with pixel area. The response time therefore tends to a final value for infinite pixel area, which is denoted with asymptotes in figure 4.22b.

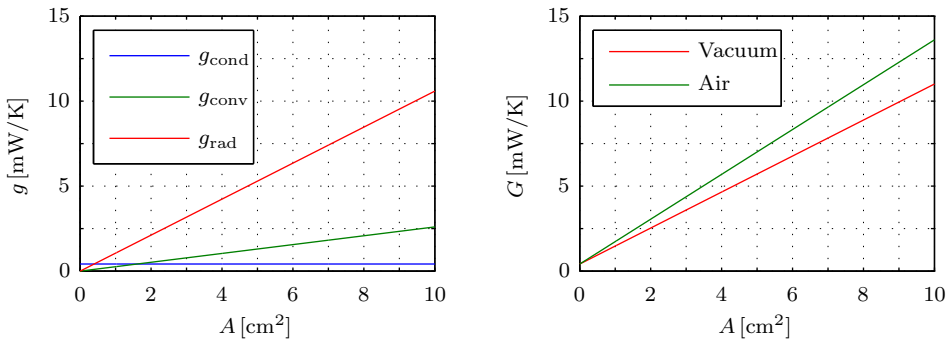

(a) Parts (b) Total

Figure 4.21: Plots showing the heat transfer coefficients versus pixel area for conduction, convection and radiation and the total heat transfer coefficient in air and vacuum. For small pixel area conduction is most significant, but with increasing pixel area, convection and radiation become more dominant.

4.4.4 Results

Measured temperatures of the pixel, reference, frame and environment of one response time experiment are shown in figure 4.23. The exponential course of the pixel temperature, responding to the step input can clearly be seen. The response of the pixel temperature above its environment is of interest. The temperature of the frame is therefore subtracted from the pixel temperature, to obtain the thermal response. Figure 4.24 shows the temperature response to

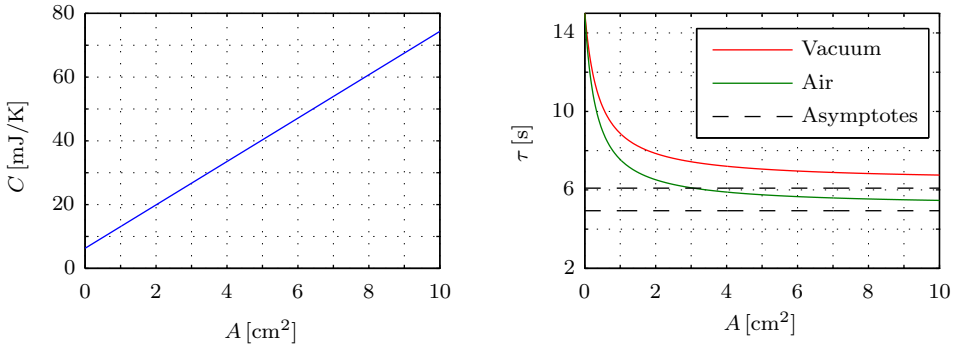

(a) Heat capacity

(b) Response time

Figure 4.22: Plots showing the pixel's heat capacity and the pixel's response time versus pixel area. The response time decreases with increasing pixel area and tends to a final value at infinite pixel area, denoted by the asymptotes.

one step input. The response time is determined from this measurement by determining the time it takes for the pixel temperature to increase 63.2% of the the total temperature increase above the environment. This is denoted by the dashed lines in figure 4.24.

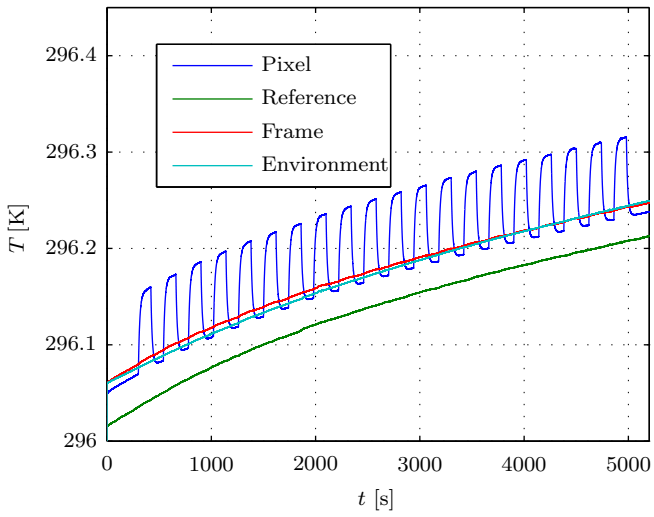

Figure 4.23: Temperatures of pixel, reference, frame and environment during a response time measurement. The temperatures of reference, frame and environment all show the same trend. The pixel temperature responds to the step light input on top of the general temperature trend.

The obtained response times in air and vacuum are shown in figures 4.25a and 4.25b respectively. Both figures show the estimated response time in air in green and the estimated response time in vacuum in red. The measurements for the three different pixel sizes are shown with boxplots in the same figure. The following observations are made from these results:

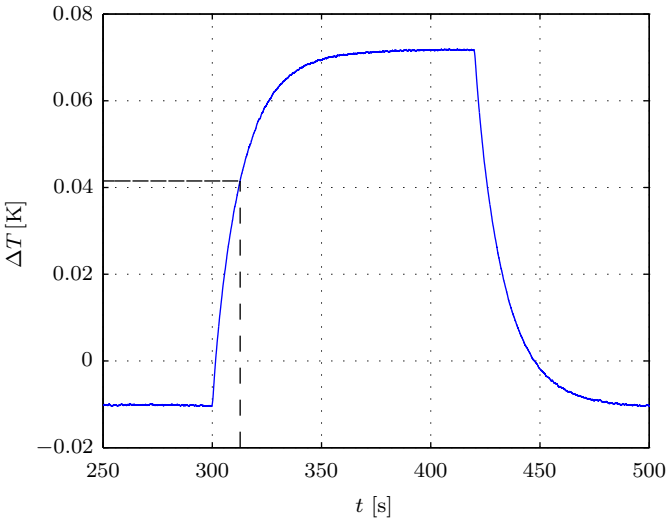

Figure 4.24: Plot of pixel temperature minus frame temperature versus time. The response time is determined by finding the time it takes for the pixel temperature to increase 63.2% of the the total temperature increase.

- The response times which have been measured 20 times for each pixel size are consistent within 0.5 [s], except for a few outliers.
- In air the response time of the smallest and middle sized pixel are within 1 [s] of the estimated response time. The response time of the largest pixel is significantly lower than what was estimated.
- The expected difference in response time between air and vacuum is not seen in the measurements. The response times per pixel size are the same within 0.2 [s] in air and vacuum.

The lack of difference between response time in air and vacuum, indicates that convection doesn't play a significant role in the heat transfer of the pixel. The deviation from the estimated response time at larger pixel areas is assumed to be caused by the size of the light dot projected on the pixel. The area of the dot is approximately that of the area of the smallest pixel. As a consequence the larger pixels receive a heat input on a relatively small part of their area, compared to the smallest pixel. This causes a non-uniform temperature increase of the pixel. The center of the pixel, where the light dot is on the pixel, heats up. The sides of the pixel don't heat up directly, but maintain a temperature close to the temperature of the reference, due to radiation heat exchange with the reference. Heat from the center flows by conduction to the sides of the pixel. This conduction loss to the sides of the pixel causes the temperature of the middle of the pixel to reach a steady state value faster, which causes an apparent lower response time. This indicates that the Biot number, as discussed in section 2.6.6, of the middle and largest pixel is larger than 0.1. The non-uniform temperature of the pixel has been verified

for the largest pixel of 30x30 [mm], by looking at it with an infrared camera. The pixel was exposed to a light spot of approximately 10x10 [mm]. The resulting temperature profile of the pixel is shown in figure 4.26a. Subsequently the pixel was exposed to a light spot covering its full area, which results in the temperature profile of figure 4.26b. Clearly the temperature difference across the pixel is smaller when the pixel is fully exposed to light. At full exposure the temperature difference across the pixel is still not negligable. The thermal response should however be closer to the case in which the pixel temperature is uniform. Figure 4.27a shows again the measured response times for the small light spot, and figure 4.27b shows the response times measured when the pixel is exposed to a light dot approximately equal to its total area. As expected the measured response time of the largest pixel increases significantly and is closer to the estimated response time.

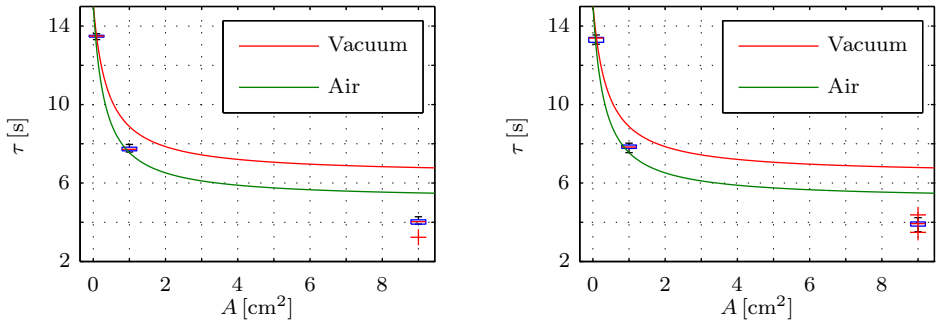

(a) Air (b) Vacuum

Figure 4.25: Estimates and measured data of response time in air and in vacuum.

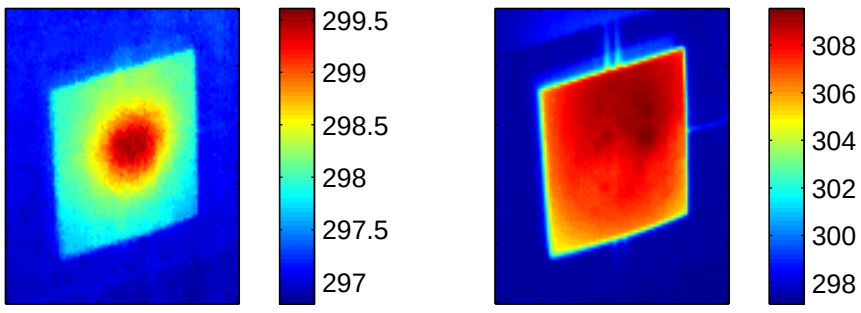

(a) Small spot (b) Spot covering total pixel area

Figure 4.26: Images of the pixel obtained with an infrared camera. Showing a pixel exposed to a small light dot at its center and a pixel exposed with a light dot covering its total area.

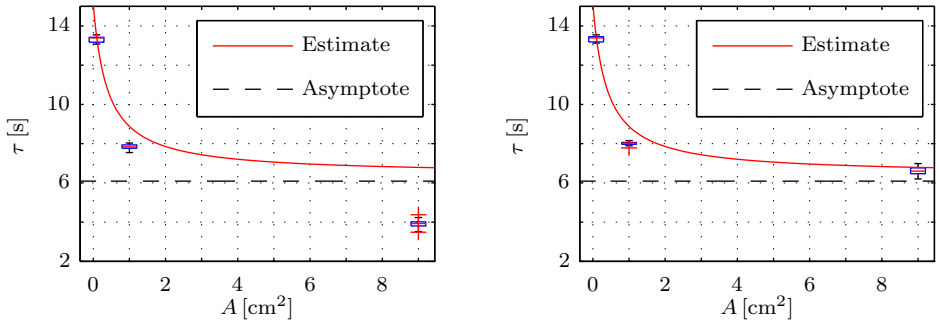

(a) Small spot

(b) Varying spot

Figure 4.27: Estimate and measured response time for a small spot size and for spot sizes adapted to the size of the pixel.

4.4.5 Conclusions

The pixel's thermal response time τ has been measured in an experiment. Response times were obtained by evaluating the temperature response of the pixel to a heat input created by exposing the pixel to a light dot, projected with a beamer. The measurements were carried out in air and in vacuum and for three different pixel area sizes. The following conclusions are drawn from the results of the experiment;

- From the measurements in air and vacuum no significant difference in response time is observed. A difference was expected due to the fact that contrary to in air, in vacuum convective heat transfer is absent. From this lack of difference in response time, it is concluded that convection doesn't play a significant role in the pixel's heat transfer.

- Increasing the size of the pixel results in a lower response time, as expected. The heat capacity C of the pixel increases with pixel area, but since the response time decreases, it is concluded that the total heat transfer coefficient of the pixel G increases stronger than the heat capacity. The support structure of the pixel (pixel frame and frame legs), through which the conductive heat transfer takes place, is the same at each pixel size. The increasing total heat transfer coefficient is therefore attributed to an increasing radiation heat transfer. A pixel with a larger pixel thus leads to a higher radiation heat transfer coefficient g_{rad}, which is significantly larger than the conduction coefficient g_{cond}. This supports the theoretical trend in the heat transfer coefficients which were discussed in section 2.6.2.

- For the larger pixel areas temperature uniformity as mentioned in section 2.6.6 has been encountered. The thickness-width ratio should therefore higher than the ratio of these pixels to obtain a pixel with a good performance.

4.5 Pixel thermal resolution

4.5.1 Introduction

The thermal resolution of a thermal imager was shown to be given by the *NETD* in section 2.6.5. Increasing the size of a pixel showed to improve the thermal resolution due to the increase of the radiation absorbing area and due to the increase of the radiation heat transfer coefficient. The pixel size increase makes the imager more sensitive to the temperature of the target. This is more clear when looking at the heat balance of the pixel given by equation 2.18 and repeated here as,

$$\begin{aligned} \tau \frac{\mathrm{d}T_\mathrm{p}}{\mathrm{d}t} &= r_\mathrm{t}(T_\mathrm{t} - T_\mathrm{p}) + r_\mathrm{r}(T_\mathrm{r} - T_\mathrm{p}) + r_\mathrm{f}(T_\mathrm{f} - T_\mathrm{p}) \\ &= r_\mathrm{t}\Delta T_\mathrm{t} + r_\mathrm{r}\Delta T_\mathrm{r} + r_\mathrm{f}\Delta T_\mathrm{f} \end{aligned} \tag{4.13}$$

where r_t, r_r, r_f were the ratios of the heat transfer coefficients of the target, reference and pixel frame to the pixel's total heat transfer coefficient G. ΔT_t, ΔT_r, ΔT_f are the temperature differences of target, referene and frame with respect to the pixel. The ratios give an indication of the influence of the temperature of each object on the temperature of the pixel. The goal of the experiment at hand is to check the influence of pixel area size on the coefficient ratios.
In section 4.4.4 it was shown that the thermal response time τ could not be determined accurately for all pixel sizes. Therefore it would be preferable if the $\tau \frac{\mathrm{d}T_\mathrm{p}}{\mathrm{d}t}$ term in the heat balance would be negligably small compared to the other terms of the equation, such that it can be neglected. In other words the pixel temperature should be settled and the temperature differences of the objects with respect to the pixel should be large.

4.5.2 Setup and experiment

Experiment

In order to find the influence of pixel area on the thermal resolution of a thermal imager an experiment is performed with one pixel. Three different pixel area sizes will be used in the experiment. Each pixel has an area which is a factor 10 larger than the previous one. The pixel is placed between a reference and a target as shown in figure 4.28. The target is fully exposed to light from a beamer to be able to bring the target to different temperatures as shown in figure 4.4b. At different target temperatures the target, pixel, pixel frame and reference temperature are measured. For each measurement the pixel heat balance of equation 4.13 is formed. The

equations of all measurements form a set of equations given by,

$$\begin{bmatrix} \Delta T_{\mathrm{t}1} & \Delta T_{\mathrm{r}1} & \Delta T_{\mathrm{f}1} \\ \Delta T_{\mathrm{t}2} & \Delta T_{\mathrm{r}2} & \Delta T_{\mathrm{f}2} \\ \vdots & \vdots & \vdots \\ \Delta T_{\mathrm{t}n} & \Delta T_{\mathrm{r}n} & \Delta T_{\mathrm{f}n} \end{bmatrix} \begin{Bmatrix} r_{\mathrm{t}} \\ r_{\mathrm{r}} \\ r_{\mathrm{f}} \end{Bmatrix} = \begin{bmatrix} 0 \\ 0 \\ 0 \end{bmatrix} \tag{4.14}$$

where n is the measurement number. In this equations it is assumed that the pixel temperature variation is very small compared to the temperature differences.

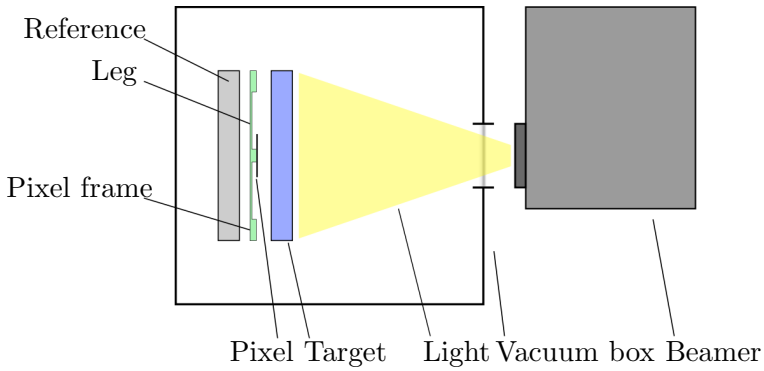

Figure 4.28: Schematic drawing of the setup.

The experiment sequence is as follows:

1. Place one of the three different pixel sizes in the setup and bring the setup to vacuum.
2. Heat the target to the desired temperature and let the setup settle until the temperature change of the pixel is small.
3. Measure temperatures of all objects.
4. Repeat steps 2 and 3 for different target temperatures.

For each pixel size 15 measurements will be performed at target temperatures between 296 and 303 [K]. The first measurement is performed at a target temperature T_{t} of 296 [K] and for each subsequent measurement T_{t} is increased by 0.5 [K].

Expectation

In section 4.4.3 the separate and total heat transfer coefficients of the pixel have been estimated. The total heat transfer coefficient G was divided into a radiation g_{rad} and a conduction heat transfer coefficient g_{cond}. In the case at hand these coefficients consist of,

$$g_{\mathrm{cond}} = g_{\mathrm{f}}$$
$$g_{\mathrm{rad}} = g_{\mathrm{t}} + g_{\mathrm{r}}$$

Table 4.3: Estimated heat transfer coefficient ratios.

A_p	3x3 [mm]	10x10 [mm]	30x30 [mm]
r_t	0.095	0.355	0.48
r_r	0.095	0.355	0.48
r_f	0.81	0.28	0.04

It is assumed that the pixel receives radiation at its front side from the target only and at its back side from the reference only. Consequently the heat transfer coefficients of target and reference each make up half of the total radiation heat transfer coefficient. Considering this, the expected heat transfer coefficient ratios are calculated and shown in table 4.3. As shown in figure 4.21a, for the smallest pixel size conduction heat transfer, which occurs between pixel and frame, is dominant. This causes r_f to be significantly larger than the radiation coefficient ratios r_t and r_r. As the pixel size increases the radiation becomes more significant, such that r_t and r_r become larger with respect to r_f.

4.5.3 Results

As an example of the course of each measurement, the results of one measurement with the smallest pixel are given. The temperatures and temperature differences of all objects are shown in figure 4.29. The sample frequency of the temperature data acquisition is 63 [Hz]. In post-processing the data, a moving average with a window size of 60 samples is applied. From this measurement the temperatures at 600 [s] are used for further analysis. At that point the pixel temperature variation $\frac{dT_p}{dt}$ is about $1{\cdot}10^{-4}$ [K/s]. The temperature differences (ΔT_t, ΔT_r, ΔT_f) are in the order of 0.1 [K]. Noting that the pixel thermal response time τ is in the order of 10 [s] and the coefficient ratios r of order 0.1, the order of magntiude of the $\tau\frac{dT_p}{dt}$ term is a factor 10 smaller than the other terms in equation 4.13 and is therefore assumed zero. The ratio of the temperature differences give an indication of the coefficient ratios. The ratio of target ΔT_t and frame ΔT_f temperature difference versus reference tempeature difference ΔT_r throughout the measurement are shown in figure 4.30. These ratios $\Delta T_t/\Delta T_t$ and $\Delta T_f/\Delta T_t$ change only 1 and 7 % with respect to their end value, respectively. Comparable measurements have been performed at a range of target temperatures for all three pixel sizes. For the smallest pixel the results of this series of measurements is shown in figures 4.31 and 4.32. The results of the middle and largest pixel are given in appendix C.3.2.

In figure 4.31a it is seen that for each measurement the target temperature is higher than the reference temperature. The pixel and frame temperature are in between target and reference temperature and their temperatures are very close to each other. The temperature difference between frame and pixel ΔT_f is very small compared to ΔT_t and ΔT_r, as can be seen in figure 4.31b. Looking at the ratios of the temperature differences in figure 4.32, ΔT_t shows to be about

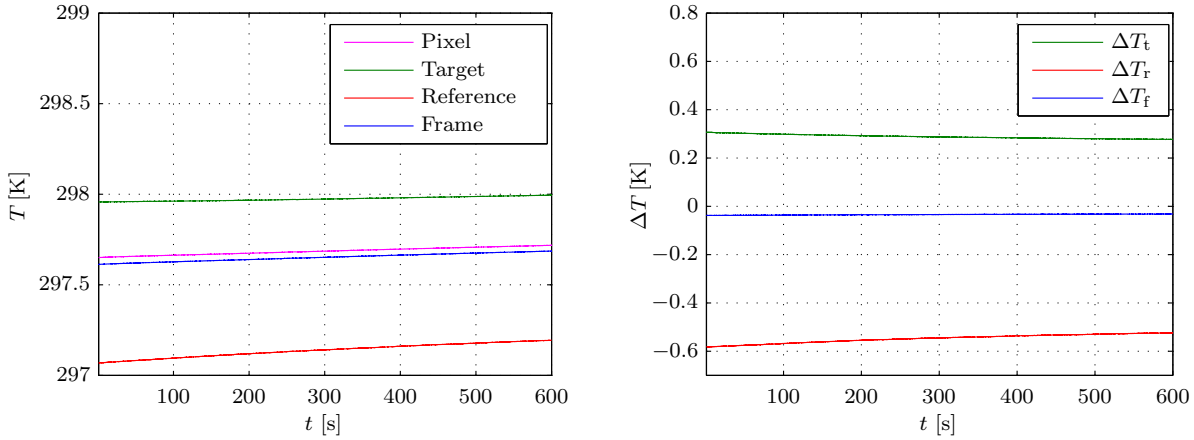

(a) Temperatures

(b) Temperature differences

Figure 4.29: Temperatures of target, pixel, pixel frame and reference during a measurement with the smallest pixel. Also showing temperature differences with respect to the pixel temperature during the measurement.

half of ΔT_r. This indicates that the heat transfer coefficient of the target, g_t is twice as large as g_r. The small ΔT_f could be due to the fact that conduction is dominant for small pixel sizes, but could also be caused by the fact that the frame exchanges heat by radiation approximatly the same as the pixel. Temperature difference ratios for the middle and largest pixel size are shown in figure 4.33. The results show that for the smallest and largest pixel size the ratios are about the same, ΔT_t is approximately half of ΔT_r and ΔT_f is less than ¹⁄₁₀ of ΔT_r. For the middle pixel size however, ΔT_t is only ⅓ of ΔT_r and ΔT_f is larger at about ⅙ of ΔT_r. In other words, for the middle pixel, the pixel temperature is closer to the target temperature and the temperature difference between pixel and frame is larger.

With the measurement results equation 4.14 is solved for the heat transfer coefficient ratios. This results in the coefficient ratios listed in table 4.4. With these coefficient ratios and measured temperatures of reference, pixel and frame it should be possible to predict the target temperature as,

$$T_\mathrm{t} = T_\mathrm{p} + \frac{r_\mathrm{r}}{r_\mathrm{t}}(T_\mathrm{p} - T_\mathrm{r}) + \frac{r_\mathrm{f}}{r_\mathrm{t}}(T_\mathrm{p} - T_\mathrm{f}) \tag{4.15}$$

The difference between the measured and predicted target temperature, the temperature error T_err, is plotted in figure 4.34a. The root mean square error of the prediction is given for each pixel size in table 4.4. The expected trend in coefficient ratios given in table 4.3 doesn't appear in the calculated ratios. The ratios of the middle pixel deviate from the prediction and from the ratios found for the other two pixels. Furthermore the radiation coefficients r_t and r_r seem to decrease, while r_f increases with increasing pixel size. This is opposite to what was expected. The deviation from the expected coefficient ratios is probably caused by the fact that the frame is influenced by target and frame temperature in the same way as the pixel is. As a consequence the influence of frame temperature on the pixel's heat balance cannot be resolved accurately.

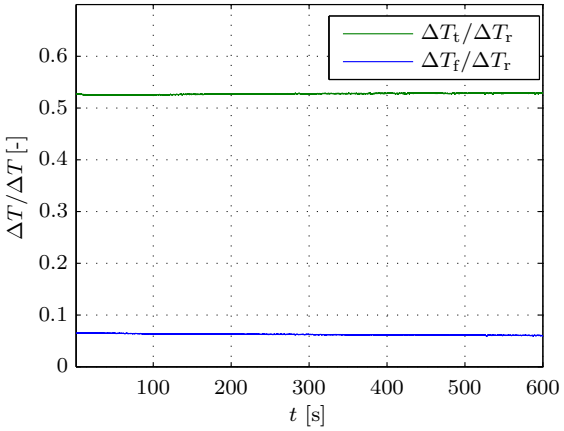

Figure 4.30: Ratio of temperature differences, showing that these ratios are constant during a measurement.

Table 4.4: Coefficient ratios for all three pixel sizes, calculated using target, reference, pixel and frame temperatures. Also showing the rms temperature error on the predicted target temperature calculated with these coefficient ratios.

A_p		3x3 [mm]	10x10 [mm]	30x30 [mm]
r_t	[-]	0.470	0.354	0.458
r_r	[-]	0.234	0	0.180
r_f	[-]	0.295	0.646	0.362
$T_{err,rms}$	[mK]	7.2	9.9	3.8

Because the frame temperature is in most cases very close to the pixel temperature it is proposed to neglect the influence of the frame in this case. The contribution of frame temperature is then removed from the pixel's heat balance and to obtain the coefficient ratios an new system of equations 4.16 is solved.

$$\begin{bmatrix} \Delta T_{t1} & \Delta T_{r1} \\ \Delta T_{t2} & \Delta T_{r2} \\ \vdots & \vdots \\ \Delta T_{tn} & \Delta T_{rn} \end{bmatrix} \begin{Bmatrix} r_t \\ r_r \end{Bmatrix} = \begin{bmatrix} 0 \\ 0 \\ 0 \end{bmatrix} \tag{4.16}$$

In table 4.5 the coefficient ratios, resulting by solving equation 4.16, are listed. The target temperature is now predicted by,

$$T_t = T_p + \frac{r_r}{r_t}(T_p - T_r) \tag{4.17}$$

The resulting temperature error between predicted and measured target temperature is shown in figure 4.34b and the root mean square error is given in table 4.5. Clearly the prediction of target temperature has improved by neglecting the frame temperature. The rms temperature error improved by 1 to 4 [mK]. The target coefficient r_t is about two times larger than the

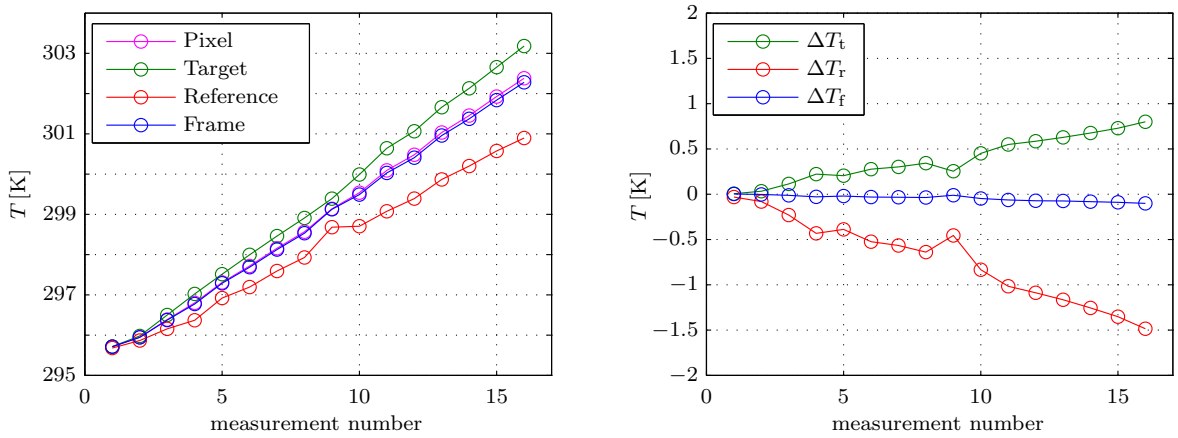

(a) Temperatures

(b) Temperature differences

Figure 4.31: Temperatures and temperature differences during measurements with the smallest pixel at different target temperature.

Table 4.5: Coefficient ratios for all three pixel sizes, calculated using only target, reference and pixel temperatures. Also showing the rms temperature error on the predicted target temperature calculated with these coefficient ratios.

A_p		3x3 [mm]	10x10 [mm]	30x30 [mm]
r_t	[-]	0.650	0.773	0.696
r_r	[-]	0.350	0.226	0.304
$T_{err,rms}$	[mK]	6.0	5.7	2.9

reference coefficient r_r, which indicates that radiation exchange between target and pixel is better than between reference and pixel. The coefficients for the middle pixel deviate from these values, r_t is 3.5 times larger than r_r.

4.5.4 Conclusions

Increasing pixel size should improve the thermal resolution of a thermal imager, because it increases sensitivity to heat radiation from a target object. The goal of the thermal resolution experiment was to verify this relationship. A single pixel, supported by slender legs to a frame, was placed between a target and a reference object. The target object has been brought tho different temperatures by heating it with light from a beamer. Measurements of the object temperatures were obtained when these temeparatures were approximately settled to a steady state value. These measurements were repeated for three different pixel sizes. From these measurements the heat transfer coefficients of target g_t, reference g_r and frame g_f to the pixel were determined, as a ratio with respect to the total heat transfer coefficient G of the pixel. These ratios should indicate how the heat transfer coefficients change with pixel size, and thus

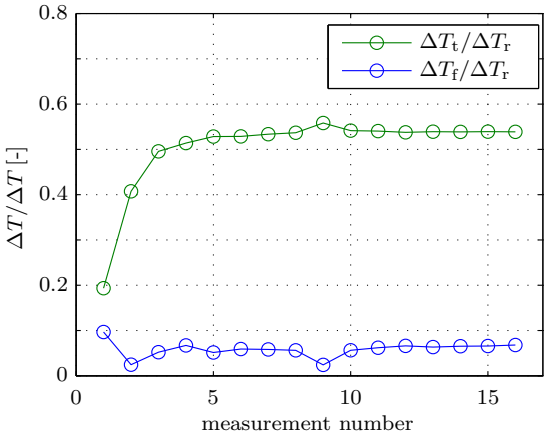

Figure 4.32: Ratio of temperature differences during measurements with the smallest pixel at different target temperatures, showing that the ratios are approximately equal for most measurements.

how the sensitivity of the pixel temperature to temperatures of target, reference and pixel change. Furthermore a predicition can be made of the target temperature using the coefficient ratios and measured temperatures of reference, pixel and frame. The following conclusions are drawn from the experiment:

- The coefficient ratios obtained from this experiment using equation 4.14 don't provide the required insight in thechange of the heat transfer coefficients of the objects versus pixel area size. This is caused by the fact that the frame temperature is subject to approximately the same heat inputs as the pixel. As a consequence the influence of frame temperature on the pixel's heat balance is not independent.
- A prediction of the target temperature is made which yields an rms temperature error $T_{\text{err,rms}}$ of maximum 6 [mK] for all pixel sizes, over a temperature range between 296 and 303 [K]. This prediction is calculated with temperatures of reference and pixel and coefficient ratios of target and reference. In this prediction the influence of frame temperature has been neglected. When frame temperature is included the prediction becomes worse.

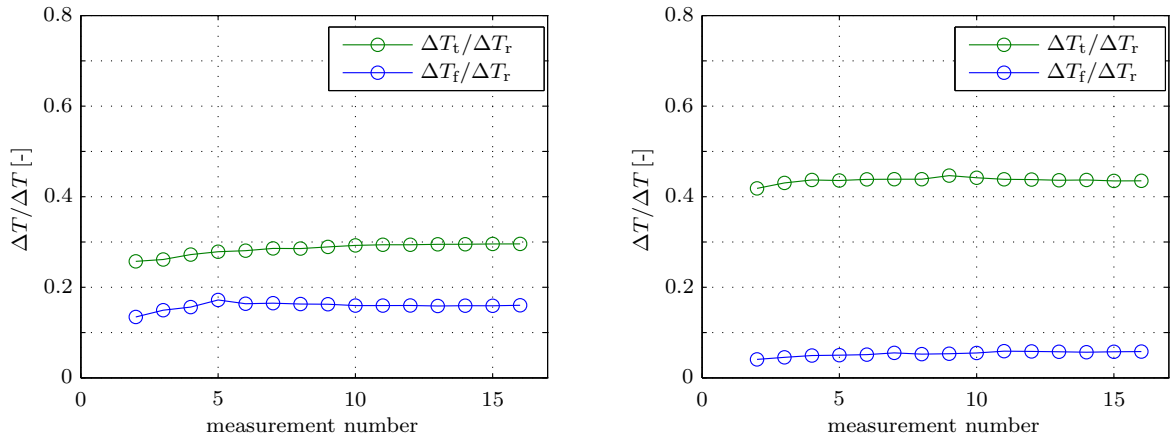

(a) Middle pixel

(b) Largest pixel

Figure 4.33: Ratio of temperatures differences ratios during measurements at different target temperatures for the middle and largest pixel. Per pixel the ratios are approximately equal throughout the different measurements.

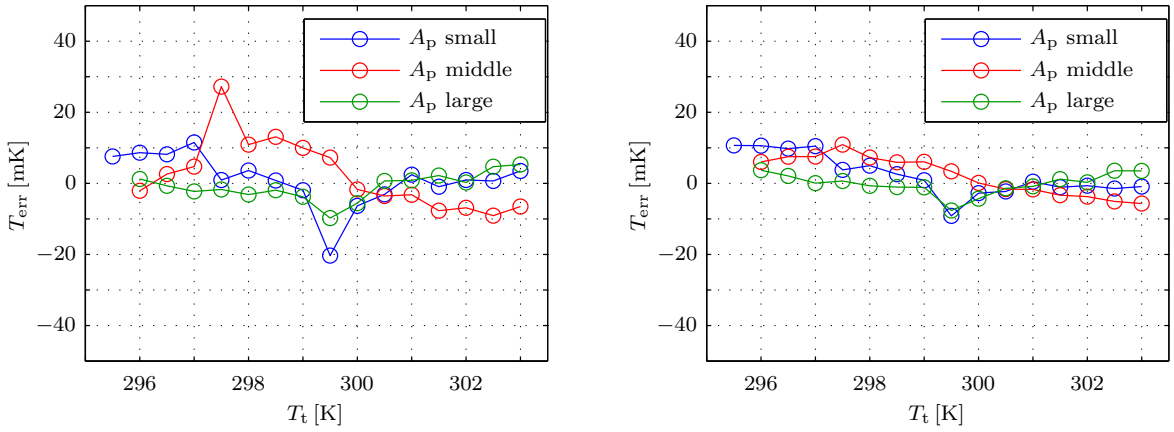

(a) Using T_f

(b) Neglecting T_f

Figure 4.34: Error between predicted and measured target temperature for all three pixel sizes, for a prediction using frame temperature T_f and a prediction where T_f was neglected.

CHAPTER 5

Conclusions and recommendations

5.1 Conclusions

A concept for a thermal imager is introduced to contactlessly measure the surface temperature distribution of the back side of a mirror in vacuum. This thermal imager consists of a reference object and an array of pixels sensitive to thermal radiation from the mirror (the target object). The thermal imager has been modeled whereby its theoretical performance is evaluated. The main challenge for the thermal imager is to reach a thermal resolution of 1 [mK]. In realizing this criterium, the area of the pixels has been shown to be the main design variable. An experimental setup with a single pixel has been build in order to demonstrate the working principle of the concept. Furthermore the influence of varying pixel area on the performance of the pixel is validated in experiments. Based on the modeling and experimental work the following conclusions can be drawn:

1. The thermal imager concept is simple in comparison to conventional thermal imagers shown in section 2.3.1 and theoretically provides better thermal resolution. Increasing pixel area up to about 1x1 [mm] significantly improves thermal resolution due to the increase of the pixel's radiation heat exchange. Beyond a pixel area of 3.5x3.5 [mm] the thermal resolution becomes worse due to decrease of the view factor from the pixel to the target area of interest with increasing pixel area. An optimum in thermal resolution of 0.06 [mK] therefore occurs at a pixel area of 3.5x3.5 [mm] as shown in section 2.6.5.

2. Section 2.6.6 showed that when the pixel area becomes large compared to its thickness it can no longer be assumed uniform in temperature. In section 2.5.3 it was discussed

that the measured pixel temperature may not be the average pixel temperature due to non-uniform current flow through the pixel. A uniform pixel temperature is therefore required. Because pixel thickness is mainly limited by the required pixel response time, the requirement on pixel temperature uniformity limits the possible pixel width to about 1.3x1.3 [mm].

3. From the performance indicators presented in section 2.6 a design path is extracted which guides the design of an optimally performing pixel for a thermal imager. Following the design path shown in section 3.1, a pixel design has been realized which meets all the requirements of section 1.2. The realized design of section 3.2 has a pixel width of 1 [mm], pixel thickness of 9 [μm] and a distance of 0.5 [mm] with respect to the target, resulting in a thermal imager with a spatial resolution of 5 [mm], response time of 1 [s] and thermal resolution of 0.09 [mK].

4. Increasing pixel area causes an increase in pixel heat capacity as well as pixel heat transfer coefficient, and their ratio determines the thermal response time of a pixel. Experiments dicussed in section 4.4 show that the response time decreases from 13.5 to 6.5 [s] with increasing pixel area over the area range of $9{\cdot}10^{-6}$ to $9{\cdot}10^{-4}$ [m^2]. These measurements results are in agreement with the estimated response times. From the response time estimation it is expected that further increase of the pixel area will not yield much change in response time because for large pixel area heat capacity and heat transfer coefficient both scale with pixel area and the response time tends to a constant value. The decrease of response time with increasing pixel area indicates that increasing pixel area cause the radiation heat transfer coefficient to increase. This trend is desirable for obtaining a thermal imager with a small thermal resolution.

5. In the experimental setup a single pixel can measure the temperature at the center of a target with an rms error 2.9 [mK] at best as shown in section 4.5. For pixel areas of 3x3, 10x10 and 30x30 [mm] the rms error on measured target temperature was 6.0, 5.7 and 2.9 [mK] respectively.

5.2 Recommendations

The following recommendations for future work are proposed:

1. In the pixel thermal resolution experiment of section 4.5 the ratio of the pixel's heat transfer coefficients, the coefficient ratios, could not be resolved. The increase of the radiation heat transfer coefficient with respect to the conduction heat transfer coefficient is important in quantifying the advantage of the proposed concept. It is therefore desirable to validate the effect of the pixel area on the coefficient ratios. In order to measure these effects in an experiment two major adaptations should be made to the experimental setup:

- It should be possible to control the temperature of the objects influencing the pixel temperature independently, such that their heat transfer coefficients with respect to the pixel, can be resolved.
- Temperature of the pixel should be measured across its total area, such that the measured pixel temperature is the average temperature of its total area.

2. Creating a thermal image requires multiple pixels in a grid. The field of view of one pixel is larger than the target area of interest which is directly opposite to the pixel. Thermal radiation from the rest of the target object, other than the area of interest, is therefore also incident on the pixel. This effect causes 'crosstalk' which deteriorates the spatial resolution of the thermal imager. The 'crosstalk' and its effect on measured target temperature distribution should be investigated to obtain a better indication of the attainable thermal resolution versus spatial resolution.
3. The proposed design for a thermal imager contains pixels with a large area compared to their to the pixel thickness and size of the support structure. This poses a challenge for the manufacturability and strength of the pixel and support structure. Knowledge of the limit to which the pixel area versus leg slenderness ratio can be increased would give more insight into the maximum attainable performance of the concept.

Bibliography

[1] A.F. Mills. *Basic heat and mass transfer*. Prentice Hall, Inc, second edition edition, 1999.

[2] John G. Webster. *The measurement, instrumentation and sensors handbook CRCnetBase 1999*. CRC Press LLC, 1999.

[3] A. Rogalski. Infrared detectors: status and trends. *Progress in Quantum Electronics*, 27(2):59–210, 2003.

[4] Paul W. Kruse. Can the 300 k radiating background noise limit be attained by uncooled thermal imagers? 2004.

[5] F. Niklaus, C. Vieider, and H. Jakobsen. Mems-based uncooled infrared bolometer arrays: a review. In *Proceedings of SPIE*, volume 6836, page 68360D, 2007.

[6] Paul W. Kruse and David D. Skatrud. *Uncooled Infrared Imaging Arrays and Systems*. Academic Press Limited, first edition edition, 1997.

[7] J.S. Steinhart and S.R. Hart. Calibration curves for thermistors. In *Deep Sea Research and Oceanographic Abstracts*, volume 15, pages 497–503. Elsevier, 1968.

[8] BW Mangum. Triple point of succinonitrile and its use in the calibration of thermistor thermometers. *Review of scientific instruments*, 54(12):1687–1692, 1983.

[9] R. Munnig Schmidt, G. Schitter, and J. van Eijk. *The design of high performance mechatronics*. IOS Press, Delft University Press, 2011.

[10] IEC BIPM, I. IFCC, I. IUPAC, and O. ISO. International vocabulary of metrology–basic and general concepts and associated terms (vim), 3rd edn, jcgm 200: 2008, 2008.

[11] G.R. Lemaitre. *Astronomical optics and elasticity theory: active optics methods*. Springer Verlag, 2009.

[12] J.C. Wyant and K. Creath. Basic wavefront aberration theory for optical metrology. *Applied Optics and Optical Engineering*, 11(s 29), 1992.

[13] W.R. McCluney. *Introduction to radiometery and photometry.* Artech House, Inc., first edition edition, 1994.

APPENDIX A

Theory and modeling

A.1 Thermal resolution requirement

The requirement of milliKelvin thermal resolution stems from the allowable optical aberration of the mirror. Ideally the mirror is perfectly flat and the wavefront of the light passing the mirror is undistorted. Amongst others, thermal deformation causes optical aberrations resulting in a distorted wavefront. To see whether an optical element is corrected well for aberrations the intensity at the image plane is checked. The light which has passed the optical element has got a certain ideal theoretical intensity distribution I_{th} at the image plane. In reality however the optical element will contain some aberration, causing an aberrated intensity distrubution I_{aber}. Strehl suggested that an appropriate tolerance level for drop in intensity of the central peak would be such as,

$$S \equiv \frac{I_{\text{aber}}}{I_{\text{th}}} \geq 0.8 \tag{A.1}$$

In equation A.1 S is the Strehl intensity ratio, which is a generally accepted tolerance. Therefore a system is considered to be well corrected and so called diffraction-limited when the Strehl ratio is equal to or larger than 0.8. A Strehl ratio of $S \geq 0.8$ is equivalent to an rms wavefront error of,

$$\Delta W_{\text{rms}} \leq \frac{\lambda}{14}$$

where ΔW_{rms} is the root mean square wavefront error and λ the light wavelength. This limit on the acceptable wavefront error is called the Marchal criterion [11, 12]. With EUV light the wavelength is $\lambda = 13.5$ [nm], which results in an allowable rms wavefront error smaller or equal than 0.96 [nm]. To keep the wavefront error within this limit the mirror deformations

(Δz) should stay within half of the wavefront error, so $\Delta z_{max} = 0.48$ [nm]. A temperature difference in the mirror of approximately 5 [mK] will cause a thermal deformation equal to Δz_{max}. Therefore the temperature sensor monitoring the mirror should be able to detect milliKelvin temperature differences.

A.2 Performance calculation

A.2.1 Dimensions and material properties

This appendix shows the dimensions and material properties used in the calculation of the pixel performance in sections 2.6 and 3.2.

Some dimensions of the pixel are defined in figure A.1 and their values are given in table A.1.

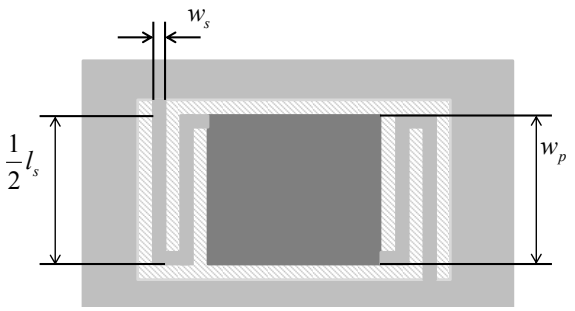

Figure A.1: Dimensions of a pixel

Table A.1: Pixel dimensions

Dimension			Units
Pixel width	w_p	varied	[mm]
Pixel length	l_p	w_p	[mm]
Pixel thickness	t_p	varied	[μm]
Leg length	l_s	w_p	[mm]
Leg width	w_s	$0.01w_p$	[μm]
Leg thickness	t_s	$0.01w_p$	[μm]
Distance target-pixel	$d_\mathrm{t\text{-}p}$	0.5	[mm]
Target width of interest	$w_\mathrm{t,i}$	5	[mm]

The pixel consists of amorphous silicon and the support structure is made of silicon nitride. The necessary material properties of these materials are given in table A.2. Electrical properties of

Table A.2: Material properties

Material	Property		Units
Silicon nitride (Si_3N_4)	Thermal conductivity k	30	[$Wm^{-1}K^{-1}$]
Amorphous silicon (a−Si)	Absorptivity η	0.8	[-]
	Density ρ	2200	[kg/m^3]
	Specific heat c_p	770	[$Jkg^{-1}K^{-1}$]
	Temp.coeff.of resistance α	-0.03	[K^{-1}]

Table A.3: Miscellanious properties

Part	Property		Units	Reference
Detector	Temperature T	300	[K]	-
	Bandwidth start f_1	$1 \cdot 10^{-4}$	[Hz]	[6]
	Bandwidth end f_2	1	[Hz]	[6]
	Nominal resistance R	10	[kΩ]	
Load resistor	Resistance R_L	10	[kΩ]	
Electrical	Bias voltage V_b	2.5	[V]	
	Bias current I_b	0.125	[mA]	
Constants	1/f noise parameter k_f	$1 \cdot 10^{-13}$	[−]	

the detectors as well as constants used in the calculation of the noise voltages are given in table A.3.

A.2.2 Noise sources

Thermal noise is caused by heat exchange of the detector with its environment. The resulting temperature fluctuation of the detector causes a fluctuating resistance of the detector which manifests itself as a fluctuation in the detector's voltage output.

$$\Delta\bar{V}_{th}^2 = \left\{ V_b \frac{RR_L\alpha}{(R+R_L)^2} \right\}^2 \left\{ \frac{1}{1+\beta\frac{RR_L}{R+R_L}} \right\} \left\{ \frac{kT^2}{C} \right\} \tag{A.2}$$

where $\Delta\bar{V}_{th}^2$ is the mean square value of the fluctuating noise voltage, V_b is the bias voltage, R the resistance of the detector, R_L a load resistor, α the temperature coefficient of resistance of the detector, β the electrothermal parameter, k the Boltzmann constant, T detector temperature and C detector heat capacity.

Johnson noise is associated with a fluctuating voltage across the terminals of a resistance due to thermal agitation of charge carriers. Johnson noise is given by the following equation:

$$\Delta\bar{V}_j^2 = 4kT\frac{RR_L}{R+R_L}(f_2 - f_1) \tag{A.3}$$

where f_1 and f_2 are the lower and upper noise bandwidth limit.

1/f-noise is associated with the fluctuation of electrical resistance that varies with 1/f. 1/f-noise voltage can be described by the following equation:

$$\Delta\bar{V}_{1/f}^2 = V_b^2 k_f \ln\left(\frac{f_2}{f_1}\right)\left\{\frac{RR_L}{(R+R_L)^2}\right\}^2 \tag{A.4}$$

where k_f is called the 1/f-noise parameter and $k_f = 1\cdot10^{-13}$ typically for a VO_x microbolometer with $\alpha = -0.03\,K^{-1}$ [6].

Parameters used in the calculation of the noise sources are listed in section A.2.1. The calculated noise contributions are listed int table A.4.

Table A.4: Calculated contribution of the different noise sources.

Noise source	Symbol	Value [μV]
Thermal noise	V_{th}	0.0007
Johnson noise	V_{j}	0.009
1/f noise	$V_{1/\text{f}}$	1.02
Total noise	V_{n}	1.03

APPENDIX B

View factors

B.1 Introduction

Ideally all radiation leaving a target object reaches the sensor object. From figure 2.5 it is obvious however that this is not entirely true. There is some distance between the target and sensor surface, causing the target to also see the gaps between target and sensor. These gaps will be further called the environment. The fraction of total radiation flux emitted by surface 1, that is incident on surface 2, can be defined as the view factor from surface 1 to surface 2 (F_{1-2}). This view factor is purely determined by geometry and given by equation B.1. It is a number between 0 and 1, where $F_{1-2} = 1$ means that surface 1 'sees' only surface 2 and nothing else, and $F_{1-2} = 0$ means surface 1 doesn't 'see' surface 2 at all.

$$F_{1-2} = \frac{\Phi_{1-2}}{\Phi_1} = \frac{1}{A_1} \int_{A_1} \int_{A_2} \frac{\cos\theta_1 \, \cos\theta_2}{\pi R^2} \mathrm{d}a_1 \mathrm{d}a_2 \tag{B.1}$$

where

Φ_1	:	Total radiant flux emitted by area 1, the source
Φ_{1-2}	:	Radiant flux emitted by area 1, that is incident on area 2, the receiver
A_1	:	Total area of the source
A_2	:	Total area of the receiver
$\mathrm{d}a_1$	:	Infinitesimally small element of area at a point in the source
$\mathrm{d}a_2$	:	Infinitesimally small element of area at a point in the receiver
R	:	Distance between the points of definition in the source and receiver
θ_1	:	Angle between the line connecting the points in source and receiver and the normal to surface da_1, at the point of intersection
θ_2	:	Angle between the line connecting the points in source and receiver and the normal to surface da_2, at the point of intersection

B.2 Derivation of the view factor

The following definitions and formulas are obtained from [13]. The emittance ε of a graybody is independent of angle of incidence, however the radiant flux emitted by the graybody can vary with angle of incidence. To explain this, the term radiance is introduced. Radiance (L) is the area and solid angle density of radiant flux. It is the radiant flux per unit projected area and per unit solid angle incident on, passing through or emerging in a specified direction from a specified point in a specified surface. Its defining equation is:

$$L = \frac{\mathrm{d}^2\Phi}{\mathrm{d}\Omega \mathrm{d}s} = \frac{\mathrm{d}^2\Phi}{\mathrm{d}\Omega \mathrm{d}a_s \cos\theta} \tag{B.2}$$

where $\mathrm{d}s = \mathrm{d}a_s \cos\theta$ is a quantity called the projected area, the area of the projection of elemental area $\mathrm{d}a_s$ in the surface containing the point at which the radiance is being defined, projected in the direction of progation onto a plane perpendicular to this direction. $\mathrm{d}\Omega$ is an element of solid angle in the specified directoin and θ is the angle between this direction and the normal to the surface at the specified point. Radiance is a function of both position and direction, for many real sources it is a strongly varying function of direction.

There are however also surfaces whose radiance is independent of direction. These surfaces, real or imaginary, are called Lambertian radiators, mainly because they obey Lambert's cosine law. Lambert's cosine law states that the irradiance E (or exitance) from an element of area in a surface varies as the cosine of the angle θ between that direction and the perpendicular to that surface element, so: $E(\theta) = E(0)\cos\theta$. The radiance of a Lambertian radiator is independent of direction.

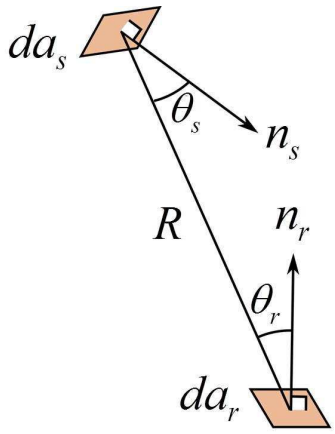

Figure B.1: The orientation of a source and a receiver area, involved in radiation

The radiation heat exchange between two blackbodies is dependent on their radiant fluxes, their geometry and their orientation. This can be shown with the following analysis. The radiance L of a point on a source surface A_s is defined by equation B.2. In that equation $\mathrm{d}a_s$ is an infinitesimally small element of area at the point of definition in the source, and $\mathrm{d}\Omega$ is an element of solid angle from the point of definition in the direction of interest. Besides the source also a receiver of area A_r is defined, containing infinitesimal area element $\mathrm{d}a_r$ at point P, at distance R from the point of definition in the source. The angles between R and the normals to surfaces $\mathrm{d}a_s$ and $\mathrm{d}a_r$ are angles θ_s and θ_r, respectively. All these angles and areas are shown in figure B.1. Now the element of solid angle $\mathrm{d}\Omega$ subtended by element of projected receiver area $\mathrm{d}a_r = \mathrm{d}a\cos\theta_r$ at distance R from the source is:

$$\mathrm{d}\Omega = \frac{\mathrm{d}a_r \cos\theta_r}{R^2} \tag{B.3}$$

so that, solving equation B.2 for $\mathrm{d}^2\Phi$ and using equation B.3, the element of flux received at point P from the element $\mathrm{d}a_s$ of area of the source is given by:

$$\mathrm{d}^2\Phi = L\frac{\mathrm{d}a_s \cos\theta_s \, \mathrm{d}a_r \cos\theta_r}{R^2} \tag{B.4}$$

The total flux Φ received by area A_r from source area A_s is being given by:

$$\Phi = \int_{A_s}\int_{A_r} L\frac{\mathrm{d}a_s \cos\theta_s \, \mathrm{d}a_r \cos\theta_r}{R^2} \tag{B.5}$$

This relation can be simplified when the source of radiance is Lambertian, and, in addition, has the same value for all points in the source surface. In this case, the radiance can be removed from any integrals over these variables and the remaining integrals are geometric in character. This simplification results in the following equation:

$$\Phi = L\int_{A_s}\int_{A_r} \frac{\mathrm{d}a_s \cos\theta_s \, \mathrm{d}a_r \cos\theta_r}{R^2} \tag{B.6}$$

The fundamental relationship between radiance L and irradiance E is given by:

$$E = \int_{\Omega} L\left(\theta, \phi\right) \cos\theta \, \mathrm{d}\omega \tag{B.7}$$

It is recalled that the radiance is assumed Lambertian and homogeneous, making it independent of angles θ and ϕ. Also, the solid angle Ω is taken to be 2π -the whole hemispherical solid angle- indicating that the relationship is to be integrated over $2\pi\, sr$. Taking a spherical coordinate system, the element of solid angle is given by $\mathrm{d}\omega = \sin\theta \, \mathrm{d}\theta \, \mathrm{d}\phi$, and the irradiance becomes:

$$\begin{aligned} E &= L \int_0^{2\pi} \int_0^{\pi/2} \cos\theta \, \sin\theta \, \mathrm{d}\theta \, \mathrm{d}\phi \\ &= \pi L \end{aligned}$$

So the flux from area A_s to area A_r can be written as:

$$\Phi = E \int_{A_s} \int_{A_r} \frac{\cos\theta_s \, \cos\theta_r}{\pi R^2} \, \mathrm{d}a_r \, \mathrm{d}a_s \tag{B.8}$$

In this expression for the radiant flux between two surfaces, the integral terms are purely geometrical. The radiant energy exchange can therefore be divided into a geometrical and a physical part, which can be convenient in complex radiation transfer problems. The geometrical part or factor in radiant energy exhange is called shape factor, view factor or configuration factor. This view factor is defined to be the fraction of total flux from the source surface that is received by the receiving surface. It is denoted by the symbol F_{s-r} or F_{1-2}. An expression for the view factor is obtained by dividing equation B.5 for the flux incident on the receiver Φ_{s-r} by the total flux emitted by the source Φ_s, as follows:

$$F_{s-r} = \frac{\Phi_{s-r}}{\Phi_s} = \frac{\displaystyle\int_{A_s}\int_{A_r} \frac{L \cos\theta_s \, \cos\theta_r \, \mathrm{d}a_s \mathrm{d}a_r}{R^2}}{\displaystyle\int_{A_s}\int_{2\pi} L \cos\theta \, \mathrm{d}\omega \, \mathrm{d}a_s}$$

$$= \frac{\displaystyle\int_{A_s}\int_{A_r} \frac{\cos\theta_s \, \cos\theta_r \, \mathrm{d}a_s \mathrm{d}a_r}{R^2}}{\pi A_s}$$

$$= \frac{1}{A_s} \int_{A_s}\int_{A_r} \frac{\cos\theta_s \, \cos\theta_r}{\pi R^2} \mathrm{d}a_s \mathrm{d}a_r \tag{B.9}$$

B.3 View factor model

Obtaining a thermal image of a surface with some defined image resolution works best when each pixel of the thermal imager or sensor only receives radiation from a point on the target directly opposite to the pixel. The measurement value of the pixel is then a direct measure for

Table B.1: The design parameters for the thermal imager of which the influence on view factors are evaluated. Also the expected effect of varying the parameter is given.

			Expected effect on F		
Design parameter		Change	F_{t1-s1}	F_{tj-s1}	F_{e-s1}
Distance target-sensor	d_{t-s}	Decrease	Increase	Decrease	Decrease
Area of sensor pixel	A_{si}	Decrease	Decrease	Decrease	Decrease
Guard height	h_g	Increase	Unchanged	Decrease	Decrease

one specific point and is not influenced by other points on the target. This would require that all radiation incident on sensor pixel 1 is coming from target point 1, i.e. $F_{s1-t1} = 1$. As stated before this is not entirely the case. The sensor pixel also receives radiation from other points on the target and from the environment. To be able to quantify and eliminate the influence of these unwanted radiation sources, the fraction of their emitted radiation incident on the sensor pixel must be determined, i.e. the view factors of these sources to the sensor pixel must be determined. Also the influence of some design parameters on the view factors are evaluated. The evaluated design paramters are listed in table B.1. The table also mentions the height of a guard. A guarding wall could be placed around each pixel, limiting the view of the pixel. This could decrease the influence of radiation sources other than the opposite point on the target. A schematic drawing of the target and sensor with and without guards around the pixels is shown in figure B.2.

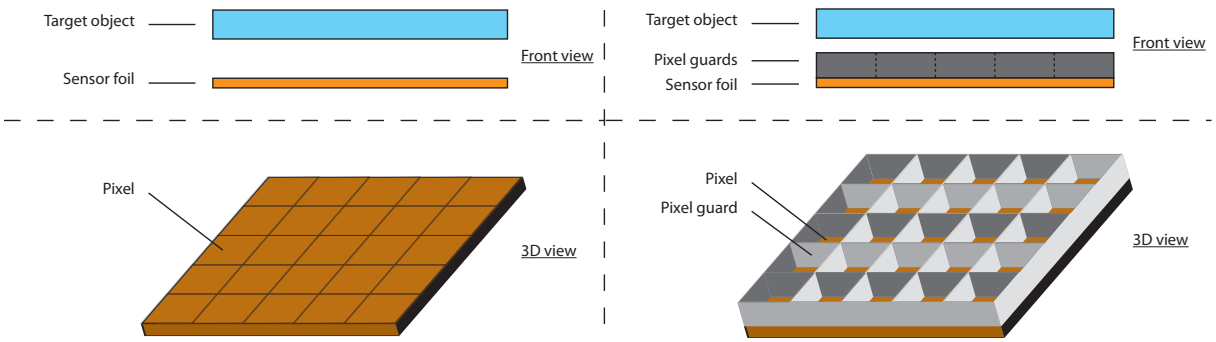

(a) Model 1 with a 5x5 pixel grid

(b) Model 2 with a 5x5 pixel grid and guarding walls bounding the pixels

Figure B.2: Schematic drawings of the sensor-target models with at the top a front view of target object and sensor foil, and at the bottom a 3D view of the sensor foil only.

Table B.2: Values used in the view factor model.

Target & sensor area (l x w)	A_t/A_s	50 x 50	[mm]
Number of pixels	n	25	[-]
Pixel area (l x w)	A_p	10 x 10	[mm]
Target-sensor distance	d_{t-s}	1	[mm]

B.4 Results

It is convenient to use a radiation conductance number (C) in stead of the view factor, because the area of the emitting surface also plays a role in the amount of radiation that is incident on a certain pixel. This radiation conductance is defined in equation B.10.

$$C_{1-2} = A_1 F_{1-2} \tag{B.10}$$

It should also be noted that the reciprocal rule is applicable to the conductance.

$$C_{1-2} = A_1 F_{1-2} = A_2 F_{2-1} = C_{2-1}$$

For the model shown in figure B.2a the conductances have been calculated with the values shown in table B.2.

The required radiation from target to pixel is the radiation from a target point (area on the target of the same size as a sensor pixel) to its opposite sensor pixel. The conductance of target point to opposite sensor pixel is shown in figure B.3. This conductance value is the same for each sensor pixel because the orientation of each sensor pixel to its opposite target point is the same and also their areas are equal.

Besides radiation from its opposite target point (the 'signal'), a sensor pixel also receives radiation from the other target points ('noise'). The conductance of the other (non-opposite) target points to the sensor pixel is dependent on their mutual orientation and therefore varies for different sensor pixels. The cumulative conductance of non-opposite target points to the sensor pixels are shown in figure B.4a. Also radiation from the space between target and sensor can be an unwanted source of radiation. The space between target and sensor is termed 'environment'. The conduction of the environment to all sensor pixels is shown in figure B.4b.

Figure B.4 shows that the conductance of non-opposite target points and of the environment is dependent on the location of the sensor pixel. The values mainly vary with distance to the corner of the sensor and distance to the middle of the sensor. Therefore four pixels are selected to compare based on their location on the sensor, namely, pixel 1 (outer ring, corner), pixel 3 (outer ring, middle), pixel 7 (middle ring, corner) and pixel 13 (middle of sensor area). The conductance of non-opposite target points (figure B.4a) is largest for pixels in the middle of the sensor, because these pixels are more centralized with respect to the target than the other

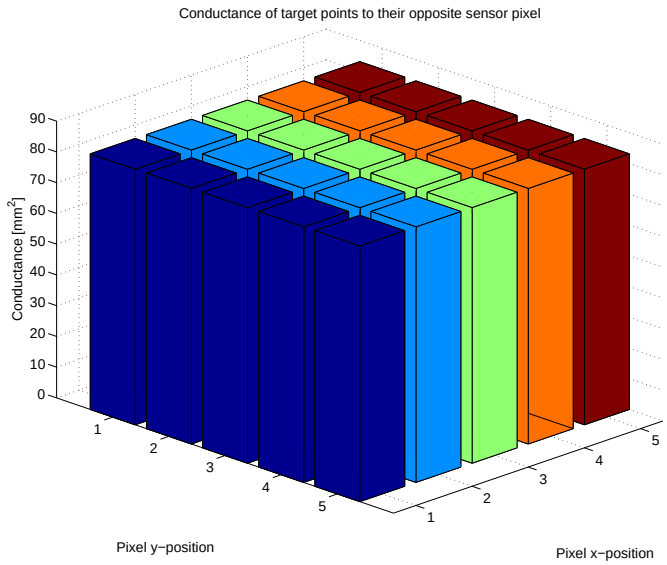

Figure B.3: For each sensor pixel the conductance of a target point to its opposite sensor pixel.

pixels. The conductance of the environment is larger for pixels at the side of the sensor because these pixels are closer to the environment than pixels which lie more towards the middle of the sensor. When all these unwanted conductances are summed it appears that the total unwanted conductance is appproximately the same for all pixels. This can be seen from the fact that in the left plot of figure B.5 the combined height of blue and green is the same for each pixel. Also the desired conductance of the opposite target point, the signal, is approximately 4 to 5 times larger than the sum of the unwanted conductances, the noise. To give a measure for the difference between wanted and unwanted conductance the conductance signal-to-noise ratio is defined as the ratio between the conductance of the signal divided by the conductance of the total noise for each sensor pixel. This signal-to-noise ratio is given by equation B.11.

$$S/N_{Csi} = \frac{C_{ti-si}}{\sum_{j \neq i} C_{tj-si} + C_{e-si}} \tag{B.11}$$

where S/N_{Csi} is the conductance signal-to-noise ratio of sensor pixel i, C_{ti-si} the conductance of target point i to sensor pixel i, $\sum_{j \neq i} C_{tj-si}$ the sum of all target points j to sensor pixel i where $j \neq i$, C_{e-si} the conductance of the environment to sensor pixel i. The signal-to-noise ratio for the selected pixels are shown in the right plot of figure B.5.

In the following subsections the influence of the design parameters listed in table B.2 on the conductance of the noise and signal sources and the signal-to-noise ratio will be shown.

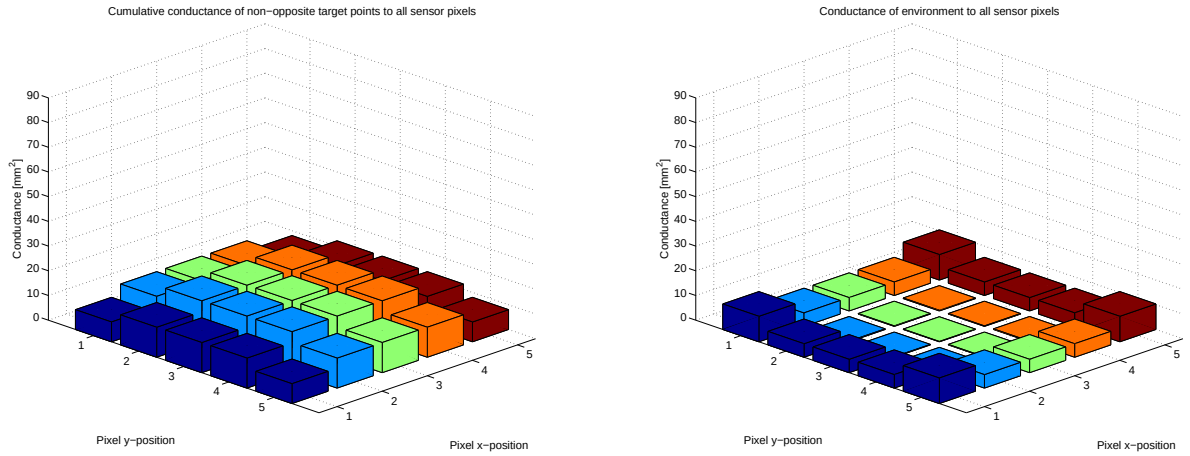

(a) Cumulative conductance of non-opposite target points tot all sensor pixels

(b) Conductance of the environment to all sensor pixels

Figure B.4: Conductance of all noise sources (non-opposite target points and environment) to all separate sensor pixels.

B.4.1 Influence of distance

This section shows the influence of the distance between the target and sensor surface on the conductances and signal-to-noise ratio. In the limit that the distance between the target and sensor surface is zero, the view factor of a target point to its opposite pixel (the signal) will be maximum, i.e. unity. Thereby the conductance of the signal will also be maximum. It is therefore expected that on decreasing the distance between target and sensor the conductance of the signal will increase. Due to the increasing conductance of the signal, the conductance of the target and environment noise will consequently decrease.

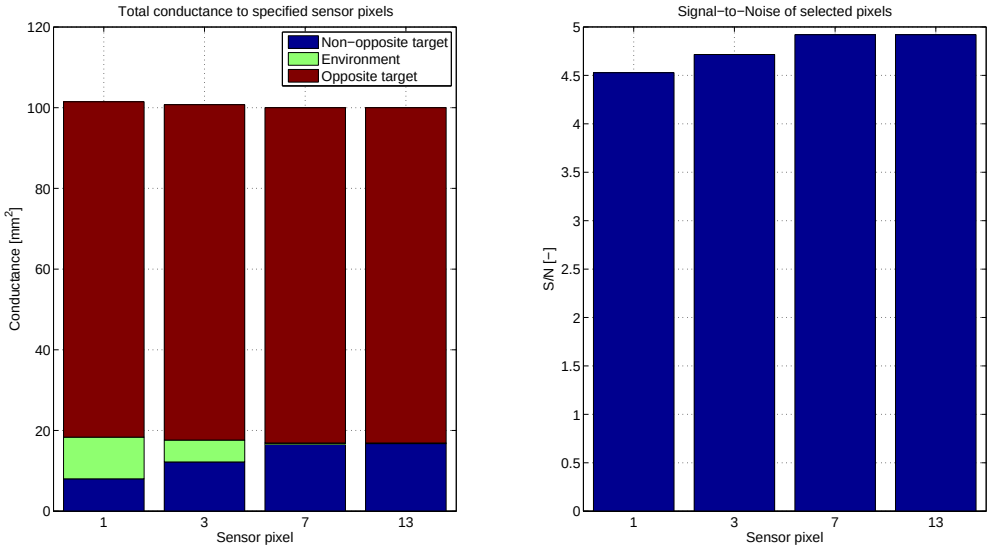

Figure B.5: Left: Conductance of opposite target point, cumulative of non-opposite target points and environment of sensor pixel 1,3,7 and 13. Right: Signal-to-Noise ratio of sensor pixel 1,3,7 and 13.

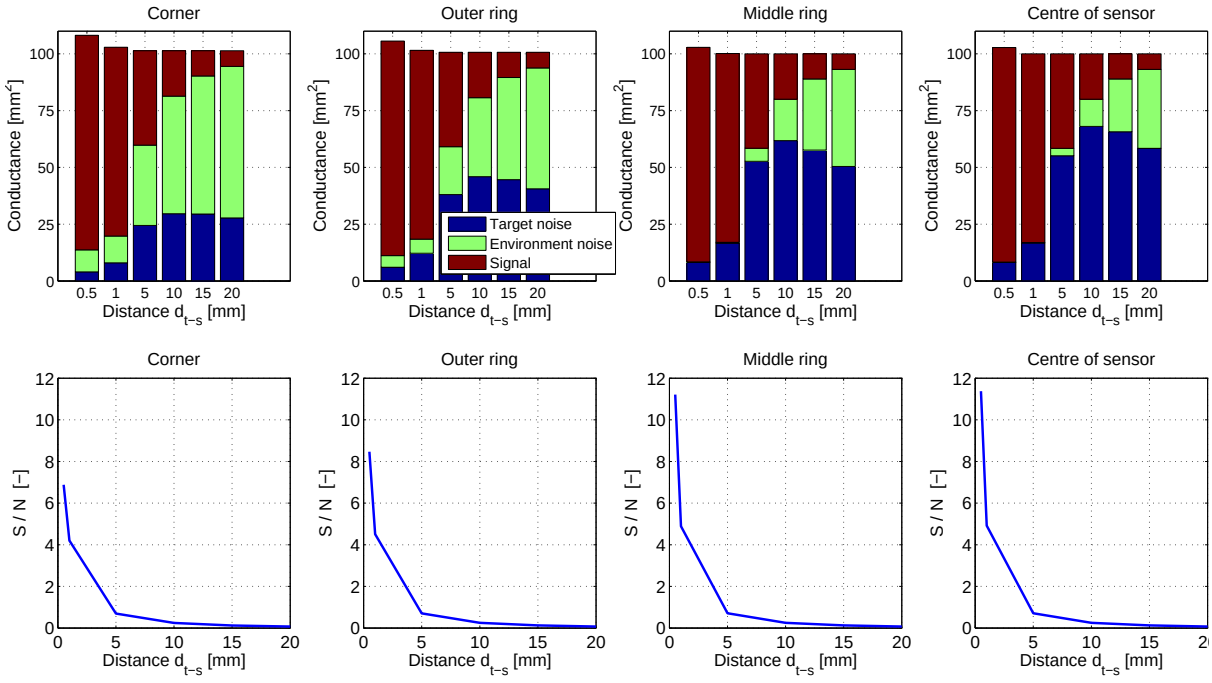

Figure B.6: Influence of target-sensor distance on conductances and signal-to-noise ratio. Top: Conductance of the signal, target noise and environment noise to pixels on the corner, outer ring, middle ring and centre of the sensor area. Bottom: Signal-to-noise ratio for a pixel on the corner, outer ring, middle ring and centre of the sensor area.

The top plots of figure B.6 show that with decreasing distance the conductance of the signal increases and the combined conductances of environment and target noise decrease. This causes an increase of the signal-to-noise ratio for decreasing distance, as expected. The conductance of the target noise increases up to a distance of 10 $[mm]$ after which the sum of noise conductances still increases, but the target noise conductance starts to decrease. This can be explained by the fact that the target area is constant but the environment area increases with increasing distance. For distances up to 10 $[mm]$ the area of the target is larger than the area of the environment, for distances larger than 10 $[mm]$ the environment area is larger, causing its view factor and conductance to increase at the expense of target noise.

B.4.2 Influence of guard height

The influence of guard height is calculated for a system with a target-sensor distance of 5 [mm], pixel width of 10 [mm] and guards around the pixels with a height varying between 0 and 5 [mm]. It is expected that the conductance of the signal is not influenced by the guards and that both the noise conductances decrease with increasing guard height. The guards will limit the view of a pixel to directions perpendicular to the pixel area and therefore guard the pixel from viewing surfaces which are not directly opposite to it.

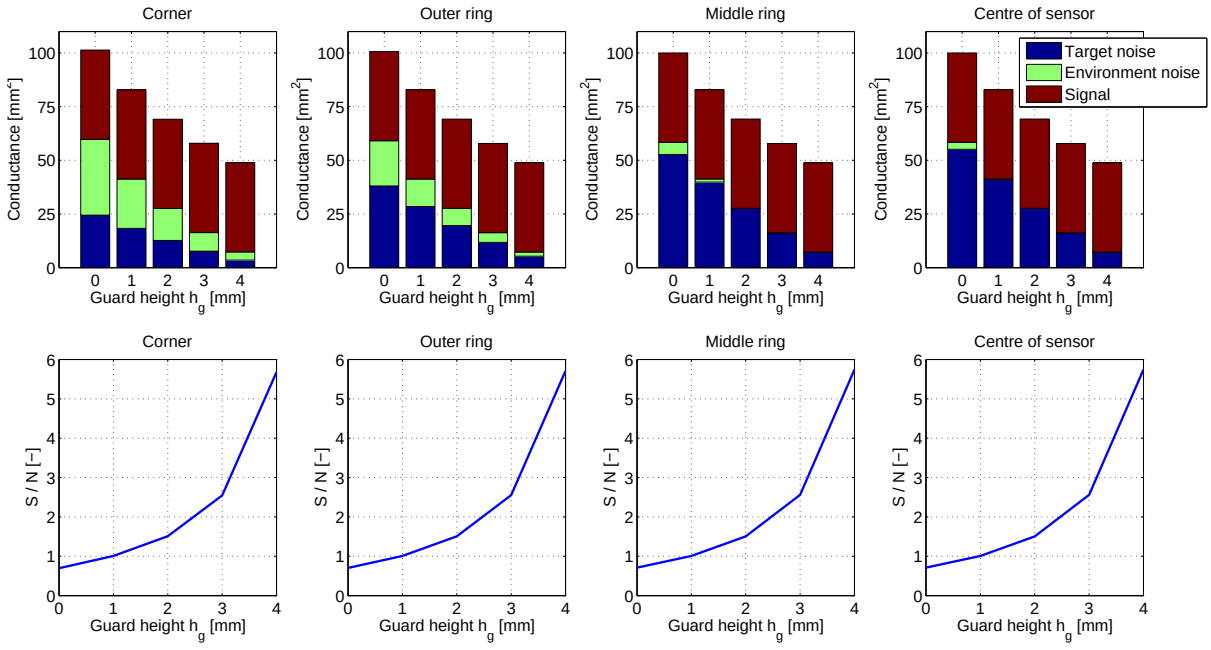

Figure B.7: Influence of guard height on conductances and signal-to-noise ratio. Top: Conductance of the signal, target noise and environment noise to pixels on the corner, outer ring, middle ring and centre of the sensor area. Bottom: Signal-to-noise ratio for a pixel on the corner, outer ring, middle ring and centre of the sensor area.

From the model it is verified that increasing guard height limits the view of a pixel to its opposite target point. In figure B.7 it is seen that the signal conductance remains unchanged but by the limiting effect of the guards, the noise conductances decrease. This causes the signal-to-noise ratio to increase when the guard height is increased. When comparing the signal-to-noise with guards to the situation of varying distance it is interesting to note that the signal-to-noise ratio with distance of 5 [mm] and guards of 4 [mm] (leaving 1 [mm] free space between target and sensor) is higher than with a distance of 1 [mm] and no guard.

B.4.3 Influence of pixel width

The width and thereby the area of the pixels is varied while keeping the total area of the sensor constant. A smaller pixel therefore leads to more pixels in total. The target-sensor distance is 1 [mm], the sensor area 50 x 50 [mm] and there are no guards surrounding the pixels. Increasing the pixel width is expected to increase the signal conductance because the target area which is defined as being the opposite target point increases according to the increase of the pixel area. Therefore the target signal area increases with respect to the noise areas, causing its conductance to increase, with increasing pixel width.

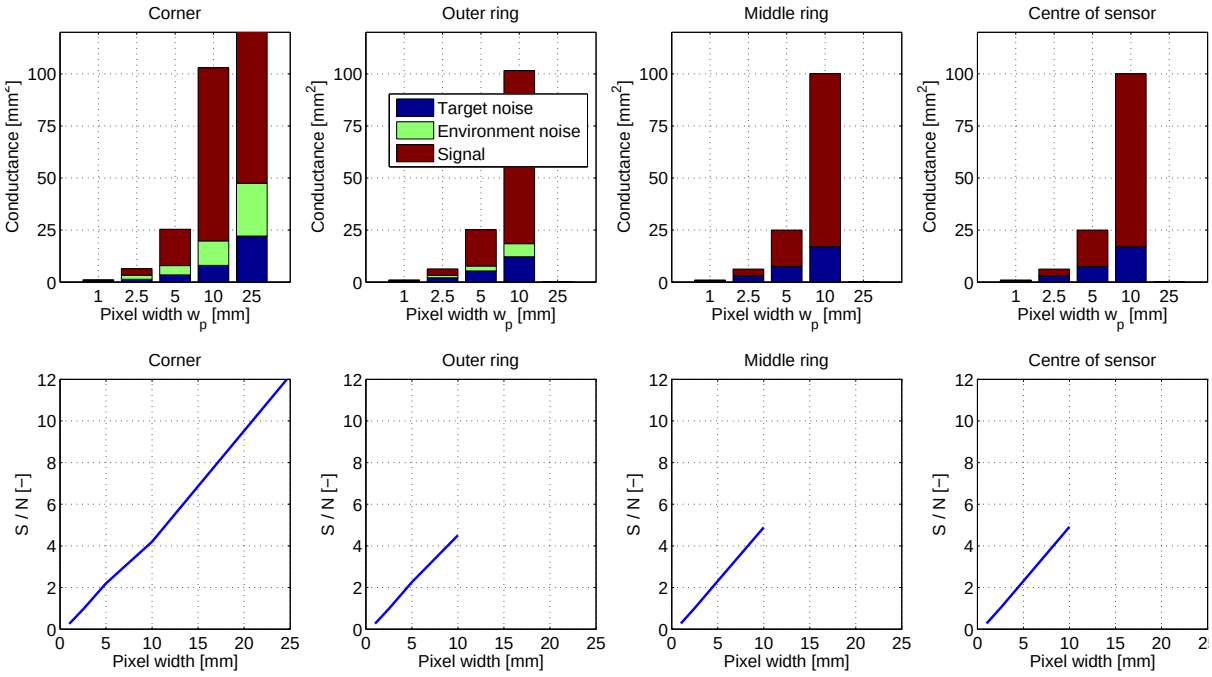

Figure B.8: Influence of pixel width on conductances and signal-to-noise ratio. Top: Conductance of the signal, target noise and environment noise to pixels on the corner, outer ring, middle ring and centre of the sensor area. Bottom: Signal-to-noise ratio for a pixel on the corner, outer ring, middle ring and centre of the sensor area.

Figure B.8 shows the conductances and signal-to-noise ratio for different pixel widths. The total sensor area is 50 x 50 [mm] so at a pixel width of 10 [mm] the sensor contains 5x5 = 25 pixels and a corner, outer ring, middle ring and centre pixel can be defined. At pixel width 25 [mm] however the sensor contains only 2x2 = 4 pixels and all pixels are corner pixels. Therefore only the plot of the corner pixel is defined up to a pixel width of 25 [mm]. For increasing pixel width the conductance of the signal as well as the conductance of noise increases, but as can be seen in figure B.8 the signal-to-noise ratio increases with increasing pixel width. It must however be noted that the image resolution also decreases when the pixel width increases.

B.5 Discussion

The goal of looking at the influence of sensor design parameters is to maximize the radiation received by a sensor pixel from its opposite target point and thereby maximizing the attainable temperature resolution of the sensor. This is realized by maximizing the signal-to-noise ratio (S/N ratio) as defined in section B.4. Increasing the width and thereby the area of the sensor pixels increases the S/N ratio, but also decreases the attainable image resolution. Since the required image resolution is fixed, the pixel width cannot be larger than the width dictated by the required image resolution.

Using guards around the pixels to limit the conductance of the noise sources yields good signal-to-noise ratios. At a target-sensor distance of 5 [mm] and a guard height of 4 [mm] the S/N ratio is about 5.7 for all pixels, for a target-sensor distance of 1 [mm] and no guards the S/N ratio is about 4.5. In both these cases the sensor object is 1 [mm] apart from the target, and the case with guards yields a better S/N ratio. In this analysis however the secondary effect of heat transported from the target to the guards and then from the guards to the pixel is not taken into account. This effect will lower the obtained S/N ratio. Moreover a sensor object with guards will introduce more complex manufacturability.

Decreasing the distance between target-sensor distance increases the conductance of the signal and reduces the conductance of the noise sources. Decreasing the target-sensor distance is therefore an effective and simple way to improve the S/N ratio. From this analysis it is concluded that the pixel width should be as large as the required image resolution allows. Then the distance between target and sensor should be made as small as possible. The use of guards does not seem feasible because it introduces complexity to the manufacturability and improves the S/N ratio only slightly.

APPENDIX C

Experimental validation

C.1 Setup properties

This section shows the properties and dimensions of the components used in the setups for the experimental validation. These are listed in table C.1

C.2 Calibration

In this appendix the most important results of the calibration are given. Section C.2.1 shows the absolute temperatures and temperature differences of the first series of thermistors (thermistors 2 to 10) during calibration at the maximum, middle and minimum calibration point. In order to check the temperature uniformity of the calibration block containing the thermistors, the calibration procedure was repeated with a shuffled configuration of the thermistors. The resulting measured temperature difference for the initial and shuffled configuration are shown in section C.2.2. For additional series of thermistors, calibrated after the first series, a thermistor of the first series was used as reference. For completeness the absolute temperatures and temperature differences of the thermistors during calibration of thermistors 19 to 26 are shown in section C.2.3.

Table C.1: Dimensions and properties of the components used for the experimental validation

Component	Property	Units		Remarks
Thermistor (EPCOS B57540)	Bead length	[mm]	1.4	
	Bead diameter	[mm]	0.8	
	Nominal resistance	[kΩ]	10	At T = 298 [K]
	Dissipation factor	[mW/K]	0.4	
	Heat capacity	[mJ/K]	1.3	
	Time constant	[s]	3.0	
	B-value	[K]	3480	
Peltier (TEC1 12705HTS)	Cooling power	[W]	56	Maximum
	Dimensions	[mm]	40x40x4.2	
Aluminium block	Dimensions	[mm]	90x90x60	
	Holes	[mm]	30x2	Depth x diameter
	Hole spacing	[mm]	2	
Mercury thermometer	Absolute error	[K]	±0.1	
Reference object	Dimensions	[mm]	70x70x6	
	Holes	[mm]	5	For thermistors
Target object	Dimensions	[mm]	70x70x6	
	Holes	[mm]	5	For thermistors
Pixel frame	Outer dimensions	[mm]	70x70x1	
	Container leg length	[mm]	21	
Beamer (BENQ SP870)	Intensity	[ANSI lumen]	5000	

C.2.1 First thermistor series

The aluminium block used for calibration contains 9 holes to insert thermistors. Since thermistor 1 was broken, thermistors 2 to 10 were inserted into the block. The first series of calibrated thermistors is therefore made up of thermistors 2 to 10. In the measurement results of the middle calibration point, shown in figure C.2, one of the thermistors appears to have a significant temperature difference with respect to the others. The results of thermistor 2 differed from the other thermistors in multiple measurements. It is assumed that the electrical contact of this thermistor is not good and therefore thermistor 2 is omitted from further results.

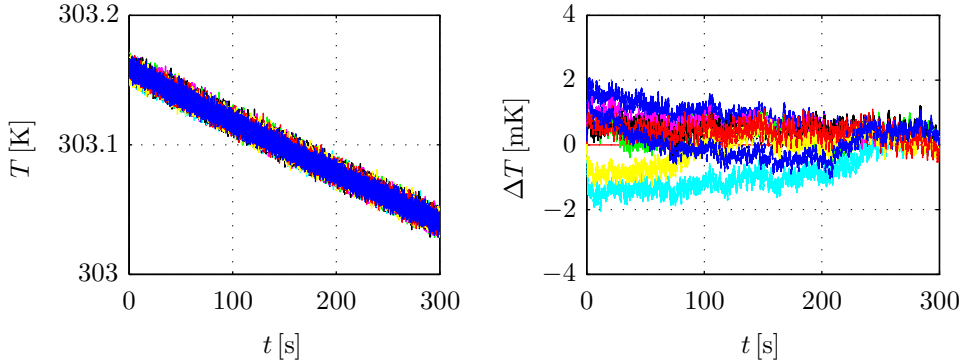

(a) Temperature (b) Temperature difference (averaged 150x)

Figure C.1: Absolute temperature and temperature difference with respect to thermistor 3 of thermistors 2 to 10 at the maximum calibration point (∼303 [K]).

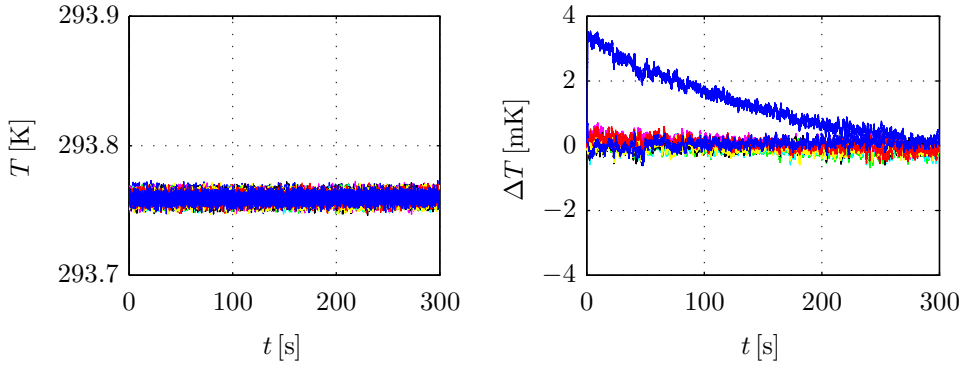

(a) Temperature (b) Temperature difference (averaged 150x)

Figure C.2: Absolute temperature and temperature difference with respect to thermistor 3 of thermistors 2 to 10 at the middle calibration point (∼293 [K]).

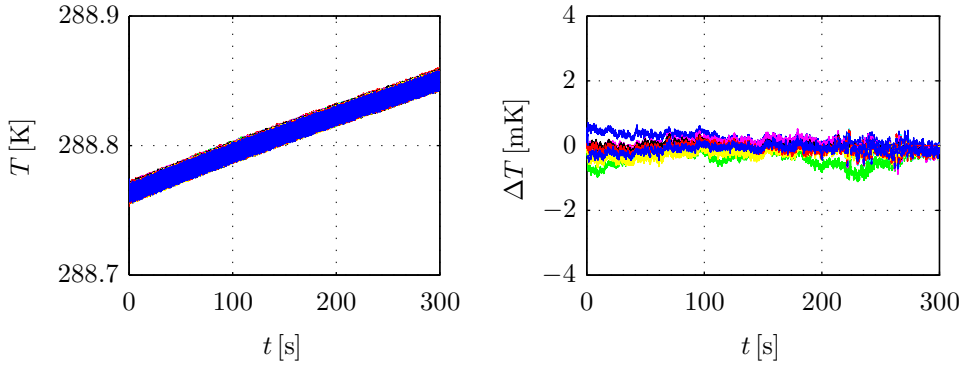

(a) Temperature (b) Temperature difference (averaged 150x)

Figure C.3: Absolute temperature and temperature difference with respect to thermistor 3 of thermistors 2 to 10 at the minimum calibration point (∼289 [K]).

C.2.2 Temperature uniformity

To check the temperature uniformity of the the thermistors during calibration, the calibration procedure has been performed in two different configurations. The actual calibration yielding the calibration values has been performed with thermistors 2 to 10 inserted into the holes of the calibration block as shown in figure C.4a. Subsequently the thermistors were shuffled into the configuration shown in figure C.4b and the calibration procedure was repeated. For both configurations the measured temperature differences were calculated with the calibration values obtained from calibration in the initial configuration. The results of the three calibration points measured in each configuration, show that the tempeature differences between the thermistors is largest at the maximum calibration point. The maximum temperature difference is about 4 [mK], as can be seen in figure C.5b. The fact that the largest temperature differences appear at the maximum calibration point can be explained by the fact that in that case the temperature difference of the calibration block with the ambient temperature is largest. Therefore the calibration block exchanges more heat with the environment and larger temperature differences can occur.

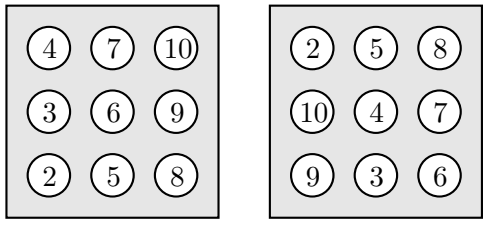

(a) Initial (b) Shuffled

Figure C.4: Placement of the thermistors in the calibration block for the initial and shuffled conifguration.

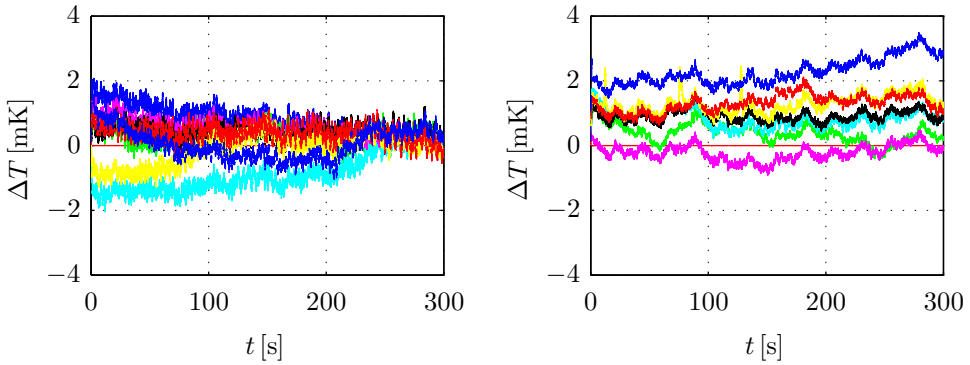

(a) Initial configuration (averaged 150x) (b) Shuffled configuration (averaged 150x)

Figure C.5: Temperature differences with respect to thermistor 3 at the maximum calibration point (∼303 [K]), in the initial and shuffled configuration.

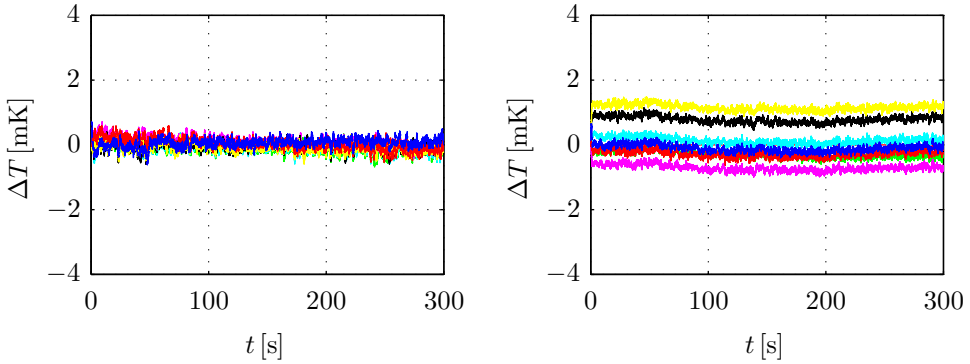

(a) Initial configuration (averaged 150x) (b) Shuffled configuration (averaged 150x)

Figure C.6: Temperature differences with respect to thermistor 3 at the middle calibration point (∼295 [K]), in the initial and shuffled configuration.

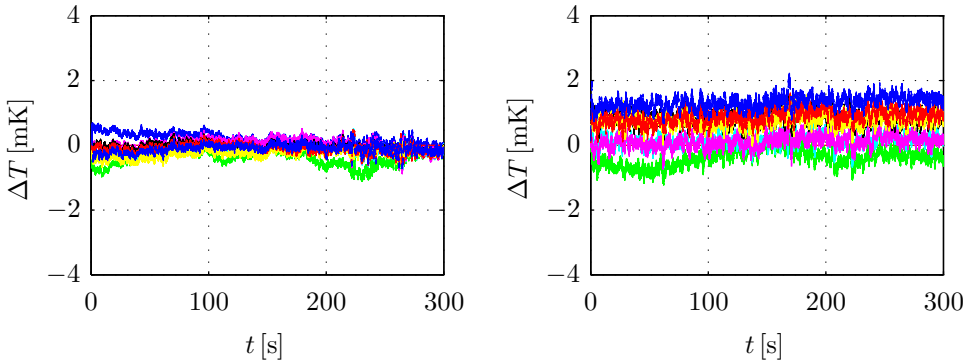

(a) Initial configuration (averaged 150x) (b) Shuffled configuration (averaged 150x)

Figure C.7: Temperature differences with respect to thermistor 3 at the minimum calibration point (∼289 [K]), in the initial and shuffled configuration.

C.2.3 Additional thermistor series

The remainder of the thermistors have been calibrated against a thermistor of the first calibration series. In this section the results of calibrating thermistors 19 to 26 against thermistor 7 are shown. The configuration of the thermistors in the calibration block is depicted in figure C.8. Figures C.9, C.10, C.11 show the absolute temperatures and temperature difference of the thermistors during calibration. The temperature differences are calculated with respect to thermistor 7. The temperature of thermistor 7 was calculated using the calibration values obtained from the calibration of the first thermistor series (thermistor 2 to 10).

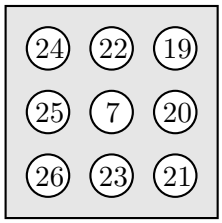

Figure C.8: Placement of the thermistor in the calibration block for thermistor series 19 to 26, using thermistor 7 as reference.

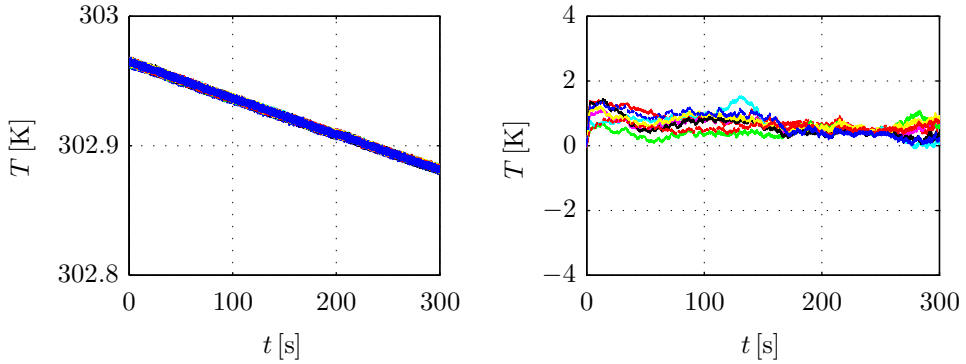

(a) Temperature (b) Temperature difference (averaged 150x)

Figure C.9: Absolute temperature and temperature difference with respect to thermistor 7 of an additional series of thermistors at the maximum calibration point (∼303 [K]).

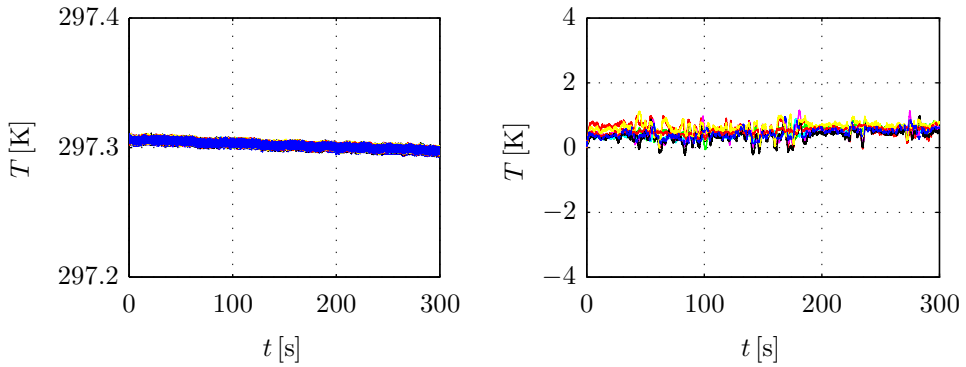

(a) Temperature (b) Temperature difference (averaged 150x)

Figure C.10: Absolute temperature and temperature difference with respect to thermistor 7 of an additional series of thermistors at the middle calibration point (∼295 [K]).

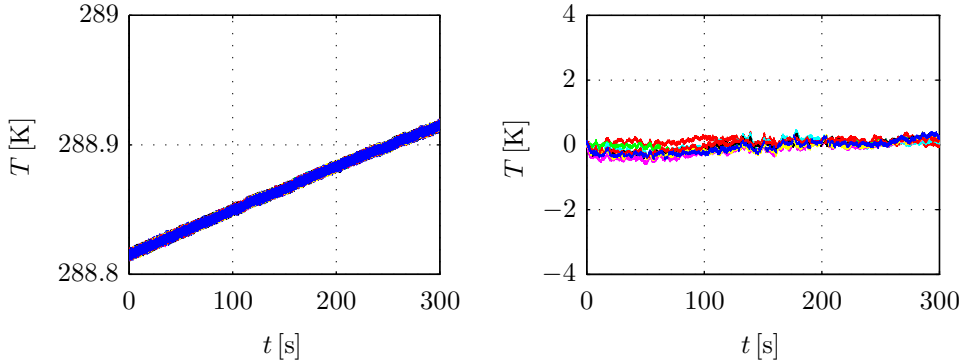

(a) Temperature (b) Temperature difference (averaged 150x)

Figure C.11: Absolute temperature and temperature difference w.r.t.thermistor 7 of an additional series of thermistors at the minimum calibration point (∼289 [K]).

C.2.4 Resolution additional results

This appendix shows the fluctuations in the measured temperature differences during the resolution experiment. Figure C.12 shows the measured temperature difference between the outer thermistors, ΔT_L. Figure C.13 shows the measured temperature difference between the inner thermistors, ΔT_l. Both temperature differences show large fluctuation in the first part of the measurement were the outer temperatures are controlled to their setpoints. After 400 [s] the outer temperatures have reached their setpoint and relatively high frequent fluctuations remain. It is assumed that these fluctuations are due to electrical noise in the measurement signals.

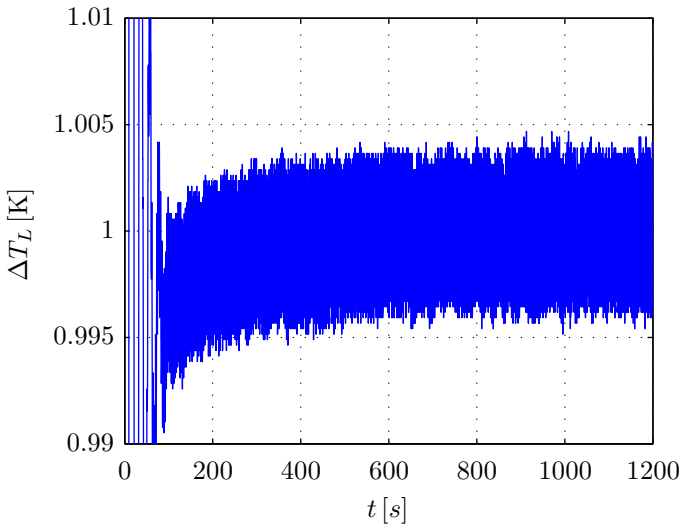

Figure C.12: Measurement of the temperature difference between the thermistors at the outside of the resolution block. After 400 [s] the setpoint is reached and the remaining measured temperature fluctuations are relatively high frequent and about 8 [mK] peak-to-peak.

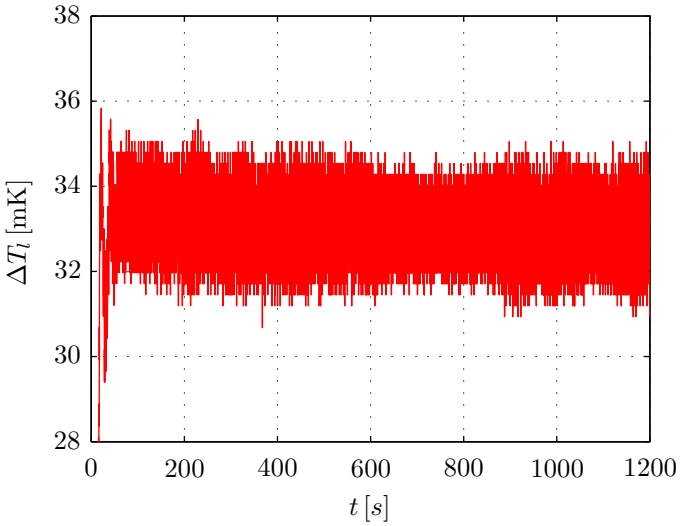

Figure C.13: Measurement of the temperature difference between the thermistors at the outside of the resolution block. After 400 [s] the setpoint is reached and the remaining measured temperature fluctuations are relatively high frequent and about 4 [mK] peak-to-peak.

C.3 Pixel experiment results

C.3.1 Setup thermal properties

Overview of thermal properties

In table C.2 an overview of the calculated heat capacities and heat transfer coefficient is given. The calculation of these properties are given in the rest of this section.

Table C.2: Overview of the thermal properties of the pixels. Showing their heat capacity C, conduction heat transfer coefficient g_{cond}, radiation heat transfer coefficient g_{rad} and convection heat transfer coefficient g_{conv}.

Pixel size [mm]	C [mJ/K]	g_{cond} [mW/K]	g_{rad} [mW/K]	g_{conv} [mW/K]
3x3	0.7	0.4	0.1	0.02
10x10	7.3	0.4	1.1	0.26
30x30	65.6	0.4	9.5	2.3

Heat capacity

The heat capacity of the pixel is determined by the heat capacities of its components. The pixel consists of a foil, a thermistor, a container and some thermal paste. The calculation of their

heat capacities and the heat capacity of the total pixel is shown here. The material properties that have been used are shown in table C.3.

Table C.3: Material properties used in the calculation of the heat capacity.

Material	Property	Symbol	Value	Units
Aluminium	Density	ρ	2700	[kg/m^3]
	Specific heat capacity	c_p	900	[J/kgK]
PVC	Density	ρ	1000	[kg/m^3]
	Specific heat capacity	c_p	1000	[J/kgK]
	Thermal conductivity	k	0.2	[W/mK]
Thermal paste	Density	ρ	2000	[kg/m^3]
	Specific heat capacity	c_p	1000	[J/kgK]

Foil The foil is made of aluminium which is sprayed black on both sides to improve absorption of radiation. The heat capacity of the foil including the paint is approximated by assuming a total thickness of the foil, including the paint, and using the material properties of aluminium. The heat capacity for the different pixel size is calculated as,

$$C_{\text{foil}} = \rho c_p V = \rho c_p t A_{\text{p}}$$

where t is the thickness of the foil and A_{p} is the area of the pixel. A thickness of 30 [μm] and the material properties of aluminium, given in table C.3, are used in the calculation. The calculated heat capacities are given in table C.4.

Table C.4: Heat capacity of the three different foil sizes.

Foil dimension [mm]	Area [cm^2]	Heat capacity [mJ/kgK]
3x3	0.09	0.7
10x10	1	7.3
30x30	9	65.6

Thermistor The thermistors are NTC thermistors, EPCOS B57540. On the datasheet of these thermistors the heat capacity is listed as approximately 1.3 [mJ/K].

Container The dimennsions of the container are shown in appendix [**ref!**]. From this dimensions the volume of the container is calculated to be 3 [mm^3]. The container is made of PVC, of which the material properties are given in table C.3. The heat capacity is then calculated to be,

$$C_{\text{cont}} = \rho c_p V = 3[\text{ mJ/K}]$$

Thermal paste Thermal paste is put in, and on the top edge of the container to ensure temperature uniformity of thermistor and foil. The volume of thermal paste is approximated to be equal to the open volume of the container, which is 1 [mm^3]. Together with the material properties of the thermal pasted listed in table C.3, this leads to a heat capacity of,

$$C_{\text{tp}} = \rho c_p V = 2[\text{ mJ/K}]$$

Heat transfer coefficient

The total heat transfer coefficient of the pixel consists of a heat transfer coefficient for conduction, convection and radiation. In this appendix the calculation of these coefficient is shown.

Conduction Heat transfer by conduction from and to the pixel takes place through the wires of the thermistors and through the legs of the pixel frame. The heat transfer coefficient caused by the wires is listed in the thermistor's datasheet to be approximately 0.4 [mW/K]. There are 4 legs attaching the container to the pixel frame. These legs have a cross sectional area A_{cond} of 0.3 x 0.5 [mm] and lenght L of 20 [mm]. With the thermal conductivity k of PVC given in table C.3, the heat transfer coefficient of the legs g_{legs} is calculated to be,

$$g_{\text{legs}} = \frac{nkA_{\text{cond}}}{L} = 0.006 \text{ [mW/K]}$$

where n is the number of legs. It is clear that the heat transfer coefficient of the wires is significantly larger than that of the legs. The conductive heat transfer coefficient g_{cond} therefore reduces to the coefficient of the wires.

Convection The convective heat transfer coefficient is calculated as an average heat transfer coefficient per unit area $\overline{h}$ [1]. This average coefficient is given by,

$$\overline{h} = \frac{Nu\, k}{L} \tag{C.1}$$

where Nu is the Nusselt number, k the thermal conductivity of the fluid involved in convection (air in this case) and L a characterstic of the solid object involved in convection. For natural convection along a vertical plate the Nusselt number is given by,

$$Nu = 0.68 + 0.670(Ra_L \Psi) \tag{C.2}$$

The Rayleigh number Ra_L and Ψ are given by the following relationships,

$$Ra_L = \frac{\beta \Delta T g L^3}{\nu \alpha}$$

$$\Psi = \left[1 + \left(\frac{0.492}{Pr}\right)^{9/16}\right]^{16/9}$$

In these equations β is the volumetric expansion coefficient of air, ΔT the temperature difference between the solid object and the bulk of the fluid, g the gravition constant, L a characteristic length of the solid object, ν the kinematic viscosity of air, α the thermal diffusivity of air and Pr the Prandtl number of air. The properties of air are evaluated at a temperature of 296 [K]. The temperature ΔT is estimated to be 0.1 [K], this is approximately the temperature increase of the pixel when it is exposed to a light dot from the beamer. The characteristic length L is half of the height of the largest pixel; 15 [mm]. This leads to an average heat transfer coefficient $\overline{h}$ of 1.3 [W/m^{2}K]. The convective heat transfer then depends on the area of the pixel as,

$$g_{\text{conv}} = \overline{h} 2 A_p = 2.6 A_p \tag{C.3}$$

where A_p is the area of the pixel. The factor 2 comes from the fact that convection takes place at the front and back surface of the pixel.

Table C.5: Convective heat transfer coefficient for different pixel sizes.

Foil dimension [mm]	Area [cm^2]	g_{conv} [mW/K]
3x3	0.09	0.02
10x10	1	0.26
30x30	9	2.3

Radiation As stated in section 2.2.4 the radiation heat transfer coefficient of the pixel can be determined by the following relationship,

$$g_{\text{rad}} = 4 \sigma \varepsilon T_{\text{lin}}^3 (2 A_p) \tag{C.4}$$

where σ is the Stefan-Boltzmann constant, ε the emissivity of the pixel, T_{lin} the temperature around which radiation heat transfer is linearized and $2A_p$ the area of the front and back of the pixel. For a linearization temperature of 296 [K] and a pixel emmissitivy of 0.9, this leads to the following equation for the coefficient,

$$g_{\text{rad}} = 10.6 A_p$$

The radiation heat transfer coefficient for the different pixel sizes is given in table C.6.

Table C.6: Radiation heat transfer coefficient for different pixel sizes.

Foil dimension [mm]	Area [cm^2]	g_{rad} [mW/K]
3x3	0.09	0.1
10x10	1	1.1
30x30	9	9.5

C.3.2 Thermal resolution measurement results

Results of the smallest pixel

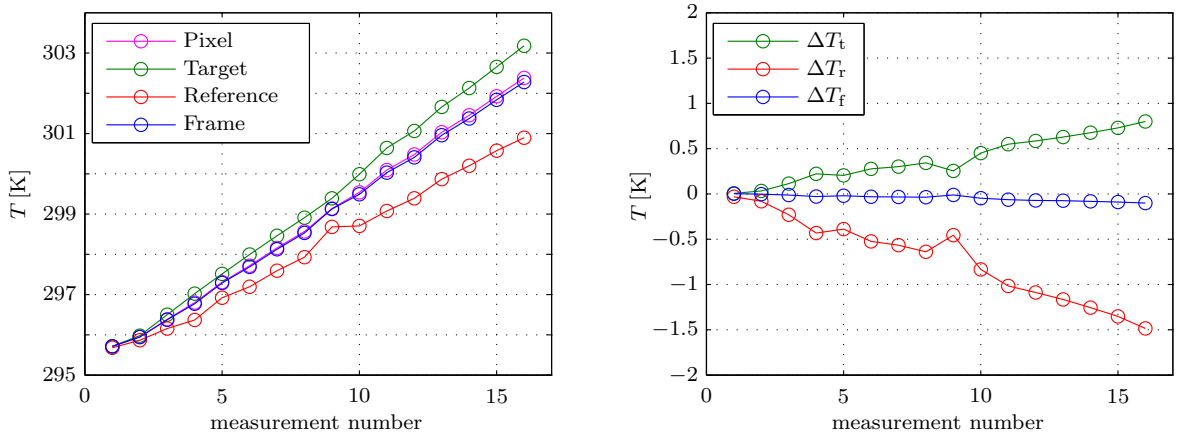

(a) Temperatures (b) Temperature differences

Figure C.14: Temperatures and temperature differences during measurements at different target temperatures with the smallest pixel.

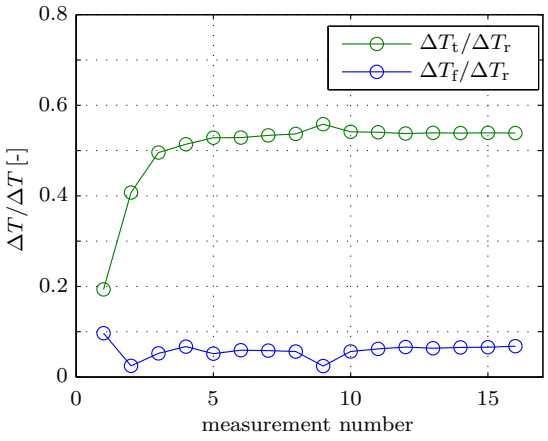

Figure C.15: Ratio of temperatures differences during measurements at different target temperatures with the smallest pixel.

Results of the middle pixel

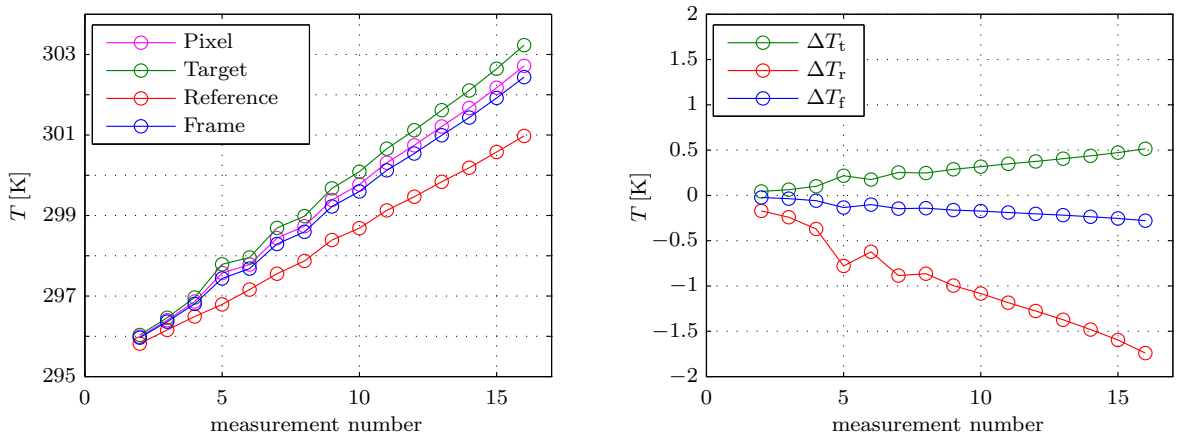

(a) Temperatures (b) Temperature differences

Figure C.16: Temperatures and temperature differences during measurements at different target temperatures with the middle pixel.

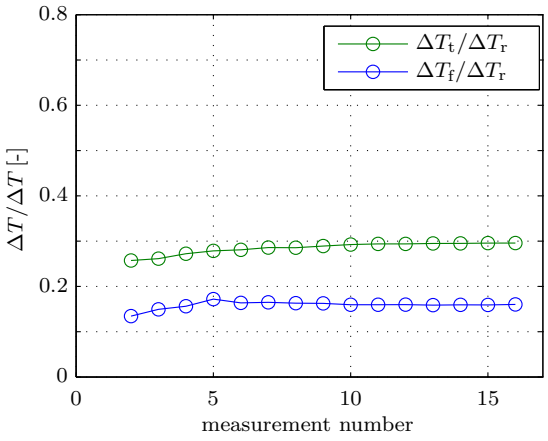

Figure C.17: Ratio of temperatures differences during measurements at different target temperatures with the middle pixel.

Results of the largest pixel

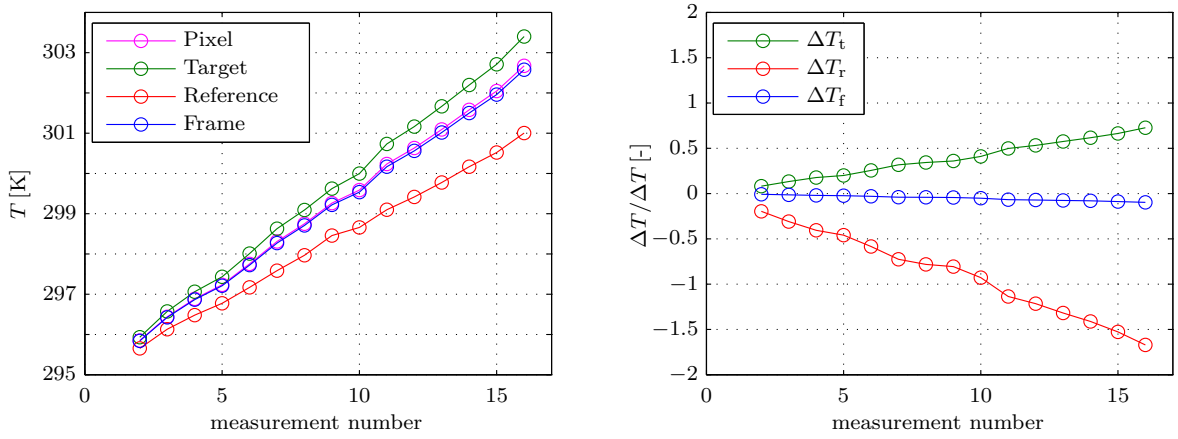

(a) Temperatures (b) Temperature differences

Figure C.18: Temperatures and temperature differences during measurements at different target temperatures with the largest pixel.

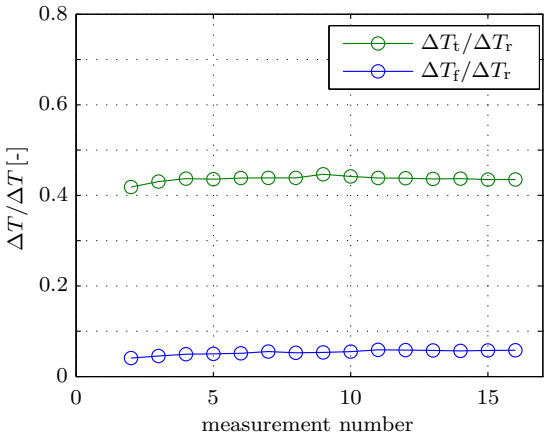

Figure C.19: Ratio of temperatures differences during measurements at different target temperatures with the largest pixel.